

SELECTIVE ELECTROCHEMICAL DETECTION OF MOLECULAR
BIOMARKERS AT CARBON ELECTRODES



A Thesis Submitted in Partial Fulfillment of the Requirements for the
Degree of Doctor of Philosophy in Chemistry
Suranaree University of Technology
Academic Year 2023

การตรวจวัดทางเคมีไฟฟ้าแบบจำเพาะของสารบ่งชี้ทางชีวภาพ
โดยใช้ชีวไฟฟ้าคาร์บอน



นางสาวธิดาภา รัตนอัมพา

วิทยานิพนธ์นี้เป็นส่วนหนึ่งของการศึกษาตามหลักสูตรปริญญาวิทยาศาสตรดุษฎีบัณฑิต
สาขาวิชาเคมี
มหาวิทยาลัยเทคโนโลยีสุรนารี
ปีการศึกษา 2566

SELECTIVE ELECTROCHEMICAL DETECTION OF MOLECULAR BIOMARKERS
AT CARBON ELECTRODES

Suranaree University of Technology has approved this thesis submitted in
partial fulfillment of the requirements for the Degree of Doctor of Philosophy.

Thesis Examining Committee



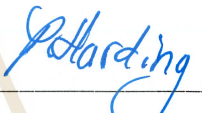
(Asst. Prof. Dr. Sireerat Lisnund)

Chairperson



(Assoc. Prof. Dr. Sanchai Prayoonpokarach)

Member



(Assoc. Prof. Dr. Phimpaka Harding)

Member



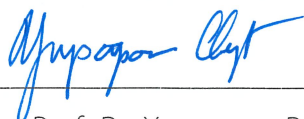
(Assoc. Prof. Dr. Kamonwad Ngamchuea)

Member (Thesis Advisor)



(Asst. Prof. Dr. Patcharin Chaisuwan)

Member



(Assoc. Prof. Dr. Yupaporn Ruksakulpiwat)

Vice Rector for Academic Affairs
and Quality Assurance



(Prof. Dr. Santi Maensiri)

Dean of Institute of Science

ธิดาภา รัตนอัมพา : การตรวจวัดทางเคมีไฟฟ้าแบบจำเพาะของสารบ่งชี้ทางชีวภาพโดยใช้
ขั้วไฟฟ้าคาร์บอน (SELECTIVE ELECTROCHEMICAL DETECTION OF MOLECULAR
BIOMARKERS AT CARBON ELECTRODES) อาจารย์ที่ปรึกษา : รองศาสตราจารย์ ดร.
กมลวิช งามเชื้อ. 147 หน้า

คำสำคัญ : คาร์บอนที่มีรูพรุนในระดับไมโคร/กรดยูริก/กรดแอสคอร์บิก/โดพามีน/เซ็นเซอร์วัดแก๊ส
ออกซิเจน/ฮีมีน

วิทยานิพนธ์เล่มนี้มุ่งศึกษาวิธีการตรวจวัดสารในร่างกายมนุษย์ (bodily fluids) เช่น กรด
ยูริก (Uric acid, UA) กรดแอสคอร์บิก (Ascorbic acid, AA) และโดพามีน (Dopamine, DA) ใน
สภาวะที่ร่างกายมีระดับของกรดยูริก กรดแอสคอร์บิก และโดพามีนสูง จะทำให้เสี่ยงต่อการเกิดโรค
ต่าง ๆ ได้ ซึ่งตรวจวัดปริมาณของสารเหล่านี้ทำได้โดยใช้วิธีเซนเซอร์ทางเคมีไฟฟ้าโดยการใช้การ
ดัดแปลงขั้วไฟฟ้าด้วยนาโนคอมโพสิตชนิดต่าง ๆ นอกจากนี้ยังได้ศึกษาสารฮีมีน (Hemin) เป็นสารที่
พบในร่างกาย มีโครงสร้างคล้ายฮีโมโกลบิน เป็นผลิตภัณฑ์ที่เกิดจากการเกิดปฏิกิริยาออกซิเดชันของ
ฮีโมโกลบิน ซึ่งการรวมตัวกันของสารฮีมีนเป็นสาเหตุที่ทำให้เกิดความผิดปกติในร่างกายได้ สารฮีมีนมี
คุณสมบัติเด่นคือสามารถใช้เป็นตัวจับออกซิเจนได้ โดยในงานวิจัยนี้ได้ศึกษาปฏิกิริยารีดักชันของ
ออกซิเจนโดยใช้ฮีมีนเป็นตัวเร่งในการจับออกซิเจนในสภาวะที่มีความเข้มข้นของเกลือสูง

วัสดุอิเล็กโทรดคอปเปอร์ออกไซด์ (Copper oxide: Cu_2O และ CuO) คาร์บอนนาโนทิวป์
(Carbon nanotube, CNT) และคาร์บอนที่มีรูพรุนในระดับไมโคร (Microporous carbon, MC)
นิยมนำมาใช้ศึกษาปฏิกิริยาออกซิเดชันของกรดยูริก กรดแอสคอร์บิก และโดพามีน ในตัวอย่างเลือด
และปัสสาวะ จากผลการทดลองพบว่า MC มีประสิทธิภาพในการวัดสารทั้ง 3 ชนิด ได้ดีกว่า Cu_2O ,
 CuO และ CNT และเมื่อทดสอบโดยใช้เทคนิคไซคลิกโวลแทมเมตรีและเทคนิคดิฟเฟอเรนเชียลพัลส์โวล
แทมเมตรีและขั้ว MC พบว่าสามารถแยกสัญญาณปฏิกิริยาออกซิเดชันของ UA, AA และ DA ออก
จากกันเป็น 3 สัญญาณได้อย่างชัดเจนในสภาวะที่มีความเป็นกรดสูง (พีเอช 1) ทำให้สามารถตรวจวัด
สารทั้งสามชนิดพร้อมกันได้อย่างมีประสิทธิภาพ เพราะในสภาวะกรดสามารถเปลี่ยนแปลงประจุและ
หมู่ฟังก์ชันบนพื้นผิวของ MC ได้ สัญญาณของ UA, AA และ DA มีการตอบสนองอย่างเป็นเส้นตรงอยู่
ในช่วง 10 – 150, 100 – 2,000 และ 10 – 150 ไมโครโมลาร์ ตามลำดับ ค่าขีดจำกัดต่ำสุดในการ
วิเคราะห์เชิงปริมาณ (LOQ) ของ UA, AA และ DA มีค่าเท่ากับ 5.2, 70.0 และ 0.6 ไมโครโมลาร์
ตามลำดับ นอกจากนี้ขั้วไฟฟ้ามีความไวในการวิเคราะห์ข้อมูลของ UA, AA และ DA เท่ากับ 93.5
 ± 2.6 , 6.8 ± 0.2 , 261.4 ± 3.4 ไมโครแอมแปร์ต่อตารางเซนติเมตรต่อมิลลิโมลาร์ ตามลำดับ ค่า
เปอร์เซ็นต์การได้กลับคืนจากการวิเคราะห์ด้วยเซนเซอร์ที่ได้ทำการพัฒนาขึ้นของ UA, AA และ DA มี

ค่าเท่ากับ 96, 102 และ 101 เปอร์เซ็นต์ ตามลำดับ ผลจากการศึกษาพบว่า เมื่อใช้เซนเซอร์ตรวจวัดทางเคมีไฟฟ้าที่พัฒนาขึ้นพบว่าสัญญาณขององค์ประกอบทั้ง 3 ชนิดไม่รบกวนซึ่งกันและกัน ทำให้สามารถนำไปประยุกต์ใช้ในการตรวจวัดปริมาณของสารทั้ง 3 ชนิดในปัสสาวะเทียมได้อย่างมีประสิทธิภาพสูง ทนต่อสารรบกวนในปัสสาวะเทียมและอยู่ในค่าที่ยอมรับได้

วิทยานิพนธ์เล่มนี้ได้ใช้ฮีมินเป็นตัวเร่งปฏิกิริยาสำหรับการวัดปริมาณแก๊สออกซิเจนในสภาวะที่เกลือมีความเข้มข้นสูงโดยใช้เทคนิคไซคลิกโวลแทมเมตรี คุณสมบัติของฮีมินจะช่วยเพิ่ม electrocatalytic activity ในปฏิกิริยาออกซิเจนรีดักชัน (Oxygen Reduction Reaction, ORR) เพราะไอออนของเหล็กที่มีเลขออกซิเดชัน +3 ที่อยู่ในรูปของสารละลายสามารถที่จะทำปฏิกิริยากับออกซิเจน (Oxygen, O₂) เกิดเป็นสารประกอบเชิงซ้อน $[(Fe^{III}) - O_2]$ จากผลการทดลองพบว่าเซนเซอร์ตรวจวัดออกซิเจนมีการตอบสนองอย่างเป็นเส้นตรงอยู่ในช่วง 65 - 610 ไมโครโมลาร์. ขีดจำกัดต่ำสุดในการวัด มีค่าเท่ากับ 11.79×10^{-6} ไมโครโมลาร์ นอกจากนี้ขั้วไฟฟ้ามีความไวในการวิเคราะห์ข้อมูล คือ 0.14 ไมโครแอมแปร์ต่อมิลลิโมลาร์ เซนเซอร์ชนิดนี้มีขีดการตรวจวัดที่ต่ำสามารถใช้วัดปริมาณออกซิเจนที่มีความเข้มข้นต่ำในตัวอย่างน้ำเสียได้ สามารถวัดได้ในตัวอย่างที่มีสารรบกวนหรือสารตัวอย่างที่มีปริมาณไอออนคลอไรด์สูง ส่วนใหญ่เป็นเกลือที่พบได้ในน้ำทะเล ไอออนของเกลือไม่รบกวนสัญญาณการตรวจวัดแบบอิเล็กโทรเคมีคัลเซนเซอร์ที่พัฒนาขึ้น ยกเว้นกรดแอสคอบิกที่ส่งผลต่อการวัดปริมาณออกซิเจนในสารตัวอย่างที่มีปริมาณไอออนคลอไรด์สูง นอกจากนี้เซนเซอร์ที่พัฒนาขึ้นยังมีความเสถียรและสามารถนำกลับมาใช้ซ้ำได้หลายครั้ง

สาขาวิชาเคมี
ปีการศึกษา 2566

ลายมือชื่อนักศึกษา ชัชกร วัฒนชัย
ลายมือชื่ออาจารย์ที่ปรึกษา ดร. อ.อ.อ.

TIDAPA RATTANAUMPA : SELECTIVE ELECTROCHEMICAL DETECTION OF MOLECULAR BIOMARKERS AT CARBON ELECTRODES. THESIS ADVISOR : ASSOC. PROF. KAMONWAD NGAMCHUEA, Ph.D. 147 PP.

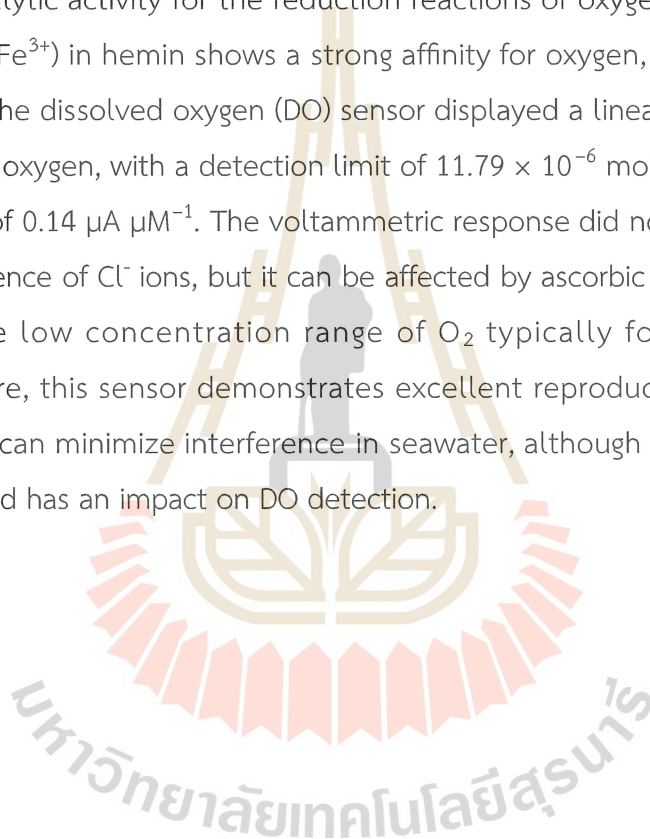
KEYWORD: MICROPOROUS CARBON/URIC ACID/ASCORBIC ACID/DOPAMINE/OXGEN SENSOR/HEMIN

This thesis focuses on the analysis of bodily fluids, including uric acid (UA), ascorbic acid (AA), and dopamine (DA). Abnormal levels of UA, DA, and AA could lead to specific diseases, and they can be measured by the use of electrochemical sensors with electrodes modified with various materials. Furthermore, various disorders may lead to the formation of hemin. Hemin is the chloro-coordinated prosthetic group of hemoglobin and is produced as a result of heme oxidation, serving as an oxygen carrier. This work investigates the oxygen reduction reaction (ORR) using hemin as an oxygen carrier in high-salt concentrations.

The electrode materials, including copper oxide (Cu_2O and CuO) and carbon (CNT and microporous carbon), were investigated for the oxidation of three molecular biomarkers: ascorbic acid, dopamine, and uric acid in human blood serum and urine samples. The low-cost microporous carbon (MC) electrode exhibits significantly better sensitivity and selectivity compared to other commonly used electrode materials (Cu_2O , CuO , and CNT). The voltammetric peaks of AA, DA, and UA at the microporous carbon electrode become better resolved in an acidic solution (HCl, pH 1) due to changes in the protonation states of the analyte and the surface functional groups of microporous carbon. Three well-resolved anodic peaks of AA, DA, and UA were identified at 0.27 V, 0.53 V, and 0.69 V, respectively, by comparing the DPV responses of the mixtures with those of the individual species. The sensitivity and limit of quantitation (LOQ) were found to be $6.8 \pm 0.2 \mu\text{A cm}^{-2} \text{mM}^{-1}$ and $70.0 \mu\text{M}$ for AA, $261.4 \pm 3.4 \mu\text{A cm}^{-2} \text{mM}^{-1}$ and $0.6 \mu\text{M}$ for DA, and $93.5 \pm 2.6 \mu\text{A cm}^{-2} \text{mM}^{-1}$ and $5.2 \mu\text{M}$ for UA. The linear range observed was 100 – 2,000 μM for AA, 10 – 150 μM for DA, and 10 – 150 μM for UA. The developed sensor was then validated in a synthetic urine sample, the percentage recoveries determined

by standard addition methods were 96%, 102%, and 101% for AA, DA, and UA, respectively, suggesting high accuracy of the method and excellent tolerance to possible interferences presented in the synthetic urine sample.

Hemin, a protoporphyrin IX containing a ferric iron (Fe^{3+}) ion, serves as the O_2 carrier and has been investigated as an electrocatalyst for detecting dissolved oxygen (DO) in high salt concentrations by the cyclic voltammetry technique (CV). The introduction of hemin in high salt concentrations significantly enhances the electrocatalytic activity for the reduction reactions of oxygen (ORR), because the ferric iron (Fe^{3+}) in hemin shows a strong affinity for oxygen, forming a $[(\text{Fe}^{\text{III}}) - \text{O}_2]$ complex. The dissolved oxygen (DO) sensor displayed a linear range in its catalytic reaction to oxygen, with a detection limit of $11.79 \times 10^{-6} \text{ mol L}^{-1}$ and an electrode sensitivity of $0.14 \mu\text{A } \mu\text{M}^{-1}$. The voltammetric response did not show any influence in the presence of Cl^- ions, but it can be affected by ascorbic acid. It can effectively detect the low concentration range of O_2 typically found in wastewater. Furthermore, this sensor demonstrates excellent reproducibility and long-term stability. It can minimize interference in seawater, although it is worth noting that ascorbic acid has an impact on DO detection.



School of Chemistry
Academic Year 2023

Student's Signature ชัชวาลย์ ใจดี
Advisor's Signature ประจักษ์ ใจดี

ACKNOWLEDGMENTS

I have learned and experienced many things during my Ph.D. journey. Therefore, I would like to express my sincere thanks to the many people who helped me complete my thesis, thus allowing me to achieve my goal of obtaining a Ph.D.

I would like to express my sincere gratitude to my thesis advisor, Associate Professor Kamonwad Ngamchuea, for providing me with the opportunity to pursue the study of electrochemistry. I am grateful for her invaluable assistance, kind support, insightful suggestions, and fruitful discussions throughout my thesis.

I am deeply grateful to the individuals in the Electrochemistry group, particularly Chochanon Moonla. Not only is she a kind and friendly individual, but her expertise in electrochemistry has been immensely valuable during my initial research endeavors. I also extend my thanks to Keerakit Keawkate, who possesses extensive knowledge in electrochemistry and is a pleasant person to work with. Additionally, I appreciate Sukanya Jankhunthod for her kindness, friendliness, and assistance, as well as Pachanuporn Sunon for their friendly demeanor and valuable support in the lab. My heartfelt thanks go out to all members of the Electrochemistry group and the School of Chemistry for their assistance and support, which has significantly contributed to the successful progression of my work.

Finally, I most gratefully acknowledge my parents for all their support, unconditional encouragement, and understanding during my studies.

Tidapa Rattanaumpa

CONTENTS

	Page
ABSTRACT IN THAI.....	I
ABSTRACT IN ENGLISH.....	III
ACKNOWLEDGEMENTS.....	V
CONTENTS.....	VI
LIST OF TABLES.....	XI
LIST OF FIGURES.....	XII
LIST OF ABBREVIATIONS.....	XXI
CHAPTER	
I INTRODUCTION.....	1
1.1 Background of the study.....	1
1.2 Objectives.....	7
1.3 References.....	7
II LITERATURE REVIEW.....	13
2.1 Electrochemistry.....	13
2.1.1 The principles of electrochemistry.....	13
2.1.1.1 Equilibrium electrochemistry.....	14
2.1.1.2 Dynamic electrochemistry.....	15
2.1.2 Reversible and irreversible behavior electrode kinetics.....	16
2.1.2.1 Reversible redox reaction.....	17
2.1.2.2 Irreversible redox reaction.....	18
2.1.3 Tafel analysis.....	19
2.1.4 Factors affecting electrode reaction rate and current.....	22
2.1.5 Mass transport.....	23
2.1.6 Adsorption and diffusion - controlled process.....	25
2.1.6.1 Adsorption-controlled process.....	25

CONTENTS (Continued)

	Page
2.1.6.2 Diffusion-controlled process.....	28
2.1.7 The principle of electrochemical methods.....	29
2.1.8 Electrodes used in electrochemistry.....	31
- Working electrode.....	31
- Reference electrode.....	31
- Counter electrode.....	32
2.1.9 Supporting electrolyte.....	33
2.1.10 Electrochemical technique.....	34
2.1.10.1 Cyclic voltammetry (CV).....	34
2.1.10.2 Differential pulse voltammetry (DPV).....	37
2.2 Uric acid, ascorbic acid and dopamine detection.....	38
2.2.1 Uric acid (UA).....	38
2.2.2 Ascorbic acid (AA).....	39
2.2.3 Dopamine (DA).....	40
2.2.4 The simultaneous determination of UA, AA and DA.....	40
2.2.4.1 Copper (II) oxide nanomaterials.....	41
2.2.4.2 Copper (I) oxide nanomaterials.....	42
2.2.4.3 Carbon nanotube nanomaterials.....	44
2.2.4.4 Microporous carbon (MC).....	46
2.2.5 The evaluation of the peroxide scavenging activity of UA.....	50
2.3 Oxygen detection.....	50
2.3.1 O ₂ solubility in electrolyte and sea water.....	38
2.3.2 Transition metal porphyrin complex.....	38
2.3.3 Oxygen reduction reaction (ORR) on transition metal porphyrin complex.....	57
2.3.4 Literature review of oxygen reduction reaction (ORR) on transition metal porphyrin complex.....	60
2.4 References.....	67

CONTENTS (Continued)

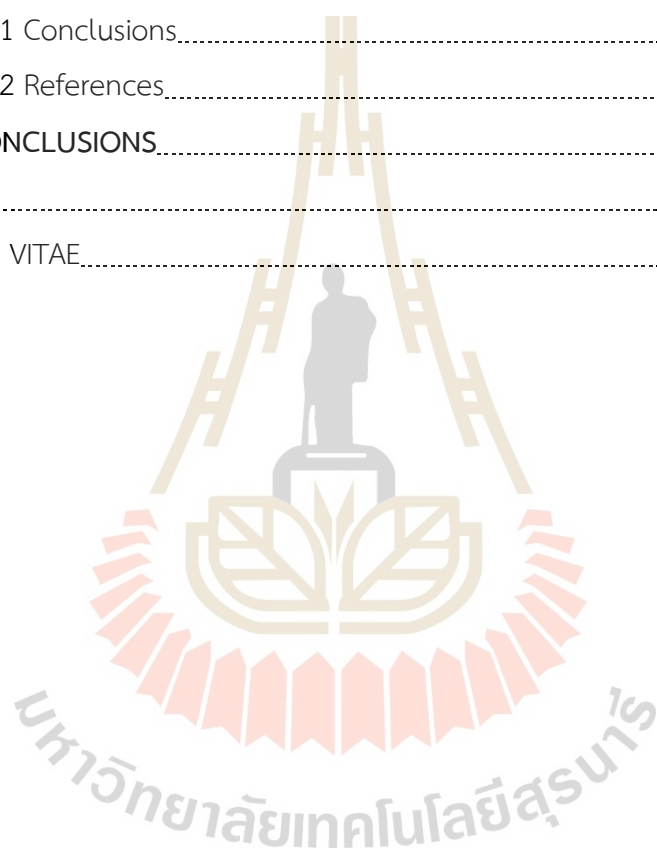
		Page
III	EXPERIMENTAL	76
	3.1 Uric acid, ascorbic acid and dopamine sensor.....	76
	3.1.1 Chemical reagents.....	76
	3.1.2 Electrochemical studies.....	77
	3.1.3 Electrode preparation and characterization.....	77
	3.1.4 Application to synthetic urine sample.....	78
	3.2 Oxygen sensor.....	79
	3.2.1 Chemical reagents.....	79
	3.2.2 Characterization of hemin and hemin solution.....	79
	3.2.3 Preparation of hemin solution at various KCl concentrations under saturated O ₂ conditions.....	79
	3.2.4 Preparation of hemin solution in high salt concentration in the absence of O ₂ molecules.....	80
	3.2.5 Preparation of O ₂ saturated 1.0 M KCl without hemin.....	80
	3.2.6 Effect of hemin concentration: Preparation of various hemin solution at saturated O ₂ concentrations.....	80
	3.2.7 Preparation of hemin solution at various O ₂ concentrations.....	81
	3.2.8 Electrochemical measurements.....	81
	3.3 References.....	82
IV	SELECTIVE ELECTRO-OXIDATION OF MOLECULAR BIOMARKERS AT MICROPOROUS CARBON ELECTRODES	83
	4. Result and discussion.....	83
	4.1 Effects of electrode material.....	83
	4.2 Characterization of microporous carbon.....	87
	4.3 Cyclic Voltammetry of AA, DA, and UA at MC/GCE.....	88
	4.3.1 Peak Identification.....	88
	4.3.2 Effects of pH.....	89
	4.3.3 Tafel analysis.....	91

CONTENTS (Continued)

		Page
	4.3.4 Effects of scan rates.....	92
	4.3.5 Effects of the amount of microporous carbon.....	95
	4.3.6 Calibration curve: CV.....	97
	4.4 Differential Pulse Voltammetry of AA, DA, and UA at MC/GCE.....	99
	4.4.1 Peak Identification.....	99
	4.4.2 Effects of DPV parameters.....	99
	4.4.3 Reproducibility tests.....	99
	4.4.4 Calibration curves: DPV.....	101
	4.5 Validation in synthetic urine.....	102
	4.6 Application of the developed sensor in the evaluation of peroxide scavenging activity of uric acid.....	104
	4.7 Conclusions.....	106
	4.8 References.....	106
V	CATALYSIS OF THE REDUCTION OF OXYGEN BY IRON (III) PORPHYRIN (HEMIN) AT GLASSY CARBON ELECTRODE IN HIGH SALT MICROPOROUS CARBON ELECTRODES.....	117
	5. Result and discussion.....	117
	5.1 Characterization of hemin.....	117
	5.2 The stability of the hemin solution color in electrolyte Solutions.....	119
	5.3 Electrochemical properties of hemin in high salt concentration without oxygen molecules.....	121
	5.4 Electrochemical properties of dioxygen in high salt concentration in the absence of hemin.....	122
	5.5 Electrochemical properties of hemin in high salt concentration with oxygen molecules.....	124
	5.6 Tafel analysis.....	131

CONTENTS (Continued)

	Page
5.7 Calibration plot.....	132
5.8 The effect of hemin as a catalyst in high salt concentration.....	133
5.9 Reproducibility.....	134
5.10 Interference.....	136
5.11 Conclusions.....	138
5.12 References.....	139
VI CONCLUSIONS.....	142
APPENDIX.....	144
CURRICULUM VITAE.....	147



LIST OF TABLES

Table		Page
2.1	The linear ranges, limits of detection (LOD), and sensitivities of different electrode materials employed in the electrochemical determination of AA, DA, and UA.....	48
2.2	Main constituents of seawater corresponding to a salinity of 35‰.....	51
2.3	Charge and radius properties of alkali metals in aqueous solution.....	54
2.4	Alkali metal chlorides hydration entropy.....	54
2.5	Comparison of the analytical performances of electrochemical DO sensor.....	65
5.1	Extinction coefficients of Hemin at 393 nm in aqueous solution and in 1.0 M KCl.....	118

LIST OF FIGURES

Figure	Page
Scheme	Electrocatalytic oxygen reduction of hemin at bare
1.1	GCE in high KCl concentration.....7
Scheme	Proposed reaction of O ₂ with a "face-to-face" binary Fe ²⁺
5.1	porphyrin. B is an axial base too large to fit in the cavity. Ovals represent porphyrin rings.....126
Scheme	Oxygen reduction mechanism by hemin in high salt
5.2	concentration.....127
2.1	Representation of (a) reduction and (b) oxidation process of a species, A, in solution. The molecular orbitals (MO) of species A shown are the highest occupied MO and the lowest vacant MO. These correspond in an approximate way to the E°s of the A/A ⁻ and A ⁺ /A couples, respectively.....16
2.2	Relationship of the transfer coefficient to the angles of intersection of the free energy curves.....19
2.3	Simple representation of standard free energy changes during a faradaic process, (a) At a potential corresponding to equilibrium, (b) At a more positive potential than the equilibrium value, (c) At a more negative potential than the equilibrium value.....20
2.4	Tafel slope.....22
2.5	Reaction profiles for a two-electron reduction.....22
2.6	Pathway of a general electrode reaction.....22
2.7	Schematics of three modes of mass transport.....24
2.8	The model of Bockris et al. of the double layer, arrangement of ions and solvent molecules; (<) represents a water molecule.....27

LIST OF FIGURES (Continued)

Figure	Page
2.9	Fick's 2 nd Law can be derived by considering the fluxes in and out of the 'slab'29
2.10	Variation with time of the concentration profiles of species A and B in the Cottrell experiment at a planar macroelectrode. The Nernst diffusion layer for t_1 (δ_1) is indicated on the graph. c_A^* is the bulk concentration of species A. $D_A = D_B$29
2.11	Three-electrode cell and notation for the different electrodes.....30
2.12	The processes of oxidation and reduction at an electrode.....30
2.13	Typical construction of a silver-silver chloride reference electrode.....32
2.14	Schematic image of the conventional three electrode cells.....32
2.15	Some supporting electrolytes and their approximate potential ranges in water and other solvents for platinum, mercury, and carbon.34
2.16	(A–G) Concentration profiles (mM) for Fc^+ (blue) and Fc (green) as a function of the distance from the electrode (d , from the electrode surface to the bulk solution, e.g.0.5 mm) at various points during the voltammogram. (H): Voltammogram of the reversible reduction of a 1.00 mM Fc^+ solution to Fc , at a scan rate of 100 mV s^{-1} . (I): Applied potential as a function of time for a generic cyclic voltammetry experiment, with the initial, switching, and end potentials represented (A, D, and G, respectively).....35
2.17	Macroelectrode.....36
2.18	Representation of the structure of glassy carbon.....37
2.19	Schematic of differential pulse voltammetry (A) Staircase waveform for differential pulse voltammetry and (B) differential

LIST OF FIGURES (Continued)

Figure	Page
	pulse voltammogram.....38
2.20	Uric acid (UA) structure.....38
2.21	Ascorbic acid (AA) structure.....39
2.22	Dopamine (DA) structure.....40
2.23	Dependences of the concentration of oxygen in sea water on its salinity at 25 °C from similar dependences of taken from various sources with extrapolation to higher salinity values.....53
2.24	Schematic representation of hydrogen bond network of water, (a) bulk water structure; (b) water structure in the presence of making ion; (c) water structure in the presence of breaking ion.....54
2.25	Different coordination of the Fe-N-C structure on graphene as a supporting material. Gray ball: carbon; Red ball: iron; Blue ball: nitrogen.....55
2.26	Hemin (Chloroporphyrin IX iron(III)).....55
2.27	Molecular structure of the iron porphyrin monomer (A), iron porphyrin dimer (B) and iron porphyrin in high salt concentration.....57
2.28	Possible configurations of dioxygen interaction with a metal in a complex.....58
2.29	Proposed reaction of O ₂ with a "face-to-face" binary Fe ²⁺ porphyrin. B is an axial base too large to fit in the cavity. Ovals represent porphyrin rings.....59
2.30	Interaction of O ₂ with heme and heme – O ₂ intermediates in heme proteins.....60

LIST OF FIGURES (Continued)

Figure	Page	
4.1	CV of 100 μM AA, 100 μM DA, and 100 μM UA in 0.10 M KCl (pH \sim 7) at different working electrodes: a) GCE, b) carbon nanotube (CNT/GCE), c) copper(II) oxide (CuO/GCE), d) copper(I) oxide (Cu ₂ O/GCE), e) microporous carbon (MC/GCE), f) Nafion-coated microporous carbon (Nafion/MC/GCE).....	86
4.2	CV of 500 μM AA, 100 μM DA, and 100 μM UA at Nafion/MC/GCE electrodes at different pH.....	87
4.3	a) SEM image, b) N ₂ adsorption-desorption isotherm, (inlay) a plot of $1/[Q(P_0/P-1)]$ against the relative pressure (P/P ₀) for the determination of BET surface area.....	88
4.4	CV of (Red) 100 μM AA, (Blue) 100 μM DA, (Black) 100 μM UA and (Green) the mixture of 100 μM AA, 100 μM DA, and 100 μM UA at MC/GCE in different electrolytes.....	89
4.5	CV of (a) 100 μM AA, (b) 100 μM DA, (c) 100 μM UA, and (d) 100 μM AA, DA, and UA mixture at MC/GCE in aqueous buffers of various pH: (black) pH 1.0, (red) pH 3.0, (blue) pH 5.0, (green) pH 7.0. E vs. Ag/AgCl (saturated KCl) RE.....	91
4.6	CV at bare GCE at varied scan rates of a) 100 μM UA and b) 100 μM AA, DA, UA. CV at MC/GCE at varied scan rates of c) 100 μM UA and d) 100 μM AA, DA, UA. (black) 10 mV s^{-1} , (red) 25 mV s^{-1} , (blue) 50 mV s^{-1} , (pink) 100 mV s^{-1} , (green) 200 mV s^{-1} , and (dark blue) 400 mV s^{-1}	94
4.7	CV of 1.0 mM hexaammineruthenium(III) in 0.10 M KCl at a bare GCE at varied scan rates (10 – 400 mV s^{-1}). The inlay shows a plot of cathodic peak currents against square root of scan rates.....	94

LIST OF FIGURES (Continued)

Figure	Page
4.8	96
<p>a) CV of 100 μM UA, and b) CV of 100 μM UA, AA, and DA at MC/GCE prepared using different amounts of microporous carbon. Inlays: the plots of I_p vs. the amount of microporous carbon. c) Average thickness of the dropcasted microporous carbon at different amounts (Inlay: confocal microscopic image of the MC (1.2 μg)/GCE surface). d) Optical profile of the MC (1.2 μg)/GCE surface.....</p>	
4.9	96
<p>The plot of electroactive surface areas of MP/GCE electrodes against the amount of immobilized microporous carbon.....</p>	
4.10	98
<p>CV of varied [AA] at a) bare GCE and b) MC/GCE. CV of varied [DA] at c) bare GCE and d) MC/GCE. CV of varied [UA] at e) bare GCE and f) MC/GCE. Electrolyte: 0.10 M HCl. Scan rate: 10 mV s^{-1}.....</p>	
4.11	101
<p>a) DPV of AA, DA, UA, the mixture of AA, DA, and UA, and a blank electrolyte. b) DPV of the mixture of AA, DA, and UA at different pulse amplitudes (10 – 200 mV). c) DPV of varied [AA] in the presence of 20 μM DA and 20 μM UA. d) DPV of varied [DA] in the presence of 500 μM AA and 50 μM UA, e) DPV of varied [UA] in the presence of 300 μM AA and 20 μM DA. Electrolyte: 0.10 M HCl. Electrode: MC/GCE. Scan rate: 10 mV s^{-1}. Otherwise stated: pulse amplitude = 10 mV and pulse width = 50 ms. E vs. Ag/AgCl (saturated KCl) reference electrode.....</p>	

LIST OF FIGURES (Continued)

Figure	Page
4.12	The calibration plots of DPV peak currents against the concentrations of a) AA, b) DA, and c) UA. Working electrode: MC/GCE. Electrolyte: 0.10 M HCl. Scan rate: 10 mV s ⁻¹102
4.13	DPV at MC/GCE electrode in the mixture of 2,500 μM AA, 100 μM DA, and 200 μM UA in 0.10 M HCl standard electrolyte vs. in synthetic urine sample in the presence of 0.10 M HCl at the pulse amplitude of 10 mV, the pulse width of 50 ms, and the scan rate of 10 mV s ⁻¹ . E vs. Ag/AgCl (saturated KCl) reference electrode.....104
4.14	% UA consumed after (black) 100 μM UA or (red) 100 μM UA were incubated with 0.0 – 50.0 mM H ₂ O ₂ for 24 hours.....105
4.15	a) UV-visible spectra and b) voltammograms of (red) 30 mM H ₂ O ₂ and (blue) 100 μM uric acid (UA).....105
5.1	(a) UV-visible spectra at varied hemin concentrations (6.25 – 21.88 μM) in aqueous 1.0 M KCl solutions. (b) FT-IR spectra of KCl, hemin solution (monomer) and hemin solution in KCl (dimer).....119
5.2	(a) 100 μM hemin solution in (A) 0.005 M KCl and (B) 0.020 M KCl, (C) 0.035 M KCl and (D) 0.050 M KCl after bubble O ₂ at the flow rate of 0.50 L/min for 3 minutes, (A) hemin solution without KCl, (B) hemin solution after bubble O ₂ gas, (C) hemin solution + 0.005 M KCl after bubble O ₂ gas, (D) hemin solution + 0.020 M KCl after bubble O ₂ gas, (E) hemin solution + 0.035 M KCl after bubble O ₂ gas, (E) hemin solution + 0.050 M KCl after bubble O ₂ gas and (b) % absorbance change at various KCl concentration.....120

LIST OF FIGURES (Continued)

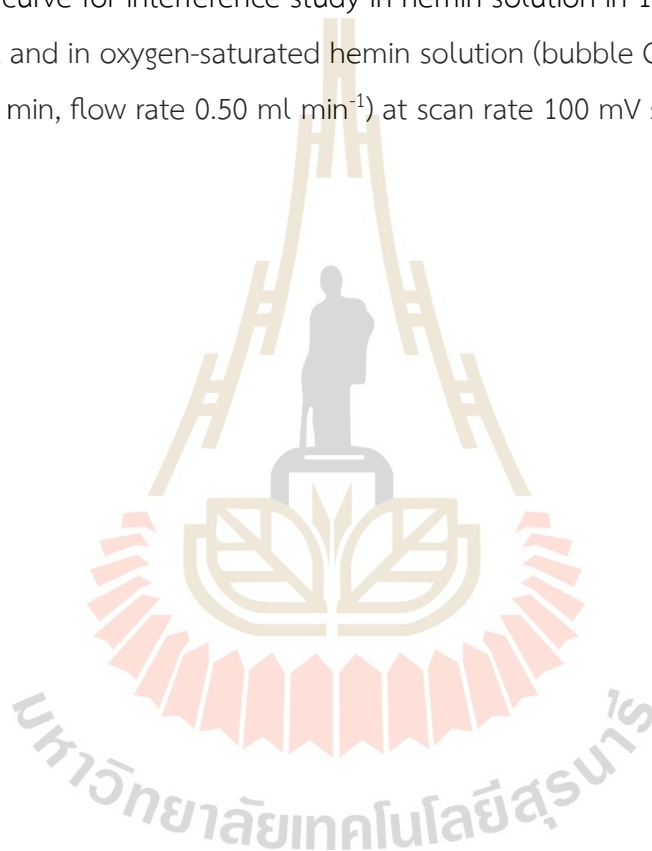
Figure	Page	
5.3	CV of varied Hemin concentration in deoxygenated 1.0 M KCl at a scan rate of 100 mV s^{-1} . (black) $0 \text{ }\mu\text{M}$, (red) $25 \text{ }\mu\text{M}$, (blue) $50 \text{ }\mu\text{M}$, (pink) $75 \text{ }\mu\text{M}$, and (green) $100 \text{ }\mu\text{M}$	121
5.4	CV of $200 \text{ }\mu\text{M}$ deoxygenated hemin in 1.0 M KCl at varied scan rate. The inlay shows the plot of the reduction peak currents against the square root of scan rate. (black) CV of $200 \text{ }\mu\text{M}$ deoxygenated hemin in 1.0 M KCl at varied scan rate. The inlay shows the plot of the reduction peak currents against the square root of scan rate. (black) 10 mV s^{-1} , (red) 25 mV s^{-1} , (blue) 50 mV s^{-1} , (pink) 100 mV s^{-1} , (green) 200 mV s^{-1} , and (dark blue) 400 mV s^{-1}	122
5.5	CV of O_2 -saturated 1 M KCl solution at varied scan rate. The inlay shows the plot of the reduction peak currents against the square root of scan rate. (black) 10 mV s^{-1} , (red) 25 mV s^{-1} , (blue) 50 mV s^{-1} , (pink) 100 mV s^{-1} , (green) 200 mV s^{-1} , and (dark blue) 400 mV s^{-1}	123
5.6	CV of O_2 -saturated and deoxygenated 1.0 M KCl solution at a scan rate of 100 mV s^{-1} . The inlay shows the plot of the reduction peak currents against the O_2 concentration.....	124
5.7	CV of $200 \text{ }\mu\text{M}$ hemin in 1.0 M KCl (black), hemin saturated with O_2 (red), hemin saturated with N_2 (blue), blank KCl (pink), blank KCl saturated with O_2 (green), at scan rate 100 mV s^{-1}	126
5.8	CV of $200 \text{ }\mu\text{M}$ hemin in 1.0 M KCl at bare GCE and at varied scan rates after bubble O_2 3.0 mins (flow rate 0.50 ml min^{-1}). (black) 10 mV s^{-1} , (red) 25 mV s^{-1} , (blue) 50 mV s^{-1} , (pink) 100 mV s^{-1} , (green) 200 mV s^{-1} , and (dark blue) 400 mV s^{-1}	129

LIST OF FIGURES (Continued)

Figure	Page	
5.9	Scan rate dependence of the cathodic peak current of O ₂ in O ₂ saturated hemin solution and O ₂ saturated 1.0 M KCl at bare GCE.....	129
5.10	CV of varied Hemin concentration ranging from 5 nM to 80 nM in 1 M KCl solution at a scan rate of 100 mV s ⁻¹ . The inlay shows the plot of the reduction peak currents against the Hemin concentration. (black) 0 nM, (red) 5 nM, (blue) 10 nM, (pink) 20 nM, (green) 40 nM, (dark blue) 60 nM, and (purple) 80 nM.....	130
5.11	CV of varied Hemin concentration ranging from 5 μM to 150 μM in 1.0 M KCl solution at a scan rate of 100 mV s ⁻¹ . The inlay shows the plot of the reduction peak currents against the Hemin concentration.....	130
5.12	Calibration of varied Hemin concentration ranging from 5 nM to 150 μM in 1.0 M KCl solution at a scan rate of 100 mV s ⁻¹	131
5.13	CV of 200 μM hemin in 1.0 M KCl at varied concentration of O ₂ by bubbling N ₂ gas (75.00 – 256.25 μM) and varied concentration calibration plot of O ₂ reduction of 200 μM hemin at varied concentration of O ₂).....	133
5.14	Comparison of the calibration plot between a deoxygenated and O ₂ -saturated hemin solution (black) and a deoxygenated and O ₂ -saturated 1.0 M KCl solution (red) at a scan rate of 100 mV s ⁻¹	134
5.15	Reproducibility and stability measurements: CV response of a 200 μM hemin solution at GCE in 1.0 M KCl at a flow rate of 0.50 L min ⁻¹ for 3.0 minutes by conducting five successive measurements.....	135

LIST OF FIGURES (Continued)

Figure		Page
5.16	Average reproducibility and stability measurements of O ₂ reduction in 200 μM hemin solution in 1.0 M KCl by conducting five successive measurements.....	135
5.17	CV curve for interference study in hemin solution in 1.0 M KCl and in oxygen-saturated hemin solution (bubble O ₂ in 3.0 min, flow rate 0.50 ml min ⁻¹) at scan rate 100 mV s ⁻¹	137



LIST OF ABBREVIATIONS

AA	Ascorbic acid
C^*	Bulk concentration of species i (mol m^{-3})
CE	Counter electrode
I	Current (A)
CV	Cyclic voltammetry
DPV	Differential pulse voltammetry
D_i	Diffusion coefficient of species i ($\text{m}^2 \text{s}^{-1}$)
δ	Diffusion layer thickness (m)
DA	Dopamine
A	Electrode area (m^2)
ϵ	Extinction coefficient ($\text{M}^{-1} \text{cm}^{-1}$)
F	Faraday constant (C mol^{-1})
GCE	Glassy carbon electrode
R	Molar gas constant ($\approx 8.314 \text{ J}\cdot\text{K}^{-1}\cdot\text{mol}^{-1}$)
n	Number of electron transfer
I_p	Peak current (A)
E	Potential applied to the working electrode (V)
RDS	Rate-determining step
RE	Reference electrode
RSD	Relative standard deviation
ν	Scan rate (V s^{-1})
T	Temperature (K)
β	The anodic transfer coefficient
α	The cathodic transfer coefficient

LIST OF ABBREVIATIONS (continued)

n'	The number of electron transfer before the rate determining step (RDS)
UA	Uric acid
V	Voltage (V)
WE	Working electrode



CHAPTER I

INTRODUCTION

1.1 Background of the study

Chemical sensors are employed to assess patient health by analyzing biofluids found in the human body, which may include uric acid (UA), dopamine (DA), ascorbic acid (AA), and hemin. (Ansah et al., 2022). These sensors play a crucial role in quantitative analysis of real samples to identify potential health risks. Abnormal levels of these compounds have been linked to several major diseases. UA, AA, and DA acid are vital molecules present in blood, urine, and saliva, each serving critical roles in protein metabolism, neurotransmission, and antioxidant functions. (Tukiman, Abdullah, and Sulaiman, 2018). UA is a natural byproduct of the body, formed during the breakdown of chemicals known as purines. (El Ridi and Tallima, 2017) AA serves as both a reducing agent and a potent antioxidant, playing a critical role in various physiological functions that protect the body against biological oxidation processes. (Yin et al., 2022). DA is associated with several mental health and neurological diseases due to its crucial role in regulating important bodily functions, including movement regulation in the brain. (Juarez Olguin, Caldero Guzman, Hernandez Garcia, and Barragan Mejia, 2016) Additionally, UA is a prominent antioxidant molecule in human blood, recognized for its exceptional ability to scavenge hydroxyl radicals (OH[•])

Several analytical methods have been employed in the detection of UA, AA, and DA, including mass spectrometry (Chen et al., 2013), high-performance liquid chromatography (Ye, Gao, and Li, 2014), colorimetry (Sohouli et al., 2020), fluorescence (Thanh et al., 2021) and biosensors (Li, Guo, Li, Dai, and Yang, 2014). However, the application of these methods in point-of-care settings is often limited by long analysis times, the complexity of sample preparation, and the requirement for expensive instruments. Electrochemical measurements have enabled rapid and

highly sensitive detection of redox-active analytes at a low cost. (Chaisiwamongkhon, Ngamchuea, Batchelor-McAuley, and Compton, 2016; Ngamchuea, Batchelor-McAuley, and Compton, 2018; Ngamchuea, Lin, Batchelor-McAuley, and Compton, 2017; Ngamchuea, Tharat, Hirunsit, and Suthirakun, 2020; Ngamchuea, Wannapaiboon, Nongkhunsan, Hirunsit, and Fongkaew, 2022) The electrochemical properties of UA, AA, and DA enable their quantitative determination via electrochemical methods. (Ngamchuea, Chaisiwamongkhon, Batchelor-McAuley, and Compton, 2018) Indeed, the similar redox properties of UA, AA, and DA lead to signals at similar potentials during electrochemical detection. Consequently, the primary challenges in their electrochemical detection include resolving overlapping oxidation peaks, overcoming electrode fouling issues, and enhancing measurement sensitivity.

Several electrode materials have been developed and employed to achieve these goals, mainly noble metals (e.g. Pt, Pd), metal oxides (e.g. Cu_2O , CuO), and carbon nanomaterials (e.g. carbon nanotube, graphene). (Krishnamoorthy, Sudha, Senthil Kumar, and Thangamuthu, 2018; Qi, Zhao, Tang, and Jiang, 2015; Sheng et al., 2012; Song et al., 2016; Sun, Lee, Yang, and Wu, 2011; C. Wang et al., 2014; C. Wang et al., 2016; H. Wang et al., 2014; Xia and Ning, 2011; S. Zhang, Xu, Liu, Chen, and Luo, 2019; Zhao, Yu, Tian, and Xu, 2016) Considering the cost and analytical performance, our focus herein is thus on the copper - and carbon - based materials. In this work, the performances of copper (II) oxide (CuO), copper (I) oxide (Cu_2O), carbon nanotube (CNT), and microporous carbon (MC) in the electrochemical detection of UA, AA, and DA are evaluated.

In particular, we will demonstrate the excellent performance of microporous carbon in enhancing the selectivity and sensitivity of measurements for UA, AA, and DA. The high conductivity, chemical stability, large surface area, and high microporosity of microporous carbon are key characteristics that significantly enhance the efficiency of electrochemical sensors. (Manocha et al., 2003; Xu et al., 2017) The selectivity of the measurement is influenced by differences in the diffusion rates of the analytes within the microporous structure. Additionally, potential interactions between the analytes and functional groups present on the microporous carbon surface, such as $-\text{OH}$, $-\text{COOH}$, $-\text{C}=\text{O}$, and $-\text{NH}_2$, can further facilitate electron transfer.

This enhances the sensitivity and selectivity of the electrochemical sensor. (Momtazan et al., 2018; Sohoulou et al., 2020)

In addition to developing a highly selective and sensitive electrochemical sensor for the detection of UA, AA, and DA, we further utilize UA as a paradigmatic example to showcase the sensor's potential in investigating reactive oxygen species (ROS) scavenging activity. UA is the primary antioxidant in human plasma, responsible for contributing up to approximately 50% of the total antioxidant activity. This contribution is notably higher than that of other antioxidants, such as AA (vitamin C) and vitamin E. (Amić et al., 2016) The excessive formation of free radicals, notably peroxy radicals (RO_2^*) and hydroxyl radicals (OH^*), accelerates the onset of chronic diseases, DNA damage, and carcinogenesis. (Ames, Cathcart, Schwiers, and Hochstein 1981; Amić et al., 2016) This work utilizes H_2O_2 , the primary source of OH^* radicals, as a model system to investigate scavenging properties.

Dissolved oxygen (DO) is a crucial parameter for monitoring water quality. Careful control of oxygen levels is essential for effective wastewater management and maintaining healthy marine environments. In seawater, the solubility of oxygen typically depends on salinity and temperature. (Zhang et al., 2022) As salinity levels increase, the DO concentration in water typically decreases. (MacArthur et al., 2002) DO and its correlation with salinity in marine environments are critical factors that profoundly affect aquatic life. A low concentration of DO can promote the growth of anaerobic bacteria, which have the potential to cause significant harm to the aquatic ecosystem, leading to permanent damage to the water system. Aquatic organisms typically require a minimum DO concentration of at least 4 mg L^{-1} for survival. (Hsu and Selvaganapathy, 2013)

In accordance with the principles of electrochemistry, a supporting electrolyte at a sufficient concentration was utilized to minimize ion migration phenomena and mitigate mass transport effects. The concentration of the supporting electrolyte, which is inert and does not interact with the electroactive species, typically falls within the range of 0.1 to 1.0 M. (Carucci, Salis, and Magner, 2017) Additionally, one of the challenges of DO sensors is the correlation between salt concentration and O_2 solubility, which affects the solubility and activity coefficient of O_2 . This phenomenon,

known as the "salting-out effect," results in a decrease in oxygen solubility with increasing ionic strength of the salt solution. (Buvik et al., 2021)

Traditional techniques for determining DO levels include titration (Winkler titration), chemiluminescence, optical fluorescence quenching, colorimetry, and the electrochemical sensor. (Fu, Zheng, Fu, Wang, and Cai, 2015) Moreover, interference from other substances remains an issue in the use of chemical, optical, and electrochemical methods.

The Winkler titration method is a titration analytical method used to quantify DO, ion interference can be a significant issue that affects the accuracy of the measurement, as interfering ions like sulfides (S^{2-}) and nitrites (NO_2^-) are often found in water samples. (Ingvorsen and Jorgensen 1979; Wong et al., 2012) They can react with the iodine (I_2) in the Winkler titration, causing the titration to prematurely reach the endpoint, which leads to an overestimation of the DO concentration. However, the extent of this interference largely depends on the experience and technique of the data collector.

Optodes, which rely on oxygen-dependent luminescence quenching, are commonly used for measuring DO in various environments. Optodes operate based on the dynamic quenching of luminescence by molecular oxygen. However, it's worth noting that several interferences, such as chlorine (Cl_2), sulfur dioxide (SO_2), and nitrogen dioxide (NO_2), can potentially interfere with the O_2 luminescence quenching process. (Dalfen, Pol, and Borisov, 2022)

Various techniques for electrochemical sensors to measure DO concentrations have garnered attention. Some of these techniques include polarographic oxygen sensors, often referred to as Clark sensors, coulometric capacitance respirometers, coulometric respirometers, and solid-state voltammetric electrodes. (Hsu and Selvaganapathy, 2013)

The commercial DO meter, Clark electrode or polarographic oxygen electrode, has three major limitations that affect the sensitivity of the DO sensor: (i) the Teflon membrane has low gas permeability to oxygen; (ii) Teflon is not effective in preventing biofouling and (iii) Clark electrodes are not considered inexpensive. The presence of

certain ions and biofouling can interfere with the sensor's ability to accurately measure the target parameter, which is typically oxygen. The presence of chloride ions in solution can be problematic because they can react with the silver electrode commonly used in Clark sensors. (Silva and Oliveira, 2012; Q. Wang, Cetó, and Valle, 2022) Biofouling can mask the sensor from its environment, leading to reduced sensitivity and eventual sensor failure. (Hsu and Selvaganapathy, 2013)

Most reported oxygen sensors have some drawbacks such as interference of other ions of the electrode. Hsu and Selvaganapathy studied electropolymerized polyhemin electrode without PDMS coating as the working electrode and silver as the conductive material which was used to verify its performance on sensing DO. Common interferences such as phosphate (PO_4^{3-}) and nitrate (NO_2^-) can result in a current shift of approximately 30-50% during DO sensing. (Hsu and Selvaganapathy, 2013) Hasebe et al. found that the electrocatalytic cathodic current for the reduction of O_2 , essential for highly sensitive voltammetric determination of respiratory toxins, was interfered with by cyanide (CN^-) and azide ion (N_3^-) in an air-saturated 0.1 mol L^{-1} phosphate/citrate buffer. (Hasebe and Wang, 2013)

Hemin, a metalloporphyrin complex and a transition metal N_4 -macrocycle, are generated when stomach enzymes and hydrochloric acid act on hemoglobin. (Kozlova et al., 2014) They indirectly influence the morphology of red blood cells and the structure of their membranes. The gradual accumulation of hemin can lead to the breakdown of red blood cells—a phenomenon associated with various disorders, including malaria, sickle cell disease, and ischemia, all of which trigger oxidation processes. Additionally, Hemin, with its porphyrin periphery structure and central metal ion, has been extensively studied as a catalyst for the electrochemical reduction of O_2 due to its structural similarity to cytochrome b and peroxidase. This similarity enables electron transfer in hemoproteins, as well as to the heme unit in myoglobin and hemoglobin. (Koichi Jeremiah Aoki, Li, Chen, and Nishiumi, 2014; Hsu and Selvaganapathy, 2013; Kolpin and Swofford, 2002; Xia, Liu, Sun, and Zhou, 2015; Gorton et al., 1999; Y. Wang, Hosono, and Hasebe, 2013; Hasebe and Wang, 2013; Y. Wang, Hosono, and Hasebe, 2013) The most frequently investigated structures of metalloporphyrin are μ -oxo-bridged dimers. (Dziedzic-Kocurek, Byrne, Świdorski, and

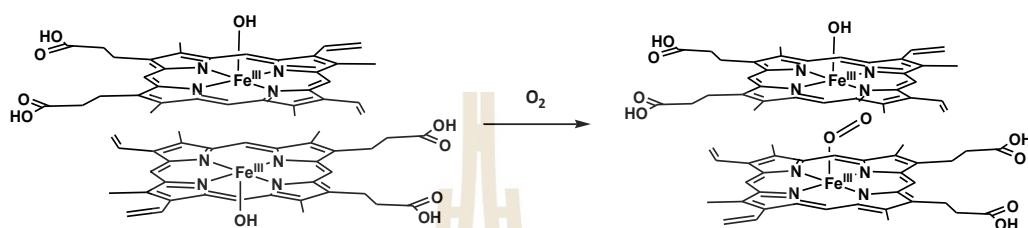
Stanek, 2009) Normally, the transition metals and the chelating atoms of the macrocyclic ring can also change the ORR activity.

The function of transition metal complexes, such as Fe, Mn, Cu, Ni, and Co, with unpaired d-electrons and multi-electron redox processes, is to serve as active centers and O₂ binding sites. This facilitates the activation of O₂ through metal coordination, ultimately leading to the formation of reactive intermediates. (Lu, Wang, and Qin, 2022) Iron (Fe) exhibits higher reactivity for O₂ reduction compared to Co, Ni, Cu, and Mn, with the order of reactivity being Fe > Co > Ni > Cu > Mn. (Collman, Elliott, Halbert and Tovrog 1977) For the chelating atoms of the macrocyclic ring, the active sequence of Fe complexes is as follows: N₄ > N₂O₂ > N₂S₂ > O₄ ≈ S₄ (Si et al., 2014) This higher reactivity makes iron accessible for direct electrochemical redox activity, and the results are highly electrode-sensitive. (Sokolov, Sepunaru, and Compton, 2017) Normally, Fe-based N₄ catalysts (Fe-N₄) for the ORR takes a four-electron transfer pathway to produce H₂O. (Si et al., 2014)

The mechanism of the O₂ reduction reaction proceeds through either a direct four-electron pathway or a two-electron pathway, which is influenced by the nature of the electrode material and the electrolyte used. (Ardakani, Karami, Zare, and Hamzehloo, 2007; Šljukić, Banks, and Compton, 2005) Various types of carbon-based electrodes have been investigated for the oxygen reduction reaction. Glassy carbon (GC) electrodes facilitate a two-electron process during the oxygen reduction reaction, resulting in the generation of hydrogen peroxide as an end product at the cathode surface. (Ardakani et al., 2007; Šljukić et al., 2005) The catalytic activity of the electrode surface dictates the rate of the electrochemical process. Metallodiporphyrins can catalyze the oxygen reduction reaction to produce either water (H₂O) via a four-electron process or hydrogen peroxide (H₂O₂) via a two-electron process. The specific process that occurs depends on the geometric and electronic properties of the metallodiporphyrins. (Šljukić et al., 2005)

In this study, we introduce a simple sensor employing hemin as a mediator to quantify oxygen concentration. The electrocatalytic reduction of oxygen by hemin was investigated in high salt concentrations using cyclic voltammetry (CV) on a bare glassy carbon electrode. The presence of hemin in a KCl solution enhances electron

transfer efficiency and catalyzes the reduction of O_2 at the glassy carbon electrode surface, thereby accelerating the overall electrocatalytic reduction of O_2 . This study investigates the impact of electrolyte concentration and increasing ionic strengths on the stability and activity of hemin towards the reduction of O_2 . Additionally, the study evaluates electrode stability and potential ion interference in high salt concentrations.



Scheme 1.1 Electrocatalytic oxygen reduction of hemin at bare GCE in high KCl concentration.

1.2 Objectives

- 1.2.1 To study the electrochemical behavior of AA, DA and UA at copper oxides (Cu_2O and CuO), carbon nanotube (CNT), and microporous carbon (MC) electrodes.
- 1.2.2 To evaluate the peroxide scavenging activity of UA.
- 1.2.3 To investigate the oxygen reduction reaction (ORR) facilitated by hemin in high salt concentrations.

1.3 References

- Ames, B. N., Cathcart, R., Schwiers, E., and Hochstein, P. (1981). Uric acid provides an antioxidant defense in humans against oxidant- and radical-caused aging and cancer: a hypothesis. *Proc. Natl. Acad. Sci. U. S. A.*, 78(11), 6858-6862.
- Amić, A., Marković, Z., Dimitrić M., J. M., Lučić, B., Stepanić, V., and Amić, D. (2016). The $2H^+/2e^-$ free radical scavenging mechanisms of uric acid: thermodynamics of NH bond cleavage. *Comput. Theor. Chem.*, 1077, 2-10.
- Ansah, I. B., Lee, W.-C., Mun, C., Rha, J.-J., Jung, H. S., Kang, M., Park, S.-G., and Kim, D.-H. (2022). In situ electrochemical surface modification of Au electrodes for

- simultaneous label-free SERS detection of ascorbic acid, dopamine and uric acid. *Sens. Actuators B: Chem.*, 353.
- Ardakani, M. M., Karami, P. E., Zare, H. R., and Hamzehloo, M. (2007). Electrocatalytic reduction of oxygen on the surface of glassy carbon electrodes modified with plumbagin. *Mikrochim. Acta*, 159(1-2), 165-173.
- Chaisiwamongkhol, K., Ngamchuea, K., Batchelor-McAuley, C., and Compton, R. G. (2016). Electrochemical detection and quantification of gingerol species in ginger (*Zingiber officinale*) using multiwalled carbon nanotube modified electrodes. *Analyst*, 141(22), 6321-6328.
- Chen, S., Zheng, H., Wang, J., Hou, J., He, Q., Liu, H., Xiong, C., Kong, X., and Nie, Z. (2013). Carbon nanodots as a matrix for the analysis of low-molecular-weight molecules in both positive-and negative-ion matrix-assisted laser desorption/ionization time-of-flight mass spectrometry and quantification of glucose and uric acid in real samples. *Anal. Chem.*, 85(14), 6646-6652.
- El Ridi, R., and Tallima, H. (2017). Physiological functions and pathogenic potential of uric acid: A review. *J. Adv. Res.*, 8(5), 487-493.
- Hasebe, Y., and Wang, Y. (2013). Sensitive voltammetric and amperometric responses of respiratory toxins at hemin-adsorbed carbon-felt. *J. Environ. Sci. (China)*, 25(6), 1055-1062.
- Hsu, L. H. H., and Selvaganapathy, P. R. (2013, 3-6 Nov. 2013). Development of a low cost Hemin based dissolved oxygen sensor with anti-biofouling coating for water monitoring. Paper presented at the SENSORS, 2013 IEEE.
- Juarez Olguin, H., Calderon Guzman, D., Hernandez Garcia, E., and Barragan Mejia, G. (2016). The role of dopamine and Its dysfunction as a consequence of oxidative stress. *Oxid. Med. Cell. Longev.*, 2016, 9730467.
- Kozlova, E., Chernysh, A., Moroz, V., Gudkova, O., Sergunova, V., and Kuzovlev, A. (2014). Transformation of membrane nanosurface of red blood cells under hemin action. *Sci Rep*, 4, 6033.
- Krishnamoorthy, K., Sudha, V., Senthil Kumar, S. M., and Thangamuthu, R. (2018). Simultaneous determination of dopamine and uric acid using copper oxide nano-rice modified electrode. *J. Alloys Compd.*, 748, 338-347.

- Li, M., Guo, W., Li, H., Dai, W., and Yang, B. (2014). Electrochemical biosensor based on one-dimensional MgO nanostructures for the simultaneous determination of ascorbic acid, dopamine, and uric acid. *Sens. Actuators B: Chem.*, *204*, 629-636.
- Lin, K.-C., Yin, C.-Y., and Chen, S.-M. (2011). Simultaneous determination of AA, DA, And UA based on bipolymers by electropolymerization of luminol And 3,4-ethylenedioxythiophene monomers. *Int. J. Electrochem. Sci.*, *6*(9), 3951-3965.
- MacArthur, C. G. (2002). Solubility of oxygen in salt solutions and the hydrates of these salts. *J. Phys. Chem.*, *20*(6), 495-502.
- Manocha, S. M. (2003). Porous carbons. *Sadhana*, *28*(1-2), 335-348.
- Momtazan, F., Vafaei, A., Ghaedi, M., Ghaedi, A. M., Emadzadeh, D., Lau, W.-J., and Baneshi, M. M. (2018). Application of copper sulfide nanoparticles loaded activated carbon for simultaneous adsorption of ternary dyes: Response surface methodology. *Korean J. Chem. Eng.*, *35*(5), 1108-1118.
- Ngamchuea, K., Batchelor-McAuley, C., and Compton, R. G. (2018). Understanding electroanalytical measurements in authentic human saliva leading to the detection of salivary uric acid. *Sens. Actuators B: Chem.*, *262*, 404-410.
- Ngamchuea, K., Chaisiwamongkhol, K., Batchelor-McAuley, C., and Compton, R. G. (2018). Chemical analysis in saliva and the search for salivary biomarkers—a tutorial review. *Analyst*, *143*(1), 81-99.
- Ngamchuea, K., Lin, C., Batchelor-McAuley, C., and Compton, R. G. (2017). Supported microwires for electroanalysis: sensitive amperometric detection of reduced glutathione. *Anal. Chem.*, *89*(6), 3780-3786.
- Ngamchuea, K., Tharat, B., Hirunsit, P., and Suthirakun, S. (2020). Electrochemical oxidation of resorcinol: mechanistic insights from experimental and computational studies. *RSC advances*, *10*(47), 28454-28463.
- Ngamchuea, K., Wannapaiboon, S., Nongkhunsan, P., Hirunsit, P., and Fongkaew, I. (2022). Structural and electrochemical analysis of copper-creatinine complexes: Application in Creatinine Detection. *J. Electrochem. Soc.*, *169*(2), 020567.

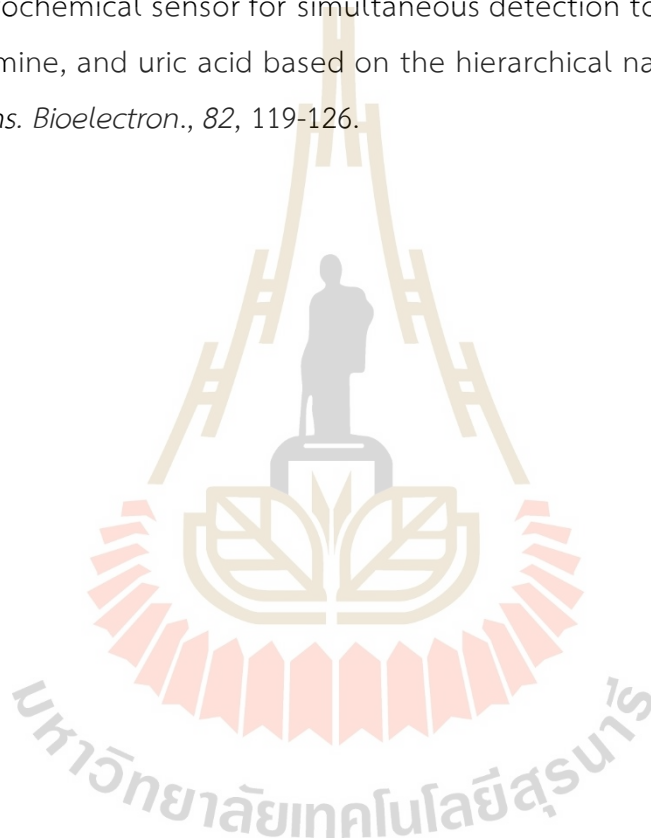
- Qi, S., Zhao, B., Tang, H., and Jiang, X. (2015). Determination of ascorbic acid, dopamine, and uric acid by a novel electrochemical sensor based on pristine graphene. *Electrochim. Acta*, *161*, 395-402.
- Si, F., Zhang, Y., Yan, L., Zhu, J., Xiao, M., Liu, C., Xing, W., and Zhang, J. (2014). 4 - electrochemical oxygen reduction reaction. In W. Xing, G. Yin, and J. Zhang (Eds.), *Rotating Electrode Methods and Oxygen Reduction Electrocatalysts* (pp. 133-170). Amsterdam: Elsevier.
- Sheng, Z.-H., Zheng, X.-Q., Xu, J.-Y., Bao, W.-J., Wang, F.-B., and Xia, X.-H. (2012). Electrochemical sensor based on nitrogen doped graphene: simultaneous determination of ascorbic acid, dopamine and uric acid. *Biosens. Bioelectron.*, *34*(1), 125-131.
- Šljukić, B., Banks, C. E., and Compton, R. G. (2005). An overview of the electrochemical reduction of oxygen at carbon-based modified electrodes. *J. Iran. Chem. Soc.*, *2*(1), 1-25.
- Sohouli, E., Khosrowshahi, E. M., Radi, P., Naghian, E., Rahimi-Nasrabadi, M., and Ahmadi, F. (2020). Electrochemical sensor based on modified methylcellulose by graphene oxide and Fe₃O₄ nanoparticles: Application in the analysis of uric acid content in urine. *J. Electroanal. Chem.*, *877*, 114503.
- Song, Y., Gong, C., Su, D., Shen, Y., Song, Y., and Wang, L. (2016). A novel ascorbic acid electrochemical sensor based on spherical MOF-5 arrayed on a three-dimensional porous carbon electrode. *Anal. Methods*, *8*(10), 2290-2296.
- Sun, C. L., Lee, H. H., Yang, J. M., and Wu, C. C. (2011). The simultaneous electrochemical detection of ascorbic acid, dopamine, and uric acid using graphene/size-selected Pt nanocomposites. *Biosens Bioelectron*, *26*(8), 3450-3455.
- Thanh, T. S., Qui, P. T., Tu, N. T. T., Toan, T. T. T., Hoa, T. T. B., Son, L. V. T., Nguyen, D. M., Tuyen, T. N., and Khieu, D. Q. (2021). Electrochemical determination of uric acid in urine by using zeolite imidazolate framework-11 modified electrode. *J. Nanomater.*, 2021.
- Toader, A. M., Volanschi, E., Lazarescu, M. F., and Lazarescu, V. (2010). Redox behavior of hemin at p-GaAs(1 0 0) electrode. *Electrochim. Acta*, *56*(2), 863-866.

- Tukimin, N., Abdullah, J., and Sulaiman, Y. (2018). Review—Electrochemical detection of uric acid, dopamine and ascorbic acid. *J. Electrochem. Soc.*, *165*(7), B258-B267.
- Wang, C., Du, J., Wang, H., Zou, C. e., Jiang, F., Yang, P., and Du, Y. (2014). A facile electrochemical sensor based on reduced graphene oxide and Au nanoplates modified glassy carbon electrode for simultaneous detection of ascorbic acid, dopamine and uric acid. *Sens. Actuators B: Chem.*, *204*, 302-309.
- Wang, C., Li, J., Shi, K., Wang, Q., Zhao, X., Xiong, W. Z., Zou, X., and Wang, Y. (2016). Graphene coated by polydopamine/multi-walled carbon nanotubes modified electrode for highly selective detection of dopamine and uric acid in the presence of ascorbic acid. *J. Electroanal. Chem.*, *770*, 56-61.
- Wang, H., Ren, F., Wang, C., Yang, B., Bin, D., Zhang, K., and Du, Y. (2014). Simultaneous determination of dopamine, uric acid and ascorbic acid using a glassy carbon electrode modified with reduced graphene oxide. *RSC Advances*, *4*(51), 26895-26901.
- Wang, Y., Hosono, T., and Hasebe, Y. (2013). Hemin-adsorbed carbon felt for sensitive and rapid flow-amperometric detection of dissolved oxygen. *Mikrochim. Acta*, *180*(13-14), 1295-1302.
- Xia, C., and Ning, W. (2011). A novel bio-electrochemical ascorbic acid sensor modified with Cu₄(OH)₆SO₄ nanorods. *Analyst*, *136*(2), 288-292.
- Xu, M., Li, D., Yan, Y., Guo, T., Pang, H., and Xue, H. (2017). Porous high specific surface area-activated carbon with co-doping N, S and P for high-performance supercapacitors. *RSC advances*, *7*(69), 43780-43788.
- Ye, N., Gao, T., and Li, J. (2014). Hollow fiber-supported graphene oxide molecularly imprinted polymers for the determination of dopamine using HPLC-PDA. *Anal. Methods*, *6*(18), 7518-7524.
- Yin, X., Chen, K., Cheng, H., Chen, X., Feng, S., Song, Y., and Liang, L. (2022). Chemical stability of ascorbic acid integrated into commercial products: A Review on Bioactivity and Delivery Technology. *Antioxidants (Basel)*, *11*(1).
- Zhang, S., Xu, F., Liu, Z. Q., Chen, Y. S., and Luo, Y. L. (2019). Novel electrochemical sensors from poly[N-(ferrocenyl formacyl) pyrrole]@multi-walled carbon

nanotubes nanocomposites for simultaneous determination of ascorbic acid, dopamine and uric acid. *Nanotechnology*, 31(8), 085503.

Zhang, Y., Zhang, Y., Yuan, D., Zhang, Y., Wu, B., and Feng, X. (2022). Calibration method of multi-parameter compensation for optical dissolved oxygen sensor in seawater based on machine learning algorithm. *Deep-Sea Res. I: Oceanogr. Res. Pap.*, 188.

Zhao, D., Yu, G., Tian, K., and Xu, C. (2016). A highly sensitive and stable electrochemical sensor for simultaneous detection towards ascorbic acid, dopamine, and uric acid based on the hierarchical nanoporous PtTi alloy. *Biosens. Bioelectron.*, 82, 119-126.



CHAPTER II

LITERATURE REVIEW

2.1 Electrochemistry

Electrochemistry is the branch of chemistry concerned with understanding the relationship between electrical and chemical effects. It specifically focuses on chemical reactions that affect the transport of charge across the interface between an electronic conductor (an electrode) and an ionic conductor (an electrolyte), particularly those involving the transfer of electrons. The conversion between chemical energy and electrical energy is a fundamental aspect of electrochemistry. Redox (reduction-oxidation) reactions form the foundation of electrochemical processes. (Moeller et al., 1980)

Electrochemical reactions occur when a solid electron conductor (electrode) is immersed in an ionic conductor (supporting electrolyte). This basic system, consisting of the electrode and electrolyte, is known as a half-cell. When two half-cells are connected with similar phases, they form an electrochemical cell. This cell enables the flow of electrical charge, involving the transfer of electrons and ions. Electrochemistry investigates a wide range of individual and interfacial characteristics, including solid-state physics, thermodynamics, kinetics of electrolyte, charge and electron transfer processes, and interfacial electrode processes.

2.1.1 The principles of electrochemistry

In electrochemical systems, this technique refers to the transfer of charge across the interface between an electrode, which acts as an electronic conductor, and an electrolyte, which serves as an ionic conductor. When an electric potential is applied and current flows at the electrode/electrolyte interface, charge is transported through the electrode by the movement of electrons (and holes). (Bard et al., 2002) The principles of electrochemistry can be divided into two main categories: equilibrium electrochemistry, which examines the inherent properties of ions, the

thermodynamics of electrolytes, and electrochemical cells operating at equilibrium; and dynamic electrochemistry, which focuses on kinetics, including electrode/electrolyte interfacial phenomena and charge transfer processes. (Bard et al., 2002)

2.1.1.1 Equilibrium electrochemistry

In a system at equilibrium, the basic component is an electrochemical cell consisting of two electrodes (sources of electrons) immersed in an electrolyte (a conductor of ions). Electrolytes and electrochemical cells reach equilibrium when no current passes through the electrochemical cell, with equilibrium occurring at the electrode/electrolyte interface. With a potential difference, the reaction involves the transfer of charged particles and electrons between the dissolved A ions and the electrons in the metal electrode. The A ions lose electrons to the metal electrode, which are said to be oxidized. Conversely, electrons from the metal electrode transfer to the A ions, which are said to be reduced (Compton and Banks, 2007).



The electron transfer mechanism is described as follows: The electronic structure of a metal consists of an effective continuum filled up to an energy maximum known as the Fermi level. In contrast, the electronic structure of the solution phase species (A and B) is discrete. When electron transfer occurs between the electrode and the solution, the Fermi level of the metal is higher than the lowest unoccupied molecular orbital (LUMO) of the A ion. Therefore, it is energetically favorable for electrons to move from the metal to the LUMO of A. The energy difference serves as the driving force for the electron transfer process from the metal to the A solution. The decrease in the energy of the Fermi level of the metal contributes to the reduction of A to B. In a dynamic equilibrium of this type, the concentrations of A and B do not measurably change, and A and B reach an equilibrium state (Brett and Brett, 1993). The electrode reaction is often described as thermodynamically or electrochemically reversible (or Nernstian), providing a linkage

between electrode potential and the concentrations of participants in the electrode process.

2.1.1.2 Dynamic electrochemistry

In dynamic electrochemistry, the cell potential undergoes changes upon applying a potential to the electrode. The applied potential has the ability to alter the direction of electron transfer, causing a disturbance in the Fermi level of the electrode. This results in a potential difference at the electrode/electrolyte interface, leading to the formation of an electrical double layer. A current begins to flow through the electrochemical cell at the electrode/electrolyte interface. This process is referred to as dynamic electrochemistry. In the mechanism of an electrode reaction, applying different potentials to the electrode can alter the direction of electron transfer. The Fermi level, defined as the average energy of available electrons or the chemical potential of electrons in that phase, can be adjusted by varying the applied potentials. In a reduction process, there is a flow of electrons from the electrode to the solution, resulting in the reduction current. When a negative potential is applied to the electrode, the energy of the electrons, or the Fermi level on the electrode, is raised. This increased energy enables the electrons to reach a level high enough to transfer into vacant electronic states in the electrolyte. The increased availability of electrons at the electrode surface can promote electron transfer from the metal to species in the solution, facilitating the reduction reaction. Conversely, when a more positive potential is applied, the energy of the electrons on the electrode can be lowered, making the electrolyte more energetically favorable on the electrode. In this case, electrons transfer from the solution to the electrode, resulting in an oxidation current (**Figure 2.1**) (Brett and Brett, 1993).

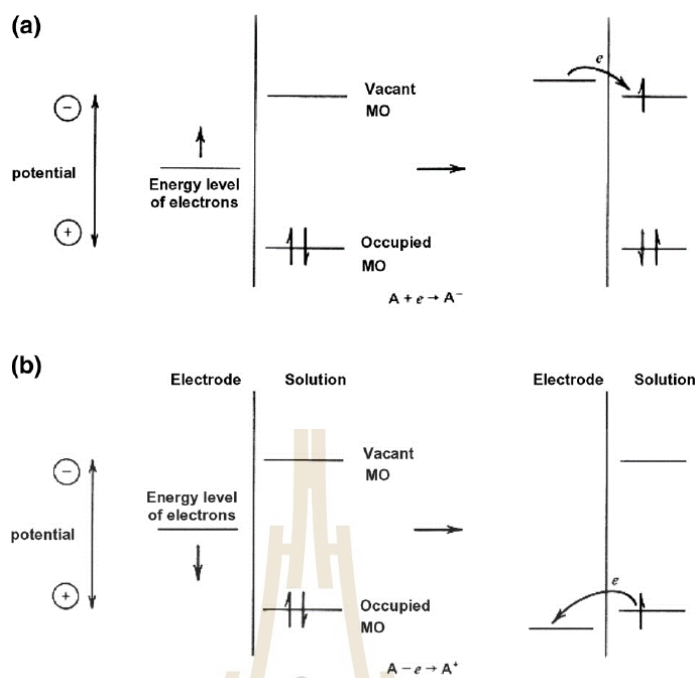


Figure 2.1 Representation of (a) reduction and (b) oxidation process of a species, A, in solution. The molecular orbitals (MO) of species A shown are the highest occupied MO and the lowest vacant MO. These correspond in an approximate way to the E° s of the A/A^- and A^+/A couples, respectively (Bard et al., 2002).

2.1.2 Reversible and irreversible behavior electrode kinetics

In both reversible and irreversible systems, electrons are transferred in more than one step. These systems are divided into two categories:

In the case of a reversible reaction where both forward and reverse reactions occur, the reaction proceeds rapidly and reversibly. This implies that the Nernst equation can be applied when $|E| \geq E_{eq}$, where E and E_{eq} are the electrode potential and equilibrium potential, respectively.

In the case of an irreversible reaction, the slowest reaction is the rate-determining step (RDS). The kinetic parameter (transfer coefficient, α) can be applied, which is built around the rate of this RDS and results in the curve having a lower slope compared to a reversible reaction.

Moreover, fast and slow electrode kinetics are related to the rate of mass transport to the electrode. The kinetic rate constants depend on the applied potential and the value of the standard rate constant, K_0 . The mass transfer

coefficient (K_d) describes the rate of diffusion within the diffusion layer, which is influenced by the thickness of the diffusion layer (Brett and Brett, 1993).

$$K_0 \gg K_d ; \text{ reversible system} \quad (2.2)$$

$$K_0 \ll K_d ; \text{ irreversible system} \quad (2.3)$$

2.1.2.1 Reversible redox reaction

For a reversible redox reaction, $K_0 \gg K_d$, a reversible reaction is kinetically fast enough to maintain Nernstian (i.e. reversible) behavior. This implies that the system can be assumed to be in equilibrium at all times at the electrode surface with respect to the electrode potential. A fully reversible cyclic voltammogram for an ideal reversible surface-adsorbed redox couple exhibits symmetric and well-defined peaks during both the oxidation and reduction processes, indicating a rapid and reversible electron transfer between the oxidized and reduced forms of the redox couple, as governed by Nernst equation for the half-reaction.

The Nernst equation is used to predict the behavior of redox reactions based on changes in concentration or electrode potential. It provides a powerful means of forecasting how a reaction will respond to changes in the concentration of species in the solution, corresponding to alterations in the electrode potential. During the cyclic voltammetry (CV) experiment, as the potential is scanned, the concentration of species in the solution near the electrode changes over time in accordance with the Nernst equation (equation (2.4)).

$$E = E^0 + \frac{RT}{nF} \ln \frac{(O)}{(R)} = E^0 + 2.3026 \frac{RT}{nF} \log \frac{(O)}{(R)} \quad (2.4)$$

In the equation, F is Faraday's constant, R is the universal gas constant, n is the number of electrons, and T is the temperature.

The peak current of a single n -electron electrochemically reversible reduction is given by

$$I_p = 0.446nFAc^* \sqrt{\frac{nFvD}{RT}} \quad (2.5)$$

Where I_p is the peak current, n is the total number of electrons transfer, A is the electrode surface area, D is the diffusion coefficient, c^* is the bulk concentration, v is the voltage scan rate, F is the Faraday constant ($96,485 \text{ C mol}^{-1}$), R is the molar gas constant ($8.314 \text{ J K}^{-1} \text{ mol}^{-1}$), and T is the absolute temperature.

2.1.2.2 Irreversible redox reaction

In irreversible redox reactions in electrochemistry, where $K_0 \leq K_d$, occur when the charge transfer step is very sluggish or exhibits slow kinetics. In such cases, the product of the forward reaction reacts chemically, leaving nothing for the reverse reaction to act upon (Hibbert et al., 1993).

There is no equilibrium existing between the surface and bulk concentrations. The half-wave potential for reduction or oxidation varies with K_d . Thus, it is necessary to apply a high potential to overcome the activation barrier and allow oxidation or reduction reactions to occur because electrochemical irreversibility corresponds to slow electrode kinetics.

In the case of an irreversible reaction, additional kinetic parameters are introduced. Here, n' represents the number of electron transfers before the rate-determining step (RDS), and $\alpha_{n'+1}$ denotes the cathodic transfer coefficient of the rate-determining step. The presence of the factor $\alpha_{n'+1}$ with $0 < \alpha_{n'+1} < 1$ signifies the significant influence of the rate of electron transfer on the voltammetric response (Compton and Banks, 2007; Christensen and Hamnet, 1993). For a completely irreversible n -electron wave, the following expression for the peak current is applicable (Compton and Banks, 2007).

$$I_p = 0.496 \sqrt{n' + \alpha_{n'+1}} n F A c^* \sqrt{\frac{F v D}{RT}} \quad (2.6)$$

Where I_p is the peak current, n' is the number of electron transfer before the rate determining step, n is the total number of electrons transfer ($n=4$), $\alpha_{n'+1}$ is the cathodic transfer coefficient of the rate determining step, A is the electrode surface area, D is the diffusion coefficient, c^* is the bulk concentration, v is

the voltage scan rate, F is the Faraday constant ($96,485 \text{ C mol}^{-1}$), R is the molar gas constant ($8.314 \text{ J K}^{-1} \text{ mol}^{-1}$), and T is the absolute temperature.

2.1.3 Tafel analysis

A model of electrode kinetics known as Tafel analysis is an example of a linear free energy relation between a kinetic and a thermodynamic parameter, specifically the flux (or the current) and the potential (Brett and Brett, 1993).

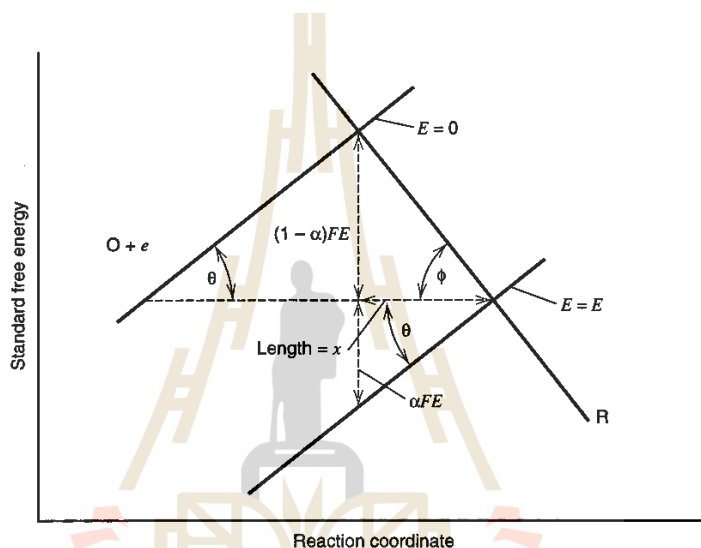


Figure 2.2 Relationship of the transfer coefficient to the angles of intersection of the free energy curves (Bard et al., 2002).

The effect of potential on the energy barrier, the height of the barriers and the configurations intersecting reactants and products at the transition state of oxidation and reduction, was considered in the reaction of Na^+ in acetonitrile or dimethylformamide. The free energy profile along the reaction coordinate was shown in **Figure 2.3** (Bard et al., 2002). When a negative potential greater than E_{eq} is applied, the barrier for reduction drops, while the barrier for oxidation rises, resulting in a net cathodic current flow. The net transformation results in the conversion of $\text{Na}^+ + e^-$ to $\text{Na}(\text{Hg})$, as shown in **Figure 2.3c** and the opposite occurs during oxidation. Thus, the potential affects the net rates and directions of electrode reactions.

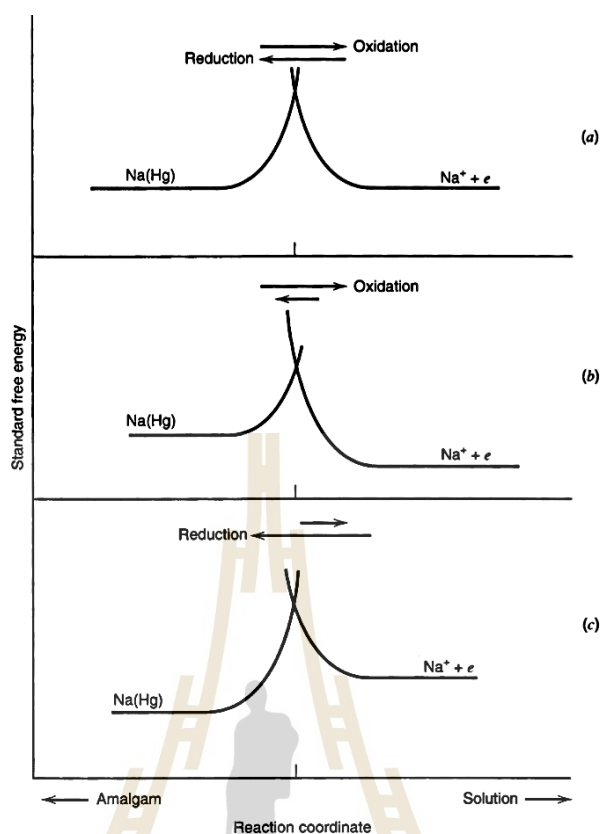


Figure 2.3 Simple representation of standard free energy changes during a faradaic process, (a) At a potential corresponding to equilibrium, (b) At a more positive potential than the equilibrium value, (c) At a more negative potential than the equilibrium value (Bard et al., 2002).

In a charge-transfer reaction at the electrode-electrolyte interface, the transfer coefficient, α , serves as an intrinsic kinetic parameter that quantifies the symmetry of the energy barrier. Typically, it is determined from the Tafel equation. Tafel analysis locates the position of the transition state relative to the oxidized and reduced products and determines the rate-determining step (RDS) for electrochemical processes (Batchelor-McAuley and Compton, 2012).

The transfer coefficient can also be described as the ratio of the reduction in the energy barrier height to the total energy applied for a particular electron-transfer reaction (Maurya et al., 2022). It elucidates how the rate of an interfacial oxidation or reduction reaction as a function of the applied potential. The transfer coefficient considers the geometry of the intersection region of the free

energy curves and is commonly interpreted qualitatively as the 'position' of the transition state. A transfer coefficient close to unity suggests that the transition state is 'reactant-like'. Conversely, a value close to zero implies a "product-like" transition state for oxidative process (Li, Lin, Batchelor-McAuley, Chen, and Compton, 2018).

Tafel analysis for a cathodic reaction:

$$\frac{\partial \ln I}{\partial E} = \frac{(n' + \alpha_{n'+1})F}{RT} \quad (2.7)$$

Tafel analysis for an anodic reaction:

$$\frac{\partial \ln I}{\partial E} = \frac{(n' + \beta_{n'+1})F}{RT} \quad (2.8)$$

Where I is the electrical current, E is the potential, F is the Faraday constant ($96,485 \text{ C mol}^{-1}$), R is the molar gas constant ($8.314 \text{ J K}^{-1} \text{ mol}^{-1}$), T is the absolute temperature (298 K), n' is the number of electron transfer before the rate determining step (RDS), $\alpha_{n'+1}$ is the cathodic transfer coefficient of the RDS and $\beta_{n'+1}$ is the anodic transfer coefficient of the RDS.

The slope of $\ln |i_{\text{red}}|$ vs. E can provide information about the magnitude of the transfer coefficient, α and β , from voltametric data (Compton and Banks, 2007) because the slope is proportional to the transfer coefficient as shown in **Figure 2.4**. In most systems, the transfer coefficient was found to be in the range of 0.3 to 0.7 (Bard and Faulkner, 1980). However, it is typically approximated as 0.5 for most electrochemical reactions ($\alpha \approx \beta \approx 0.5$) indicating that in Case 1 (see below), the first step is the rate-determining step (Compton and Banks, 2007). If a Tafel slope of 1.5 is observed, it indicates that the second electrode transfer is the rate-determining step, as shown in **Figure 2.5**.

Case 1: The first step is rate-determining:



Case 2: The second step is rate-determining:



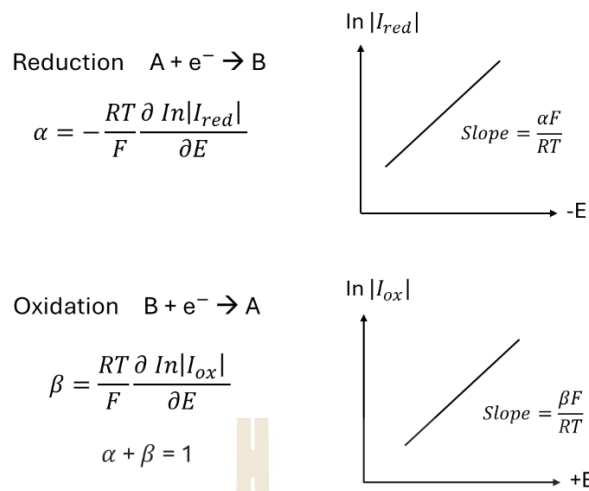


Figure 2.4 Tafel slope (Compton and Banks, 2007).

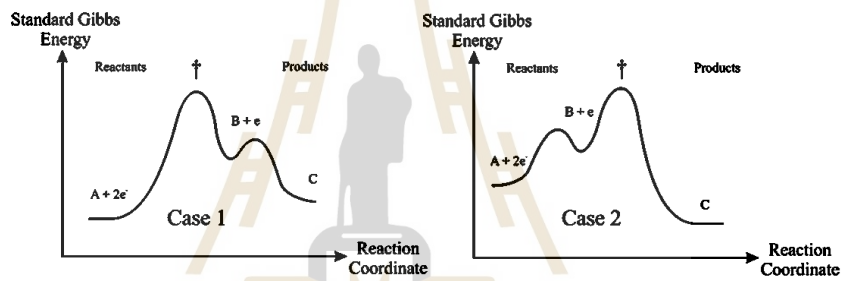


Figure 2.5 Reaction profiles for a two-electron reduction (Compton and Banks, 2007).

2.1.4 Factors affecting electrode reaction rate and current

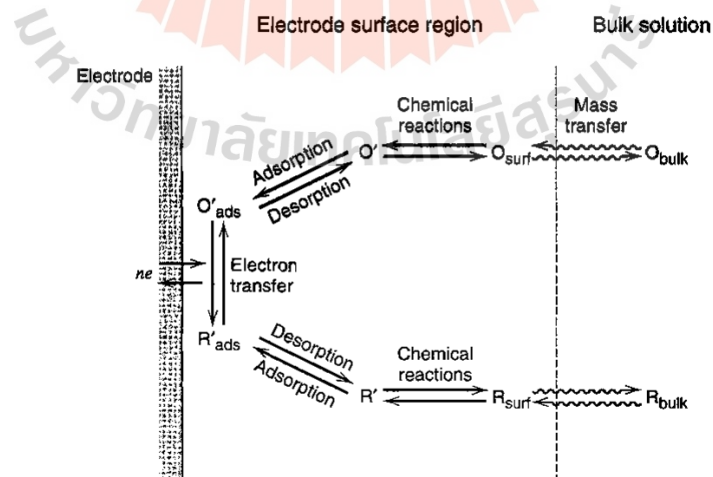


Figure 2.6 Pathway of a general electrode reaction (Bard et al., 2002).

An overall electrode reaction often involves multiple steps due to the conversion of the dissolved oxidized species, O, (species O (reduction)) to a reduced form, R (species R (oxidation).) including:

(a) Mass transfer involves the transfer of a reactant from the bulk solution to the electrode surface, followed by heterogeneous electron transfer, and finally, the mass transfer of the product back into the bulk solution.

(b) Electron transfer at the electrode surface.

(c) Chemical reactions may precede or follow the electron transfer. These reactions could be homogeneous processes (such as protonation or dimerization) or heterogeneous ones (such as catalytic decomposition) occurring on the electrode surface.

(d) Other surface reactions, such as adsorption, desorption, or crystallization (electrodeposition).

2.1.5 Mass transport

Mass transfer involves the movement of charge resulting from differences in electrical or chemical potential at two locations. Within an electrochemical system, this encompasses the transfer of charge between an electrode and a species in solution, as well as the movement of reactants in and out of the electrode interface. Mass transfer plays a crucial role in controlling the current flowing in the solution. The modes of mass transfer include diffusion, convection, and migration (Daniele and Bragato, 2014). These modes of mass transport are illustrated in **Figure 2.7** (Cai et al., 2014).

Convection refers to the action of an external force on the solution, which divides in two forms: natural convection and forced convection. Natural convection arises unpredictably due to small thermal or density gradient differences and serves to randomly mix the solution. On the other hand, forced convection involves deliberate external forces applied to the system, such as stirring, flowing, or the use of rotating electrodes. In electrochemical experiments, convection is often unwanted and can be eliminated by preventing stirring and minimizing vibration in the electrochemical cell (Cai, Zhao, Liu, Xing, and Zhang, 2014).

Migration refers to the movement of charged ions along an electric field within the electrolyte. The direction of movement is determined by both the electric field and the charge state of the particle. Migration can be effectively minimized by adding a large amount of inert supporting electrolyte at a concentration much higher than that of the electroactive species. This helps minimize the electrochemical potential gradient, allowing the system to reach equilibrium (Cai et al., 2014).

Electrochemical behavior can be manipulated to eliminate the influences of electrostatic potential and convection on the overall flux of electroactive species. The resulting currents from such experiments can then be classified only as diffusion-controlled.

Diffusion plays a crucial role in electrochemical reactions. It involves the spontaneous movement of species under the influence of a concentration gradient, moving from regions of high concentration to regions of low concentration without the effects of an electric field, with the aim of minimizing concentration differences.

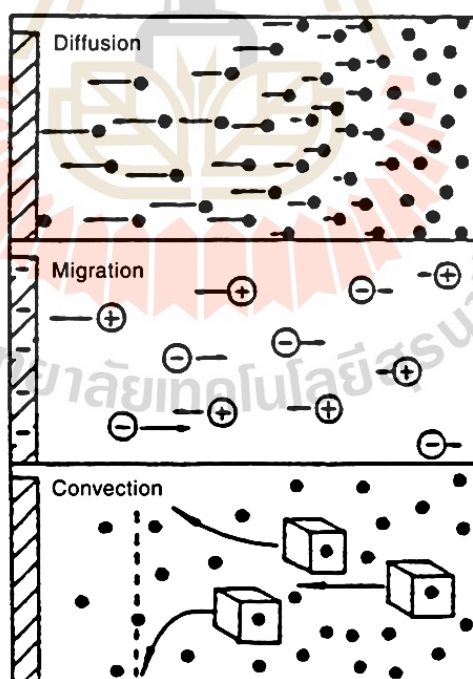


Figure 2.7 Schematics of three modes of mass transport (Cai et al., 2014).

2.1.6 Adsorption vs. diffusion-controlled process

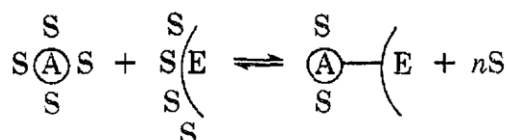
An electrochemical reaction on the surface of an electrode can occur via two limiting mechanisms: the reaction controlled by adsorption and the reaction controlled by the diffusion of electroactive species. Both mechanisms involve the movement of ions in electrolyte solutions and on the electrode surface. Solvated ions move at different velocities, influenced by their size and charge.

2.1.6.1 Adsorption-controlled process

An adsorption-controlled process involves an interaction between the adsorbate and the electrode material, leading to the formation of a layer (partial or complete) on the electrode surface. In an ideal adsorption process, a non-Faraday process is observed, indicating that there is no electron transfer at the solid-liquid interface between the electrode and the adsorbate.

Moreover, the extent of adsorption also strongly depends on the solubility of the adsorbate. The adsorption is greatly influenced by the adsorption of reactants, intermediates, or products onto the surface of the electrode, as well as by interfacial interactions between the reactants and the electrode surface. Adsorption has the potential to enhance electrode reaction rates or eliminate the electrode reaction (Anson et al., 1975; Brett and Brett, 1993). The electrode reaction depends on specific adsorption, which involves ions being adsorbed onto the electrode surface after losing their solvation, approaching closer to the electrode surface. This results in the formation of bonds with the electrode that are stronger than those with solvated ions (Brett and Brett, 1993).

Adsorption, as described by adsorption kinetics, can be studied using electrochemical methods. Electroactive species adsorbed on the electrode surface can significantly alter the voltammetric response, depending on the electrode material and solution composition. Additionally, the adsorption of non-electroactive species can inhibit the electrode reaction (Brett and Brett, 1993).



Where A is the adsorbate, S is the solvent in which the adsorption is being observed, and E is the electrode on the surface of which the adsorption occurs (Anson et al., 1975).

The adsorbate, A, loses part or all of its surrounding solvent molecules upon adsorption. The adsorbate displaces the solvent molecules that were originally adsorbed on the electrode surface, resulting in the formation of the adsorbate-electrode bond. The relationship between the amount of substance i adsorbed on the electrode per unit area corresponding to a monolayer coverage (mol cm^{-2}), Γ_i , the activity in bulk solution, a_i^b , and the electrical state of the system, E or q^M , at a given temperature, is given by the adsorption isotherm. One of the most frequency used is the Langmuir isotherm:

$$\frac{\Gamma_i}{\Gamma_s - \Gamma_i} = \beta_i a_i^b \quad (2.13)$$

Three types of isotherm are generally considered: the Langmuir isotherm assumes no interactions between the adsorbed species on the electrode surface and no surface heterogeneity, then eventually surface saturation occurs. In contrast, other isotherms, such as the Frumkin and Temkin isotherms, account for interactions between adsorbed species. This complicates the problem by making the energy of adsorption a function of surface coverage (Brett and Brett, 1993; Wang et al., 2023).

In surface-controlled processes (also known as adsorption-controlled processes), the peak current (I_p) is determined using equation 2.14 and peak currents are typically linearly proportional to the scan rate.

$$I_{p,c} = -I_{p,a} = -\frac{F^2 \nu V C_0^*}{4RT} \quad (2.14)$$

Where I_p is the peak current, C_0^* is the bulk concentration, ν is the voltage scan rate, V is equivalent to the volume of single, closely packed layer of atoms of molecules, such as a monolayer, F is the Faraday constant ($96,485 \text{ C mol}^{-1}$), R is the molar gas constant ($8.314 \text{ J K}^{-1} \text{ mol}^{-1}$), and T is the absolute temperature.

When electric charge is stored through the adsorption of ions at the electrode surface (electrical adsorption), this process includes both physical adsorption and chemical adsorption, which can be explained by the Gouy-Chapman-Stern double layer model. The applied potential and electrolyte concentration influence the double-layer capacity. This model consists of the inner Helmholtz layer (IHP), which passes through the centers of adsorbed ions, and the outer Helmholtz layer (OHP), which passes through the centers of solvated and non-specifically adsorbed ions. These two layers help explain the distribution of adsorbates within the double layer (Cheng et al., 2022). The diffuse region is outside the OHP (Brett and Brett, 1993).

More recent models of the double layer, such as the Bockris, Devanathan, and Müller model, demonstrate the role of solvent molecules near the electrode interface. This model focuses on the arrangement of solvent molecules near the interface, as well as the arrangement of layers containing specifically adsorbed ions. The IHP is the plane passing through the center of these dipoles and specifically adsorbed ions. Similarly, OHP refers to the adsorption of solvated ions, which could be identified with a second solvation layer (Brett and Brett, 1993).

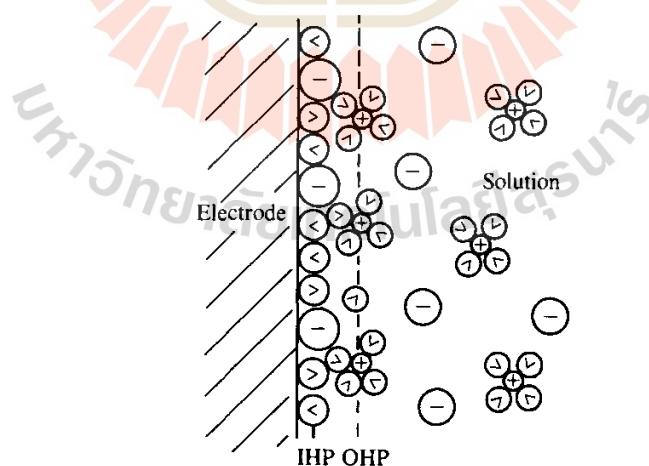


Figure 2.8 The model of Bockris et al. of the double layer, Arrangement of ions and solvent molecules; (<) represents a water molecule.

2.1.6.2 Diffusion-controlled process

Diffusion takes place across different concentrations of the electroactive species, where the concentration gradient balances with the corresponding material flux through diffusion. This occurs at various distances from the electrode-electrolyte interface. The impact of convection and migration is generally minimal compared to diffusion. The change in concentration is influenced by the geometry of the electroactive surface (Batchelor-McAuley and Compton, 2012; Brett and Brett, 1993).

The diffusion process can be described by Fick's first and Fick's second laws, which relate the flux of a substance to its concentration as a function of time and position. The flux of a substance A at a given location x and time t is governed by diffusion, moving from high to low concentration, resulting in a diffusive flux. The rate of diffusion, dependent on concentration gradients, is quantified by Fick's first law of diffusion.

$$J = -D \frac{\partial c}{\partial x} \quad (2.15)$$

Where J is the flux of A species, $\frac{\partial c}{\partial x}$ is the concentration gradient in direction x-a plane surface and D in $\text{cm}^2 \text{s}^{-1}$ is the diffusion coefficient under the defined concentration gradient. D is dependent on temperature and its value in aqueous solution normally varies between 10^{-5} and $10^{-6} \text{ cm}^2 \text{s}^{-1}$.

Fick's second law, which deals with time-dependent diffusion processes, can be derived from Fick's first law. **Figure 2.9** illustrates the flux of a substance and its concentration as functions of time and position (Compton, Laborda, and Ward, 2013). This Fick's second law is giving by:

$$\frac{\partial c}{\partial t} = D \frac{\partial^2 c}{\partial x^2} \quad (2.16)$$

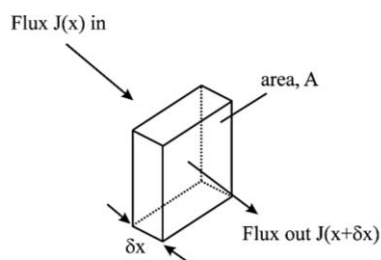


Figure 2.9 Fick's 2nd Law can be derived by considering the fluxes in and out of the 'slab'.

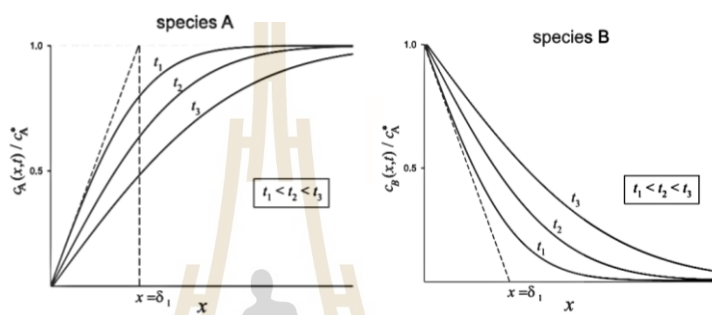


Figure 2.10 Variation with time of the concentration profiles of species A and B at a planar macroelectrode. The Nernst diffusion layer for t_1 (δ_1) is indicated on the graph. c_A^* is the bulk concentration of species A. $D_A = D_B$.

The Randles–Sevcik equation can indicate whether an analyte is freely diffusing in solution. The peak current (I_p) increases linearly with the square root of the scan rate, indicating a diffusion-controlled process. The slope of the plot from the Randles–Sevcik equation may be utilized to calculate diffusion coefficients (D), as shown in Equation 2.5.

2.1.7 The principle of electrochemical methods

The potentiostat is crucial for various electrochemical experiments, including cyclic voltammetry, chronoamperometry, and other techniques used to study redox reactions and materials in electrochemistry. It adjusts the voltage to maintain the potential difference between the working and reference electrodes and controls the voltage across the working electrode and counter electrode, as shown in Figure 2.11.

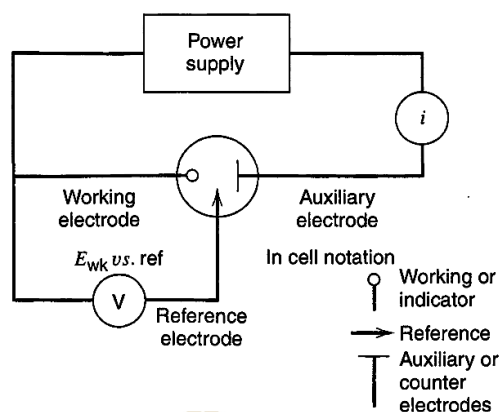


Figure 2.11 Three-electrode cell and notation for the different electrodes (Bard et al., 2002).

A common electrochemical setup, typical for experiments such as cyclic voltammetry, involves three electrodes representing the working electrode, counter electrode, and reference electrode. The conducting phase for ions is known as the electrolyte. Common electrode materials are made of a variety of substances, including solid materials like Pt and Au, liquid metals such as Hg and amalgams, carbon (graphite), and semiconductors like indium-tin oxide and Si (Bard et al., 2002). Oxidation and reduction processes take place at the electrode interface between electrodes and electrolytes, with reduction occurring at the surface that donates electrons and oxidation at the surface that accepts electrons as shown in **Figure 2.12**.

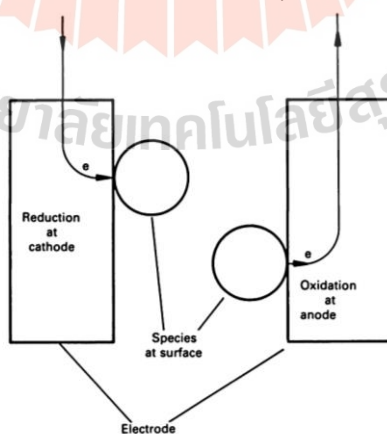


Figure 2.12 The processes of oxidation and reduction at an electrode (Hibbert et al., 1993).

2.1.8 Electrodes used in electrochemistry

All voltammetric experiments are carried out in an electrochemical cell consisting of three types of electrodes: the working electrode (WE), the reference electrode (RE), and the auxiliary electrode or counter electrode (CE).

The working electrode (WE) serves as the electrode where the electrochemical reaction takes place within the potential range of interest, controlled by the potentiostat. It is typically made of an "inert" material such as gold, platinum, or glassy carbon. The selection of electrode material is largely determined by the desired potential range for the electrode, aiming to either reduce or promote surface adsorption of the species of interest. The Working Electrode is employed for investigations of both anodic and cathodic behaviors. Any changes in the cell are attributable to the working electrode, specifically the potential of the working electrode with respect to the reference electrode. To accurately control the potential of the working electrode, it is necessary to minimize the resistance between the working and reference electrodes (Brett and Brett, 1993).

The reference electrode (RE) is defined as a stable equilibrium potential electrode, serving as a reference point against which the potential of other electrodes is measured in an electrochemical cell. Reference electrodes are used to measure and correct the electrochemical potentials generated between electrodes and electrolyte, maintaining a constant voltage referenced to the potential of the hydrogen electrode. In this work, a common reference electrode, (Ag/AgCl), consists of a silver wire covered with a solid layer of silver chloride, immersed in a saturated solution of KCl (approximately 3.5M) (Glanc, Sophocleous, Atkinson, and Garcia-Breijo, 2013; Sophocleous and Atkinson, 2017). When a current passes through this electrode, it becomes polarized, resulting in a variation in its potential. A reliable reference electrode should maintain a stable potential over time and temperatures (Glanc et al., 2013).

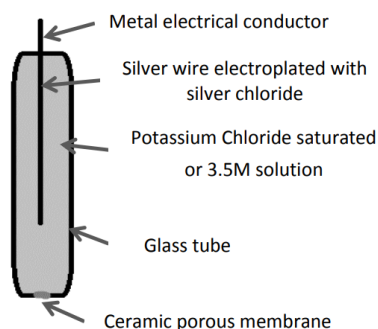


Figure 2.13 Typical construction of a silver-silver chloride reference electrode (Sophocleous and Atkinson, 2017).

The counter electrode (CE) is responsible for completing the electrical circuit and often needs to remain chemically inert to avoid interfering with the reactions happening at the working electrode. To ensure a consistent potential difference between the reference electrode (RE) and the working electrode (WE), a counter electrode such as platinum (Pt) is introduced. The current passes between the working electrode and the counter electrode, and the electrochemical properties of the counter electrode do not affect the behavior of the electrode of interest. When studying a reduction at the working electrode, an oxidation occurs at the counter electrode, as the working electrode and counter electrode have opposite reactions (Brett and Brett, 1993).

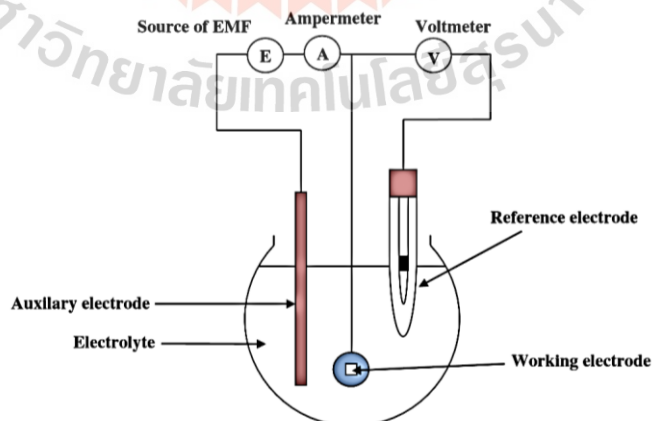


Figure 2.14 Schematic image of the conventional three electrode cells (Nasirpouri et al., 2017).

2.1.9 Supporting electrolyte

A supporting electrolyte is used to decrease the solution resistance, as electrically charged species migrate towards the electrode surface or the bulk solution to disperse the charge created by the electrode process. To reduce the migration of electroactive ions caused by the electric field, it is necessary to add a solution containing a high concentration of inert electrolyte (Compton, Laborda, and Ward, 2013).

The most frequently used electrolytes are liquid solutions containing ionic species, such as H^+ , Na^+ , Cl^- , typically in water. A suitable solvent should be able to completely dissolve the analyte and high concentrations of the supporting electrolyte, while also remaining stable toward oxidation and reduction within the potential range of the experiment. The usable potential range is controlled by solvent and/or supporting electrolyte decomposition, as well as by the electrode material, as shown in **Figure 2.15**. Typically, the supporting electrolyte should have a concentration of electroactive species at least 100 times that of the analyte, with a concentration of ≤ 5 mM or less at the macroelectrode. The concentration of the supporting electrolyte typically ranges between 0.1 M and 1.0 M. In some cases, samples for laboratory analysis already contain high concentrations of supporting electrolyte, such as seawater (0.7 M NaCl). Additionally, the supporting electrolyte should not interfere with the electrode reactions (Brett and Brett, 1993).

The concentration profile of Fc^+ (blue) and Fc (green) is defined by their concentrations relative to the distance from the surface of the electrode at various points during the voltammogram, as shown in **Figure 2.16** (Elgrishi et al., 2017). This profile is influenced by the movement of Fc^+ and Fc species between the electrode surface and the bulk solution, along with the applied potential. At the electrode surface, when a solution of Fc^+ is scanned to more negative potentials than the formal potential (E_f^0), Fc^+ is locally reduced to Fc , resulting in the measurement of a current corresponding to the reduction of Fc^+ . This point corresponds to the maximum reduction current. Then, the flux starts to decrease when the surface concentration of Fc^+ becomes near-zero. Conversely, during the reverse scan, Fc is reconverted to Fc^+ near the electrode surface as the potential becomes more positive, and it then diffuses toward the bulk solution. Although the bulk concentration of Fc is initially zero, Fc is formed from the cathodic reaction in the forward sweep. Therefore, a concentration change occurs, resulting in a characteristic "duck"-shaped response in the cyclic voltammetry at a macroelectrode (Compton and Banks, 2007).

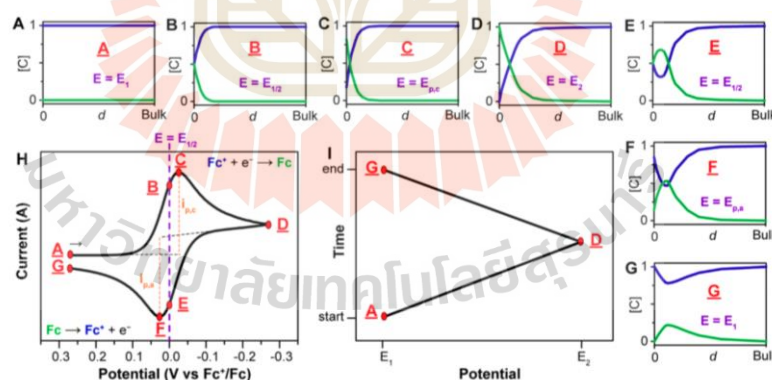


Figure 2.16 (A–G) Concentration profiles (mM) for Fc^+ (blue) and Fc (green) as a function of the distance from the electrode (d , from the electrode surface to the bulk solution, e.g. 0.5 mm) at various points during the voltammogram. (H): Voltammogram of the reversible reduction of a 1.00 mM Fc^+ solution to Fc , at a scan rate of 100 mV s^{-1} . (I): Applied potential as a function of time for a generic cyclic voltammetry experiment, with the initial, switching, and end potentials represented (A, D, and G, respectively) (Elgrishi et al., 2017).

The performance of voltammetry techniques is strongly influenced by the modified material of the working electrode and the supporting electrolyte. The working electrode should provide high signal-to-noise characteristics, as well as a reproducible response.

A macroelectrode, as a working electrode, typically has a one-dimensional (planar electrode) structure on the scale of millimeters or centimeters (Compton and Banks, 2007). The diffusion transport mainly occurs in a planar manner, perpendicular to the electrode. Electrodes with large surface areas experience significant ohmic drop and capacitive effects (Compton, Laborda, and Ward, 2013).

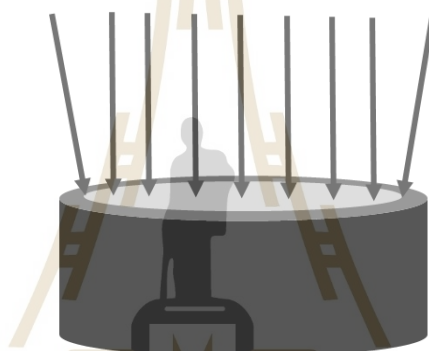


Figure 2.17 Macroelectrode (Compton and Banks, 2007).

The most popular carbon electrode material is glassy carbon, often used as a working electrode. Glassy carbon serves as an inert electrode and exhibits electron transfer kinetics dependent on its structure and surface preparation. It has become widely used due to its excellent mechanical and electrical properties. Moreover, it offers a broad potential window, low background current, high surface chemistry, low cost, chemical inertness, and suitability for various sensing and detection applications (Wang et al., 2006). It undergoes a glass-like fracture and is structurally amorphous (Uskoković et al., 2021; Wang et al., 2006). The structure of glassy carbon involves thin, tangled ribbons of crosslinked graphite-like sheets that are fully sp^2 hybridized - aromatic carbon, containing three σ and one delocalized π bond per coordination as shown in **Figure 2.18** (Wang et al., 2006). The carbon surface presents functional groups including hydrogen, hydroxyl, and carboxyl groups, and sometimes quinones. The diffusional mass transport of the macroelectrode is

primarily planar, and only the diffusion normal to the electrode width can be considered, allowing for diffusional mass transport to the macroelectrode.

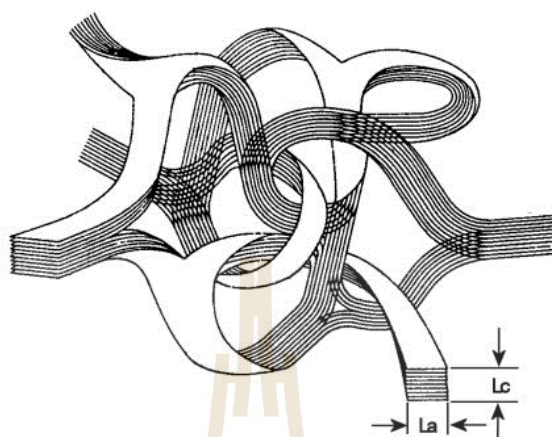


Figure 2.18 Representation of the structure of glassy carbon (Brett and Brett, 1993).

2.1.10.2 Differential pulse voltammetry (DPV)

Differential pulse voltammetry has greater sensitivity and provides signals more suitable for quantitative studies due to the elimination of the capacitive background current. The current is measured twice: once before pulse application and then at the end of the pulse, and the difference between the two currents is observed. The base potential increases in a staircase manner because it is incremented between pulses, as shown in **Figure 2.19**. Moreover, this potential steadily increases by small amounts with short pulses of increasing amplitude, with the amplitude increments always being equal. Subtracting the current of two consecutive pulses enhances sensitivity, leading to the reduction of background currents and resulting in well-defined, peaked voltammograms (Compton, Laborda, and Ward, 2013). The resulting differential pulse voltammogram directly proportional to the concentration of the corresponding analytes. Moreover, selecting the pulse amplitude and potential scan rate usually involves balancing sensitivity, resolution, and speed (Venton and DiScenza, 2020).

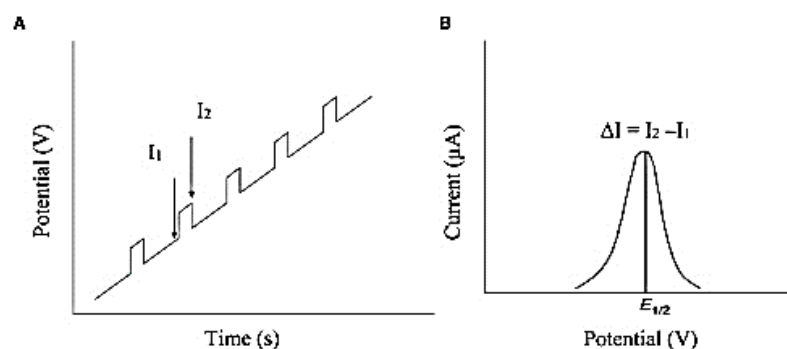


Figure 2.19 Schematic of differential pulse voltammetry (A) Staircase waveform for differential pulse voltammetry and (B) differential pulse voltammogram (Venton and DiScenza, 2020).

2.2 Uric acid, ascorbic acid and dopamine detection

Uric acid (UA), ascorbic acid (AA), and dopamine (DA) are co-present in biological fluids and play important roles in physiological processes and metabolisms.

2.2.1 Uric acid (UA)

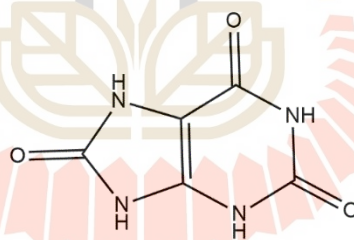


Figure 2.20 Uric acid (UA) structure.

UA is a byproduct of the metabolism of purines, which are natural substances found in the cells of the body and in certain foods. UA is typically filtered out of the blood by the kidneys and excreted in the urine. In certain conditions, UA may also function as a reactive, water-soluble antioxidant in the human body, helping to quench radicals and oxidants such as H_2O_2 or hydroxyl radical (OH^\bullet), potentially preventing aging and cancer. UA can undergo oxidation to form allantoin when reacting with reactive oxygen species (ROS) (Glantzounis, Tsimoyiannis, Kappas, and Galaris, 2005). The normal range of UA levels for healthy individuals is typically 89–357 μM for women and 149–416 μM for men (Buledi et al., 2021). The concentration

of UA in the human body varies at different levels. Both low and high levels of UA may be observed in certain health conditions. Abnormal UA levels are a major factor in several diseases, such as hyperuricemia, Lesch-Nyhan syndrome, and gout symptoms (Buledi et al., 2021). Hyperuricemia, defined as high levels of blood UA, is a major etiological factor in gout and is associated with cardiovascular and neurological diseases. The development of methods for detecting UA includes both enzyme and non-enzyme approaches, such as ultraviolet absorption and fluorescence, electrochemical methods like voltammetry and electrochemiluminescence, as well as chromatography employing both liquid and gas phases (Wang, Wen, and Kong, 2020).

2.2.2 Ascorbic acid (AA)

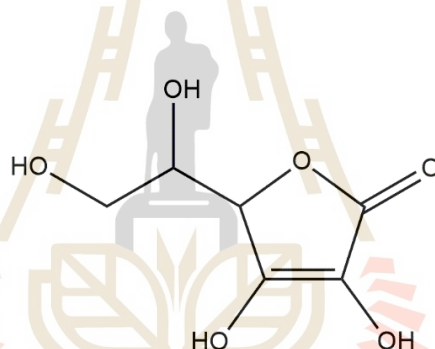


Figure 2.21 Ascorbic acid (AA) structure.

AA, a form of vitamin C found in biological systems, serves as an antioxidant and scavenging free radicals. The normal range for AA levels in the blood is typically 0.6 to 2.0 mg dL⁻¹ (Dhara and Debiprosad, 2019). Quantitative determination of AA aids in the diagnosis of certain diseases. Another drawback of AA in the human body is its potent antioxidant effect in the absence of aqueous heavy metal cations. Vitamin C deficiency can lead to various diseases, such as scurvy, rheumatoid arthritis, Parkinson's, cardiovascular disease, Alzheimer's, and cancer. Conversely, excessive intake of AA can result in various adverse effects like diarrhea, gastric irritation, and urinary stones. The detection of AA can be achieved using various analytical techniques, including chromatographic methods (such as high-performance liquid chromatography or HPLC), spectrophotometry, electrophoresis,

chemiluminescence, solid-phase iodine, fluorescence, and electrochemical techniques (Dhara and Debiprosad, 2019). However, it's important to note that AA is a common interfering substance in glucose, UA, and DA biosensors based on electrochemical analysis (Narla et al., 2016; Tukimin et al., 2018).

2.2.3 Dopamine (DA)

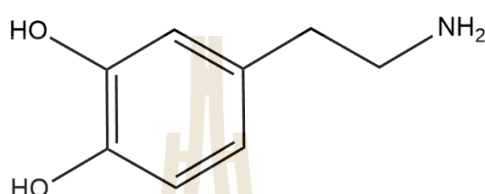


Figure 2.22 Dopamine (DA) structure.

DA is a neurotransmitter present in biological fluids that plays a crucial role in regulating emotions, maintaining hormone balance, and controlling movement in the human body. Imbalances in DA levels can lead to movement disorders and disrupt hormonal balance, potentially contributing to the development of certain diseases (Lakard, Pavel, and Lakard, 2021). Low levels of DA have an impact on the central nervous system, contributing to several neurological diseases such as increased stress, depression, Alzheimer's disease, and Parkinson's disease, which primarily affects movement. Excess levels of DA may indicate cardiotoxicity, leading to rapid heart rates, hypertension, and, in severe cases, heart failure. Normal levels of DA concentration range from 0.1 to 0.4 nM in the blood and from 0.1 to 2 μ M in urine (Mikhelson et al., 2018). High-cost analytical techniques, such as enzyme assays, liquid chromatography, mass spectrometry, capillary electrophoresis, and high-performance liquid chromatography (HPLC), are widely used for the quantitative determination of DA (Lakard et al., 2021).

2.2.4 The simultaneous determination of UA, AA and DA

Surface modification of electrodes has attracted significant interest and greatly enhances biosensor performance by covering the conductive substrate to promote electron-transfer reactions. Surface modification enhances electrocatalytic

activity, resulting in better selectivity toward the analyte (Lakard et al., 2021). Various nanomaterials have been used as electrode modifiers. This work employed two carbon-based nanomaterials, namely carbon nanotubes and microporous carbon, as well as metal oxide nanostructures like Cu_2O and CuO .

2.2.4.1 Copper (II) oxide nanomaterials

Copper (II) oxide (CuO) has been widely used as an effective electrocatalytic material for the electrochemical monitoring of UA, as demonstrated in various studies including Uricase/ CuO / Pt /galss bio-electrode (Jindal, Tomar, and Gupta, 2012) , CPE-PPy/ CuO (Sheikh-Mohseni and Pirsá, 2016) , and CuO /Glassy carbon electrode (GCE) (Buledi et al., 2021) Additionally, it has been utilized for the electrochemical monitoring of UA, AA, and DA in studies employing CuO nanoleaf-modified electrodes, Fe-doped CuO modified electrodes, and CuO nano-rice-modified electrodes.

Zheng et al. utilized a CuO nanoleaf-modified electrode for the determination of DA in the presence of AA and UA in PBS at pH 8. In the mixture of UA, AA, and DA, weak electrocatalytic oxidations of UA and AA were observed at 0.052 V and 0.372 V, respectively. They observed that upon adding DA, the oxidative peak at 0.270 V increased with the concentration of DA. At low concentrations of DA, the electrochemical response of DA was significantly higher than those of AA and UA. This suggests that CuO nanoleaf selectively absorbs DA and repels AA and UA due to electrostatic interactions and the different adsorption affinities of CuO . The concentration range of DA at the CuO nanoleaf-modified electrode shows two different ranges: 1 - 7.5 μM and 7.5 - 140 μM . The detection limit for DA was found to be 0.5 μM (Zheng et al., 2014).

Waryani et al. developed a Fe-doped CuO -modified electrode that exhibited superior catalytic activity for UA, attributed to the quantum confinement effect. The introduction of electrons to the conduction band of CuO and the reduction of the band gap by the iron dopant enhanced the conductivity of CuO , facilitating the oxidation process of UA. A highly selective oxidation peak for UA was observed at 0.41 V vs. Ag/AgCl . The sensor demonstrated a wide linear range of

0.05 - 4 mM for UA, and the detection limit was found to be 0.01 mM with acceptable recovery results (Waryani et al., 2020).

Krishnamoorthy et al. synthesized a nano-rice-like structure of CuO with high surface area, excellent conductivity, and efficient electron transfer through a simple chemical precipitation method for electrochemical sensing of DA at low concentrations. CuO demonstrated outstanding simultaneous detection for both DA and UA, with an increase in anodic peak current as the concentrations of DA and UA increased. The sensor exhibited a sensitivity and detection limit (LOD) of $432 \mu\text{A cm}^{-2} \text{mM}^{-1}$ and $0.42 \mu\text{M}$ for DA, and $73 \mu\text{A cm}^{-2} \text{mM}^{-1}$ and $1.2 \mu\text{M}$ for UA, within linear ranges of 1 – 150 μM and 1 - 160 μM for DA and UA, respectively. The amperometric response remained stable when DA and UA were interfered with by other substances. Additionally, a Nafion film was employed to mitigate interference from substances like glucose, fructose, galactose, and lactose. The determination of DA and UA in human urine showed an acceptable range of recovery. The CuO nanorice-modified electrode demonstrated minimal electrode fouling, good stability, high sensitivity, and a low detection limit (Krishnamoorthy, Sudha, Senthil Kumar, and Thangamuthu, 2018).

2.2.4.2 Copper (I) oxide nanomaterials

Copper (I) oxide (Cu_2O) was also used as an effective electrocatalytic material for the electrochemical monitoring of UA, AA and DA.

Mei et al. utilized porous Cu_2O nanospheres deposited on reduced graphene oxide (p Cu_2O NS-rGO) through a solvothermal approach. The p Cu_2O NS-rGO electrode was coated with a Nafion film for the simultaneous determination of UA and DA in the presence of a high concentration of AA. The combination of Cu_2O 's high catalytic activity and graphene's excellent electrical conductivity allowed for the individual determination of UA and DA oxidation at 0.29 V and 0.16 V, respectively, in 0.1 M PBS pH 7. The linear range and detection limit for UA were 1.0 – 138.0 μM and 112 μM , and for DA, they were 0.05 – 109.0 μM and 15 nM, respectively. The current for both UA and DA remained at 94.0 – 95.0% of the

initial value after one month, demonstrating good reproducibility and stability (Mei et al., 2016).

Yan et al. employed ferrocene (Fc) and cuprous oxide (Cu_2O) for covalent immobilization with uricase (UOx) on a glassy carbon electrode (UOx/Fc/ Cu_2O /GCE) to detect UA. The use of UOx, or urate oxidase, provided high specificity for UA, while Cu_2O , with its excellent conductivity, facilitated electron transfer. However, the introduction of BSA as a crosslinker to immobilize UOx onto the electrode surface led to a decrease in redox peaks due to hindered electron transfer of UOx and the crosslinker. This electrode demonstrated selective detection of UA over a wide linear range of 0.1 – 1,000 μM with a low detection limit (DL) of 0.0596 μM . In the presence of interference, it exhibited high selectivity for UA and a high percentage recovery value of 93.36 – 102.06 % in human urine samples (Yan et al., 2020).

Aparna et al. reported the preparation of an Au- Cu_2O /rGO nanocomposite through a one-pot synthesis method, utilizing hydrazine hydrate as the reducing agent for the selective and simultaneous determination of DA in the presence of UA. The combination of Cu_2O with high catalytic activity, Au nanoparticles, and graphene oxide (rGO) was designed to enhance sensing performance. The functional groups on rGO were expected to improve conductivity and electron transfer kinetics. Aparna observed a highly selective peak current for DA even in the presence of UA interference, with distinct peaks at 0.1 V and 0.35 V. The linear range and limit of detection (LOD) for DA were found to be 10 - 90 μM and 3.9 μM , respectively, and for UA, the corresponding values were 100 – 900 μM and 6.5 μM . Overall, the developed sensor for DA and UA detection exhibited enhanced current response, good sensitivity, and high % recovery of 95.0 – 98.6% for DA and 94.0 – 97.3% for UA (Aparna, Sivasubramanian, and Dar, 2018).

In Ning et al., Cu_2O nanoparticles were decorated on electrochemically reduced graphene oxide (ErGO) to reduce agglomeration and enhance the electrochemical performance of Cu_2O . The resulting ErGO - Cu_2O composite exhibited higher electrocatalytic activity toward UA compared to GO/GCE, attributed to the synergistic effect of ErGO and Cu_2O nanoparticles. In the presence

of interfering compounds such as AA and DA, the oxidation peaks of UA were well-separated from those of AA and DA. The modified electrode demonstrated high selectivity, sensitivity, and minimal interference. Additionally, the electrode exhibited good stability, with the peak current remaining at 92% after two weeks (Ning et al., 2018).

In a study by Ö. Doğan et al., Cu_xO/ErGO modified Au electrode (Cu_xO/ErGO/Au) was investigated for the voltammetric and amperometric detection of DA in the presence of AA. The electrodeposition of Cu_xO and ErGO was conducted using O₂ gas. The analysis confirmed the presence of two copper oxide structures, Cu₂O and CuO, through X-ray photoelectron spectroscopy (XPS). Scanning electron microscopy (SEM) images revealed a homogeneous coating of Cu₂O and CuO nanostructures on the ErGO surface. Cu_xO/ErGO/Au electrodes exhibited superior electrocatalytic performance for both AA and DA in 0.1 M phosphate-buffered saline (PBS) at pH 7.0, with peak potentials at 0.2 V and 0.6 V for AA and DA, respectively. The modified electrode demonstrated a wide linear range of 0.1–400 µM, a low detection limit of 12 nM, and a high sensitivity of 122.4 mA cm⁻² µM⁻¹ for DA (Ö. Doğan, K. Urhan, Çepni, and Eryiğit, 2019).

2.2.4.3 Carbon nanotube nanomaterials

The excellent carbon-based electrode materials, such as CNTs, exhibit outstanding electrocatalytic activity toward H₂O₂, UA, AA, and DA, owing to their high surface functionalization, electrical conductivity, and surface area (Lawal et al., 2019; Sajid et al., 2016). There are numerous examples of combining CNTs with other materials for the detection and quantification of biological compounds.

Savk et al. investigated f - multiwalled carbon nanotube (MWCNT) based ZnNi alloy (ZnNi@f-MWCNT) as distinctive materials to provide detection of UA, AA, and DA. This material exhibited the highest peak current at pH 7. The peak potentials were determined to be 0.31 V, 0.5 V, and 0.67 V in the differential pulse voltammetry (DPV) technique for AA, DA, and UA, respectively. It was observed that the oxidation peak current decreased with increasing pH. The high specific surface area of nanomaterials is a crucial factor, breaking carbon bonds on the CNT surface

to facilitate attachment to the target molecules and exhibit excellent anti-interference properties (Savk et al., 2019).

Noroozifar et al. studied the electrochemical behavior of holmium fluoride nanoparticles/multi-walled carbon nanotube in acidic conditions for UA and the coexisting interferents AA and DA. The enhancement of oxidation peak currents and a high peak separation is sufficient for determining the concentrations of the three molecules at pH 1, indicating the involvement of H^+ in the electrochemical reaction. Three well-defined peaks were observed at 0.241 V, 0.422 V, and 0.605 V in cyclic voltammetry (CV). Additionally, other interferences such as tryptophan (Trp), tyrosine (Try), cysteine (Cys), and glucose did not interfere with the determination of UA, AA, and DA (Noroozifar, Khorasani-Motlagh, Jahromi, and Rostami, 2013).

Sun et al. synthesized a core-shell structure using multiwalled carbon nanotubes (MWCNTs) and graphene oxide nanoribbons (GONRs) to modify the electrode through microwave energy for the selective detection of UA, AA, and DA. The unzipping induced by microwave heating of CNTs caused a change in the graphene sheet structures on both sides of the CNTs. At a moderate microwave power (200 W), the core-shell heterostructure was observed with a slightly dark and tube-like appearance. At the highest microwave power (250 W), TEM images showed a flat graphene structure. The core-shell GONR (200 W) electrode demonstrated selectively higher peak currents for AA, DA, and UA in CV curves compared to commonly used MWCNTs, and it exhibited good voltammetric peak separation of AA-DA and DA-UA in DPV. This is attributed to GONR (200 W) having a rapid electron transfer pathway at the inner core and active sites for selective electrochemical reactions at the outer shell. The unique electronic structure of MWCNT/GONR/GC contributes to well-separated voltammetric peaks and high peak currents, making it suitable for the detection of UA, AA, and DA (Sun, Chang et al., 2011).

W. Zhang et al. demonstrated lanthanum-multiwalled carbon nanotube electrodes (La-MWCNTs) exhibiting high catalytic activity and selectivity toward the oxidation of AA, DA, UA, and NO_2^- . The porous surface of the La-MWCNTs film facilitates electroactive species, attributed to the synergistic effect of La-O coordination bonds. In PBS at pH 6, well-separated peaks were observed at 0.08 V,

0.23 V, 0.38 V, and 0.75 V for AA, DA, UA, and NO_2^- , respectively. The obtained sensor provided a linear response range of 0.40 μM – 0.71 mM for AA, 0.04 μM – 0.89 mM for DA, 0.04 μM – 0.81 mM for UA, and 0.40 μM – 0.71 mM for NO_2^- . The corresponding detection limits were 140 nM, 13 mM, 15 nM, and 130 nM for AA, DA, UA, and NO_2^- , respectively. The recoveries of spiked samples fell within the range of 97.2% – 105.0% (W. Zhang, Yuan, Chai, Zhang, and Chen, 2012).

Yang et al. found that the selective determination of DA was achieved using a nano-sized copper oxide/multiwall carbon nanotube coated with nafion. The highest peak current was observed in the pH range of 2.0 – 9.0, showing a decrease and subsequent increase, which depends on the amount of H^+ involved in the chemical reaction. At pH 6, the surface oxidation of the electrode strongly interacted with more DA molecules due to the good electronic properties of CuO, resulting in the highest redox peak current. However, the oxidation peaks of AA and UA were relatively poor. The sensor exhibited a low detection limit of $0.4 \pm 0.03 \mu\text{M}$ and a good linear range of 1.0 – 80 μM (Yang et al., 2013).

2.2.4.4 Microporous carbon (MC)

The most utilized materials for adsorption applications involving UA (Kameda, Horikoshi, Kumagai, Saito, and Yoshioka, 2020), AA, DA (Farahi et al., 2019) and glucose (Şavk, Aydın, Cellat, and Şen, 2020) are microporous carbon materials (MC). This preference is attributed to their surface functional groups, such as $-\text{OH}$, $-\text{COOH}$, $-\text{C}=\text{O}$, and $-\text{NH}_2$ (Momtazan et al., 2018), along with their high porous structure. Additionally, MC serves as an alternative in electrochemical analysis, offering improved electrical conductivity, excellent chemical stability, and a large surface area. The attachment of MC to electrode surfaces enhances the rate of electron transfer, showcasing its high electrocatalytic capability (Farahi et al., 2019).

The adsorption of MC onto UA is attributed to various interactions, including electrostatic interactions, π - π interactions, van der Waals forces, and hydrogen bonding (Marahel, Ghaedi, and Ansari, 2015). Additionally, van der Waals forces contribute to the attraction of hydrophobic UA to the hydrophobic surface of microporous carbon. The adsorption performance of UA, AA and DA and microporous

carbon depends not only on the attractive electrostatic interaction between UA, AA, DA, and the carbon surface but also on the pH dependence (Liu et al., 2008; Marahel et al., 2015). At acidic conditions ($\text{pH} < \text{pH}_{\text{pzc}}$), the positively charged microporous carbon exhibits a strong electrostatic interaction with the UA anion. Conversely, at high pH values, this interaction leads to electrostatic repulsion between UA and the carbon surface (Liu et al., 2008).

Govindasamy and coworkers investigated the simultaneous determination of DA and UA in the presence of a high concentration of AA using a CTAB-PANI/AC modified electrode. The composites of polyaniline (PANI) and microporous carbon (MC) exhibited excellent electrocatalytic activity, conductivity, mechanical properties, and the high surface area of microporous carbon/charcoal. CTAB and potassium peroxodisulfate (PDS) were employed as a soft template for the controlled polymerization of aniline and as a radical initiator in PANI formation. In comparison with CTAB-PANI/GCE, the CTAB-PANI/AC/GCE exhibits two sharp oxidation peaks at 0.218 V and 0.335 V, along with a high peak current for DA and UA at pH 7, owing to its high electrochemical surface area. However, CTAB-PANI/GCE alone is insufficient for simultaneous determinations. Furthermore, the role of PDS leads to a more negatively charged electrode surface, which can repel negatively charged AA, thus improving the selectivity of UA and DA. Additionally, the analytical performance of the developed method is compared with other previous electrochemical sensors for AA, DA, and UA detection in **Table 2.1** (Govindasamy et al., 2016).

Table 2.1 The linear ranges, limits of detection (LOD), and sensitivities of different electrode materials employed in the electrochemical determination of AA, DA, and UA.

Ascorbic acid					Dopamine					Uric acid				
Electrode	Linear range (μM)	LOD(μM)	Sensitivity ($\mu\text{A } \mu\text{M}^{-1}$)	Reference	Electrode	Linear range (μM)	LOD(μM)	Sensitivity ($\mu\text{A } \mu\text{M}^{-1}$)	Reference	Electrode	Linear range (μM)	LOD(μM)	Sensitivity ($\mu\text{A } \mu\text{M}^{-1}$)	Reference
Graphene/Pt	0.15-34.4	0.15	0.3457	(Sun, Lee, Yang, and Wu, 2011)	Graphene/Pt	0.03-8.13	0.03	0.9695	(Sun, Lee et al., 2011)	Graphene/Pt	0.05-11.85	0.05	0.4119	(Sun, Lee et al., 2011)
Reduced graphene oxide	0.7-100	0.7	0.4342	(Wang et al., 2014)	Reduced graphene oxide	0.1-400	0.1	0.3304	(Wang et al., 2014)	Reduced graphene oxide	2-600	1	0.0153	(Wang et al., 2014)
MOF-5/3D kenaf stem-derived porous carbon ¹	0.7-11.5	0.24	0.00686	(Song et al., 2016)	Graphene coated by polydopamine/CNT ²	7-297	1	223.7	(Wang et al., 2016)	Graphene coated By polydopamine/CNT ²	20-320	15	209.6	(Wang et al., 2016)
Nitrogen doped graphene	5.0-1,300	2.2	0.09311	(Sheng et al., 2012)	Nitrogen doped graphene	0.5-170	0.25	0.2049	(Sheng et al., 2012)	Nitrogen doped graphene	0.1-20	0.045	0.1320	(Sheng et al., 2012)
Poly[N-(ferrocenyl formacyl)pyrrole]@MWCNT	200 - 400	40	0.005	(S. Zhang, Xu, Liu, Chen, and Luo, 2019)	Poly[N-(ferrocenyl formacyl)pyrrole]@MWCNT	2-16	1.1	0.020	(Zhang et al., 2019)	Poly[N-(ferrocenyl formacyl)pyrrole]@MWCNT	2-16	0.07	0.0279	(Zhang et al., 2019)

¹ The spherical porous MOF-5 microstructures supported by three-dimensional (3D) kenaf stem derived porous carbon (KSC)

² CNT = multi-walled carbon nanotube

Table 2.1 The linear ranges, limits of detection (LOD), and sensitivities of different electrode materials employed in the electrochemical determination of AA, DA, and UA (continued).

Ascorbic acid					Dopamine					Uric acid				
Electrode	Linear range (μM)	LOD (μM)	Sensitivity ($\mu\text{A } \mu\text{M}^{-1}$)	Reference	Electrode	Linear range (μM)	LOD (μM)	Sensitivity ($\mu\text{A } \mu\text{M}^{-1}$)	Reference	Electrode	Linear range (μM)	LOD (μM)	Sensitivity ($\mu\text{A } \mu\text{M}^{-1}$)	Reference
Pristine graphene	9.00-2,314	6.5	0.067	(Qi, Zhao, Tang, and Jiang, 2015)	Pristine graphene	5.0-710	2.00	0.1125	(Qi et al., 2015)	Pristine graphene	6.00-1,330	4.82	0.1029	(Qi et al., 2015)
Hierarchical nanoporous PtTi	450-1,000	17.5	27.50	(Zhao, Yu, Tian, and Xu, 2016)	Hierarchical nanoporous PtTi	25-50	2.8	21.05	(Zhao et al., 2016)	Hierarchical nanoporous PtTi	120-230	5.7	26.34	(Zhao et al., 2016)
Reduced graphene oxide/Au nanoplates	240-1,500	51	0.012	(Wang et al., 2014)	Reduced graphene oxide/Au nanoplates	6.8-41	1.4	1.8	(Wang et al., 2014)	Reduced graphene oxide/Au nanoplates	8.8-53	1.6	3.6	(Wang et al., 2014)

2.2.5 The evaluation of the peroxide scavenging activity of UA

UA exhibits the ability to protect cells from damage by acting as an antioxidant and free radical scavenger. This protective function involves the inactivation of various reactive oxygen species, including peroxy and hydroxyl radicals, which are known to be induced by free radical-induced oxidative stress (Guelcin et al., 2008; Nimse and Pal, 2015). Peroxyl radicals, under physiological conditions, have the capability to extract an electron or hydrogen atom from the base pairs of DNA, leading to oxidative damage. UA is harnessed for its potent scavenging ability against carbon-centered radicals and peroxy radicals (Nimse and Pal, 2015).

In addition, the monitoring of antioxidant activity (AOA) has been determined using electrochemical methods (Brainina and Kazakov, 2020). In another method, Guelcin reported the radical scavenging activity of UA through spectrophotometric measurements. UA was reacted with H_2O_2 in phosphate buffer (pH 7.4), and the absorbance was recorded at 230 nm. The percentage of peroxide scavenging activity of UA at a concentration of 10 $\mu\text{g/ml}$ was estimated to be 41.1% (Guelcin et al., 2008).

2.3 Oxygen detection

2.3.1 O_2 solubility in electrolyte and sea water

The amount of dissolved oxygen (DO) in water is one of the most important indicators of water quality. Even relatively small amounts of dissolved O_2 in both fresh and seawater are sufficient to sustain marine and aquatic life and facilitate the decomposition of organic waste in water bodies. The exchange of oxygen between the atmosphere and seawater occurs at the ocean's surface, where oxygen levels are replenished through the diffusion of O_2 from the atmosphere. Furthermore, aeration, driven by winds, allows oxygen to dissolve in the water as a byproduct of photosynthesis by aquatic plants (Waddell, Darby, Theobald, and Management, 1985).

Oxygen has limited solubility in water, a property directly influenced by atmospheric pressure (increasing at higher pressure) and inversely related to water temperature (decreasing at higher temperatures) and salinity (decreasing with higher concentrations of electrolytes). This work will provide a detailed discussion of the impact of salinity on the solubility of oxygen. As salinity increases, the amount of oxygen that water can hold decreases—a phenomenon known as the "Salting-out effect." This effect occurs because the presence of dissolved salts, such as sodium chloride (NaCl), in water can affect the solubility of oxygen, reducing the weak affinity of non-polar oxygen molecules for water. Therefore, high salt levels lead to low O₂ solubility in the water (Buvik et al., 2021; Zannotti and Giovannetti, 2015).

Freshwater typically has a salinity of 0.5 ppt or less in rivers. Salinity levels increase as you move from estuaries to the ocean and are categorized as oligohaline (0.5-5.0 ppt), mesohaline (5.0-18.0 ppt), or polyhaline (18.0-30.0 ppt). The salinity levels in the ocean are typically more than 30.0 ppt. Salinity is usually expressed in units of parts per thousand (ppt) or ‰ (Alves et al., 2009). The amount of inorganic substance with predominant cation and predominant anion in seawater as listed in **Table 2.2**.

Table 2.2 Main constituents of seawater corresponding to a salinity of 35‰.

Predominant cations	g/kg	mM	Predominant anions	g/kg	mM
Sodium	10.77	479	Chloride	19.37	559
Magnesium	1.30	54.4	Sulfate	2.71	28.9
Calcium	0.409	10.5	Carbonate	0.023	2.33
Potassium	0.388	10.4	Bromide	0.065	0.86
Strontium	0.010	0.09	Fluoride	0.001	0.075

Salinity is commonly determined by measuring the chloride content since chloride is a major component of the various dissolved salts and ions in seawater. The level of dissolved oxygen in water is influenced by the salinity of seawater, with the solubility of dissolved oxygen decreasing as salinity increases. The average salinity

in the open ocean is approximatedly 35 parts per thousand (‰). Chloride content is often described by the following equation, where Cl^- [‰] represents chlorinity expressed in parts per thousand (Huber et al., 2000).

$$S [\text{‰}] = 0.03 + 1.805 \text{Cl}^- [\text{‰}] \quad (2.18)$$

A study investigated the influence of hydration on the solubility of O_2 in seawater, revealing that the solubility of O_2 is contingent on changes in the structure of electrolyte solutions. Ordinarily, oxygen molecules penetrate the tetrahedral ('ice-like') formation voids in the network of H-bonded water molecules, causing alterations in the structure of the solutions. The number of voids in tetrahedral formations decreases with increasing salt concentration, temperature, and pressure. Moreover, researchers have observed the mechanism by which O_2 is inserted into voids within ice-like water structures, particularly in the presence of ions with positive and negative hydration. These ions can disturb the network of hydrogen bonds within the water structure, causing O_2 molecules to fill the voids between hydrogen-bonded water molecules rather than replacing water molecules in the network of the tetrahedral formations. As the concentration, temperature, and pressure increase, the number of voids in the tetrahedral formations decreases, leading to a decrease in the solubility of O_2 . The presence of ions with negative hydration significantly influences the conditions under which O_2 can penetrate the structure (Mel'nichenko et al., 2008).

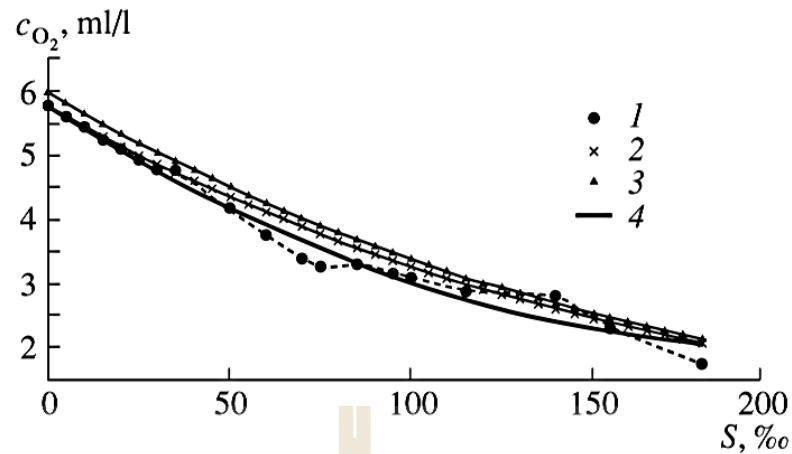


Figure 2.23 Dependences of the concentration of oxygen in sea water on its salinity at 25 °C from similar dependences of taken from various sources with extrapolation to higher salinity values (Mel'nichenko et al., 2008).

To understand the influence of salts on water oxygenation, Zannotti studied the effect of cations on water oxygenation using three types of chloride salts: LiCl, NaCl, and KCl. The charge and radius properties of alkali metals, along with thermodynamic parameters in aqueous solutions, were used to appropriately understand the oxygen mass transfer phenomena in salt solutions. This work focused on the hydrogen bond interaction of bulk water in the presence of salts with different cations (Li⁺, Na⁺ and K⁺) with making or breaking properties. The presence of these cations facilitates the transfer of oxygen molecules to bulk water in the following order: KCl > NaCl > LiCl. The lower charge and larger radius properties of K⁺ make it more influential as a "breaking" ion in the hydrogen bond network of water compared to Li⁺ and Na⁺, leading to higher entropy values. K⁺ ions, with their lower charge density, face challenges in rebuilding a well-structured water network around themselves when interacting with water, thereby promoting the removal of oxygen molecules from the network (Zannotti and Giovannetti, 2015). Moreover, the same mobilities of K⁺ and Cl⁻ ions were used to avoid any contribution of liquid junction potentials to the cell potential (Brett and Brett, 1993).

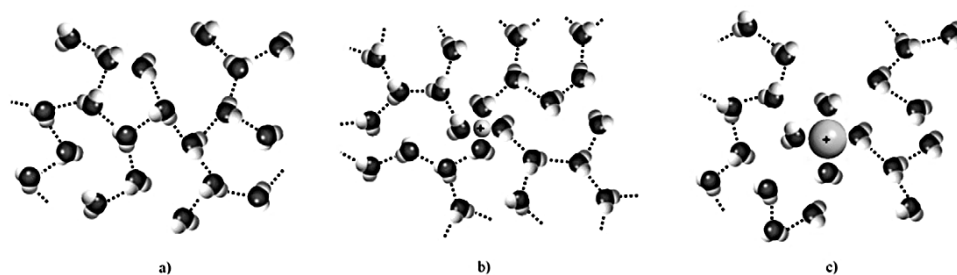


Figure 2.24 Schematic representation of hydrogen bond network of water, (a) bulk water structure; (b) water structure in the presence of making ion; (c) water structure in the presence of breaking ion (Zannotti and Giovannetti, 2015).

Table 2.3 Charge and radius properties of alkali metals in aqueous solution.

	Li ⁺	Na ⁺	K ⁺
Ionic radius (pm)	60	95	133
Charge density (C pm ⁻¹)	0.0167	0.0105	0.0075
Hydrated radius (pm)	340	276	232
Hydrated number	23.3	16.6	10.5

Table 2.4 Alkali metal chlorides hydration entropy.

Salt	Hydration energy ($\Delta_s S$) (L mol ⁻¹ K ⁻¹)
LiCl	-147.7
NaCl	-117.4
KCl	-79.9

2.3.2 Transition metal porphyrin complex

The unique structure of the Fe-N-C catalyst has widespread attention for its application in the oxygen reduction reaction (ORR). The Fe-N-C catalyst consists of Fe active sites coordinated by pyridine/pyrrole nitrogen and carbon, facilitating the reduction of O₂. The various coordinated structures of the Fe-N-C catalyst, including the increase in intrinsic activity and the number of active sites, result in varied ORR activities, as shown in **Figure 2.25** (Shen et al., 2019).

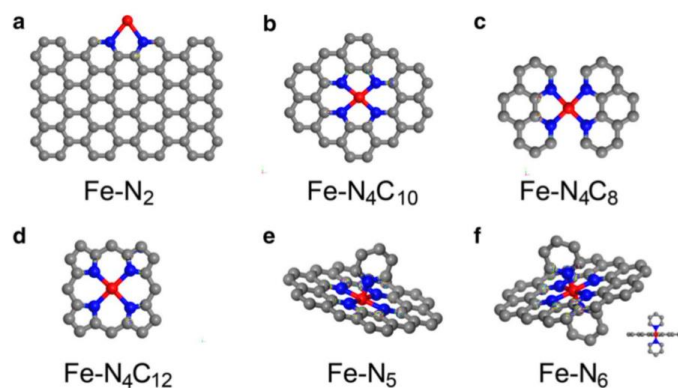


Figure 2.25 Different coordination of the Fe-N-C structure on graphene as a supporting material. Gray ball: carbon; Red ball: iron; Blue ball: nitrogen (Shen et al., 2019).

Hemin, a Fe-N₄-C structure, is a coordination complex of iron (Fe³⁺) and protoporphyrin IX. It serves as an electroactive material with an Fe core (Fe³⁺/ Fe²⁺ redox couple), allowing for direct electrochemical redox activity. Furthermore, it is capable of facilitating direct electron transfer to and from biomolecules, making it an excellent bioactive material widely employed in biosensors. Hemin has demonstrated high electrocatalytic activity in the reduction of dioxygen, hydrogen peroxide, uranium, tryptophan, and nitrite (Gao and Chen, 2005).

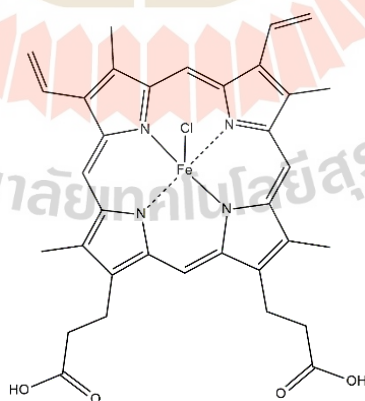


Figure 2.26 Hemin (Chloroporphyrin IX iron(III)).

The oxygen reduction reaction (ORR) takes place at the cathode, where O₂ molecules undergo reduction through the gain of electrons. The reactivity of iron (Fe) in the ORR is intricately linked to the energy changes associated with the

geometry of the ligand-metal atom bonds. The coordination environment of the Fe active sites, particularly the nature of ligands such as pyridine and pyrrole nitrogen, plays a crucial role in influencing the overall efficiency of the ORR process (Harada et al., 2009).

Iron porphyrin can form various structures, including monomers, π - π dimers, μ -oxo dimers, and π -stacked aggregates of μ -oxo dimers. The formation of these structures depends on factors such as concentration, pH, the presence of salts, temperature, and the type of solvent (Villiers, Kaschula, Egan, and Marques, 2007). Porphyrin was found to maintain its monomeric form in methanol and dimethyl sulfoxide (DMSO) and exist in a dimeric form in a range of aprotic solvents (such as DMSO, acetone, DMF, THF, and 2,6-lutidine). The π - π dimer can exist as a mixture with the monomer in solvents like methanol, ethanol, propanol, ethylene glycol, diethylene glycol, and formamide, depending on solvent polarity. In water/alcohol mixtures, both the monomer and π - π dimer are present (de Villiers, Kaschula, Egan, and Marques, 2007).

The most often investigated iron porphyrins structure are μ -oxo-bridged dimers (Dziedzic-Kocurek et al., 2009). Dimerization leads to alterations in the local electronic structure at the iron center, accompanied by changes in solvent interactions and axial coordination (Alsharabasy et al., 2021). The formation of dimeric structures influences both the dynamic and structural properties of iron porphyrin molecules, as well as their functions. One characteristic spectral feature of hemin is the broad Soret band, which includes intense π - π absorption bands from the porphyrin ring, often referred to as Q- or B-(Soret) bands (Harada et al., 2009). The dimerization of iron porphyrin to form a μ -oxo dimer (with the presence of the Fe-O-Fe bond) under alkaline conditions was achieved by introducing 1.0 M NaOH (de Villiers et al., 2007).

In aqueous solution, iron porphyrin does not form a μ -oxo dimer. Instead, it has been proposed that the dimer is a π - π dimer of two five-coordinate iron porphyrins with H₂O/HO as axial ligands. However, in high salt concentrations, large π -stacked aggregates of μ -oxo dimers of iron porphyrin are formed. The UV-vis spectrum exhibits a broader Soret band compared to mixed aqueous solutions, suggesting the

presence of both the π - π dimer and a charge transfer region characteristic of the μ -oxo dimer (de Villiers et al., 2007).

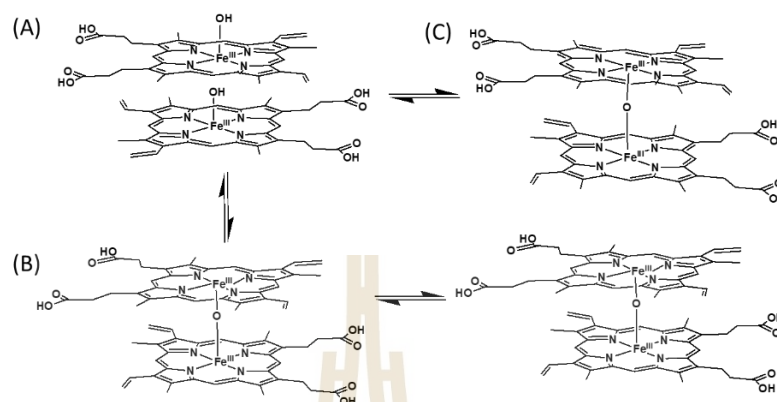


Figure 2.27 Molecular structure of the iron porphyrin monomer (A), iron porphyrin dimer (B) and iron porphyrin in high salt concentration (de Villiers et al., 2007).

2.3.3 Oxygen reduction reaction (ORR) on transition metal porphyrin complex

Transition metal macrocyclic complexes can catalyze the oxygen reduction reaction (ORR) through either a two-electron transfer pathway to produce H_2O_2 or a four-electron transfer pathway to produce H_2O . Alternatively, they can catalyze the ORR through a mixed pathway involving both two- and four-electron transfer reductions. Commonly employed techniques for studying ORR catalysis include steady-state polarization, cyclic voltammetry (CV), and rotating disk electrode (RDE), as well as rotating ring disk electrode (RRDE) (Si et al., 2014).

The catalytic activity of transition metal macrocyclic compounds in the oxygen reduction reaction (ORR) is influenced by multiple factors, including the transition metal center, the chelating ligand, and the size of the π -electron system. Transition metal macrocyclic complexes include a range of metal centers, such as Fe, Co, Ni, and Cu, and macrocyclic ligands that include chelating atoms like N_4 , N_2O_2 , N_4S_4 , O_4 , and S_4 . Among these, Fe metal centers and N_4 chelating atoms, which exhibit the highest impact on the activity sequence of Fe complexes, have the greatest potential to influence ORR activity. In most cases, Fe- N_4 can catalyze 4-electron oxygen reduction and the product is water (Si et al., 2014).

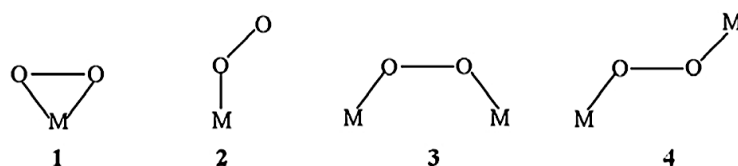


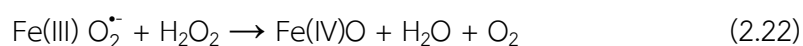
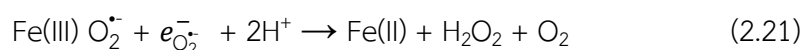
Figure 2.28 Possible configurations of dioxygen interaction with a metal in a complex (Si et al., 2014).

In 2:1 complexes of metal-dioxygen ($M-O-O$), specifically in case 2, bonding originates from the interaction between the d-orbitals on the metal and the combination of π^* and π orbitals on O_2 . The singlet or triplet nature of dioxygen orbitals determines whether the interaction occurs in a bridge- or trans-mode with the metal. The product of O_2 reduction depends on the mode of adsorption of the oxygen molecule on the metal surface, leading to different mechanistic steps (Si et al., 2014).

A bridge configuration is likely to occur on noble metals such as Pt, involving face-to-face porphyrins, which results in the reduction of O_2 to water with little or no peroxide formed. A trans configuration is likely to occur on metal porphyrins, metal phthalocyanines, and dimeric metal complexes. The conformation of two porphyrin rings in a dimer typically remains in a parallel configuration. This arrangement allows two metal atoms to bind and reduce a dioxygen molecule in the gap between the porphyrin rings (Collman, Elliott, Halbert, and Tovrog 1977).

The entire reaction of O_2 reduction by metal porphyrins consists of multiple elementary steps, including electron transfer and chemical reactions involves specific intermediates through a redox catalysis procedure, which depends on the nature of the electrode material, catalyst, and electrolyte. Firstly, superoxide ions $O_2^{\bullet-}$ are produced on a glassy carbon electrode (GCE). Superoxide ions, important intermediates for a fundamental understanding of the ORR mechanism, form adducts at the metal center, followed by an intra-adduct electron transfer from the metal ion to the oxygen. In O_2 reduction, the O-O bond distance between O_2 and the metal atom increases (Si et al., 2014). The addition of protons from the electrolyte, coupled with electron transfer, results in the production of H_2O_2 , which can be subsequently

reduced to form water. The mechanism can be summarized as follows: (Le and Jeong, 2018; Sokolov et al., 2017)



In collman et al., the two porphyrin rings are arranged in a 'face-to-face' configuration in a parallel conformation. Dioxygen binds and undergoes reduction in the gap between the two metal atoms within the porphyrin rings, forming species V. Subsequently, species V transitions to the bis-ferryl complex VI through a $4e^-$ reduction process. Protonation of the bis-ferryl complex VI, followed by the reduction of iron by an electrode surface, could lead to the overall catalytic reduction of O_2 to H_2O as shown in **Figure 2.29** and **Figure 2.30** (Collman et al., 1977)

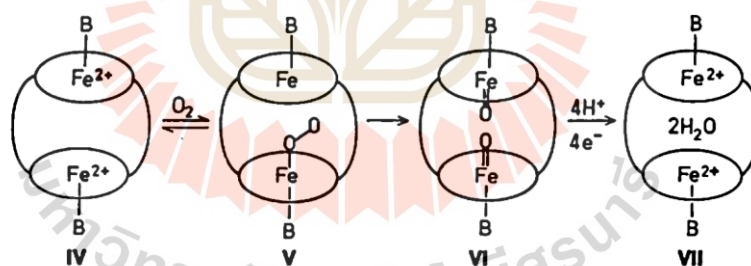


Figure 2.29 Proposed reaction of O_2 with a "face-to-face" binary Fe^{2+} porphyrin. B is an axial base too large to fit in the cavity. Ovals represent porphyrin rings (Collman, 1977).

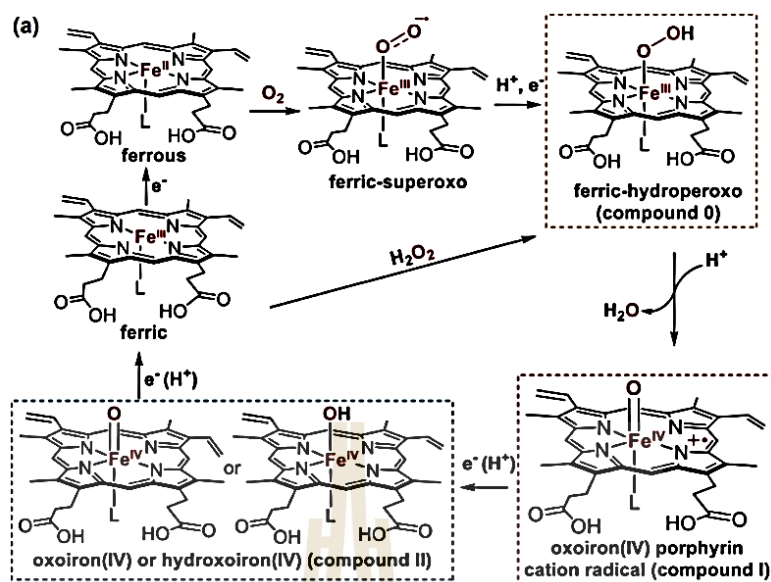


Figure 2.30 Interaction of O_2 with heme and heme – O_2 intermediates in heme proteins (Huang and Groves, 2018).

2.3.4 Literature review of oxygen reduction reaction (ORR) on transition metal porphyrin complex

The study conducted by Fu et al. involved a comparison of the O_2 reduction on bare, reduced graphene oxide (RGO), and reduced graphene oxide–silver nanoparticles (RGO/Ag) composite-modified glassy carbon electrodes (GCE). RGO served as an excellent electron transfer mediator, and the supporting materials for Ag nanoparticles enhanced the electrocatalytic performance of noble metal nanoparticles. Silver nanoparticles, known for their high catalytic activity for O_2 , effectively prevented the stacking of RGO sheets. The large peak current the RGO/Ag electrode was observed at -0.26 V indicated effective catalysis for the electrochemical reduction of O_2 , signifying a fast and efficient four-electron reaction for dioxygen reduction. The linear range was observed from 1 to 120 μM , with sensitivity and detection limits of 0.205 $\mu A \mu M^{-1}$ and 0.031 μM , respectively (Fu, Zheng, Fu, Wang, and Cai, 2015).

Carbon felt (CF), a micro-electrode ensemble of microcarbon fibers, physically adsorbs hemin through hydrophobic and π - π stacking interactions between hemin and the graphite basal plane of CF. This sensor functions as an electrochemical sensor for the reduction of DO. Hemin-CF exhibited a pair of reversible peaks located

at -0.342 and -0.307 V, assigned to the hemin – Fe (III) / Fe(II) redox process, whereas bare-CF did not show any redox wave at this potential region. Hemin-CF displayed a large cathodic current at -0.2 V in 0.1 M BR buffer (pH 7.0) with varying concentrations of DO, suggesting excellent electrocatalytic activity for the electrochemical reduction of DO. The developed hemin-CF sensor demonstrated high reproducibility, could tolerate high concentrations of interfering species, and accurately measured O_2 levels in pond, stream, and tap waters, consistent with a DO meter (Wang et al., 2013).

High-performance electrochemical sensors for O_2 and H_2O_2 were investigated using the CCG–hemin composite, prepared by simply mixing aqueous solutions of chemically converted graphene (CCG) and hemin through π – π interactions. Upon the addition of CCG, the dispersion of the CCG–hemin solution showed a significant redshift, indicating the formation of stable complexes via π – π stacking interactions between hemin molecules and CCG sheets. In electrochemical studies in a blank electrolyte solution, CCG sheets proved to be an excellent substrate for immobilizing and stabilizing hemin molecules after cycling for 100 CV cycles. In an O_2 -saturated H_2SO_4 solution, the cyclic voltammograms (CVs) of hemin and the CCG–hemin electrode exhibited strong oxygen reduction reaction (ORR) waves at 0.09 V and -0.07 V, respectively. The potential for ORR at CCG–hemin was found to be approximately 0.16 V higher than that at the hemin electrode. Consequently, CCG–hemin exhibited significantly greater electrocatalytic activity for ORR than hemin (Chen, Zhao, Bai, and Shi, 2011).

In this work, a conventional electrochemical DO sensor was developed through the co-electropolymerization of polyhemin with polypyrrole and silver, wherein silver enhances electron transfer. Furthermore, the sensor was coated with a silicone rubber [poly(dimethylsiloxane) (PDMS)] grafted with polyethylene glycol (PEG) to serve as an anti-biofouling, gas-permeable membrane, thereby enhancing the selectivity of the DO sensor. A sensitivity of 20.7 ($\mu A\ cm^{-2}$) ($mg\ L^{-1}$) $^{-1}$ was observed over a DO concentration range of 7 – 2 $mg\ L^{-1}$. The linear range for DO covers the entire spectrum of water monitoring, from 7 to 4 $mg\ L^{-1}$. In natural water, common interferences such as 0.1 M phosphate and nitrate can change the response current, resulting in a shift of approximately 30–50% during DO sensing. Furthermore, the use

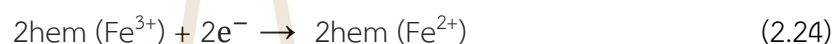
of PEG in the PEG-PDMS membranes can protect the sensor from biofouling, such as proteins on the PDMS surface (Hsu and Selvaganapathy, 2013).

Hemin was immobilized on the surface of carbon nanotubes through non-covalent (π - π interaction) bonding to be used as an O_2 sensor in a pH 7.4 PBS buffer. The modification of hemin on carbon nanotubes enables it to catalyze the reduction of hydrogen peroxide and oxygen, demonstrating the outstanding electrocatalytic properties of hemin. The electrocatalysis of O_2 reduction on the hemin-modified MWNT electrode was evidenced by an increase in peak current, more than four times greater than the response observed on the GCE and the MWNT electrode without hemin immobilization, and a positive shift in potential at -87, -182, and -290 mV. These observations suggest that hemin adsorbs onto the surface of the nanotubes (Ye et al., 2004).

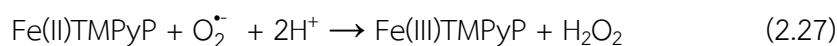
The integration of an electropolymerized polyhemin electrode, a Pd/H reference electrode, and a stainless-steel rod was utilized to create a solid-state DO sensing device, which was subsequently applied to water samples. In contrast to conventional reference electrodes (RE), this work employed semi-solid-state electrolytes to enhance performance. The performance of the Pd/H reference electrode depends on the pH of the sample solution, eliminating the need for internal liquid electrolytes. To prevent interference from wastewater, a poly(dimethylsiloxane) membrane (PDMS membrane) was spin-coated onto the polyhemin DO-sensitive electrode on an ITO substrate. An oxygen reduction reaction (ORR) peak was observed at -1.15 V in the cyclic voltammetry (CV) curve. This DO sensing device demonstrated a sensitivity of $1.3 (\mu\text{A cm}^{-2}) (\text{mg L}^{-1})^{-1}$ and a detection limit of 0.26 mg L^{-1} over a DO concentration range of 1.5 to 20 mg L^{-1} . It exhibited long-term durability, operating successfully over 60 cycles in both surface water and wastewater. The Pd/H reference electrode is well-suited for a narrow pH range, making it suitable for applications in drinking water (Hsu, Deen, and Selvaganapathy, 2017).

Hemin, naturally adsorbed on the GC, showed a small contribution to the catalytic reduction of dioxygen at -0.85 V. Li et al., found that the catalytic current of dioxygen at the hemin-coated GC electrode exhibited an enhanced catalytic current

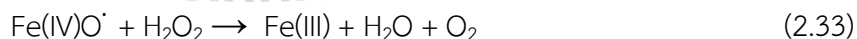
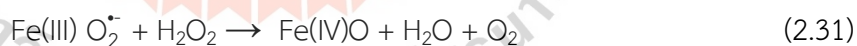
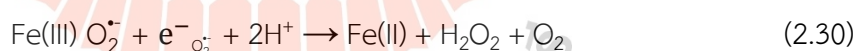
at -0.30 V vs. Ag/AgCl during air bubbling. This result supports the electrocatalysis of dioxygen by hemin. The catalytic current for the reduction of O₂ is controlled by the diffusion of dioxygen. However, this adduct has not been recognized in electrochemically catalytic experiments. In O₂ reduction, Ferrous hemin is converted to another species, specifically the dioxygen adduct [hem(Fe²⁺)-O₂], rather than the ferric state (Fe³⁺), as confirmed by UV-vis spectra. The formation of a dioxygen adduct involves two ferrous hemin molecules and one dioxygen molecule. The calculated number of electrons, which is 2, indicates that the quantity of hemin molecules is higher than the number of dioxygen molecules (Li, Aoki, Chen, and Nishiumi, 2015).



The electrocatalytic reduction of O₂ occurs through an EC catalytic regeneration mechanism. The water-soluble Fe(III) tetra(N-methylpyridyl)-porphyrin cation, abbreviated as Fe(III)TMPyP, can undergo a homogeneous reaction with dissolved oxygen. When oxygen is reduced by one electron, it forms superoxide at the electrode surface. Available superoxides (O₂^{•-}) covalently bond with Fe³⁺ porphyrin (Fe(III)TMPyP) to form an intermediate, which can be produced by either Fe(III)TMPyP and O₂^{•-} or Fe(II)TMPyP + O₂. The rapid addition of protons, followed by the addition of another electron from either the electrode, would result in the production of hydrogen peroxide. This reaction is reversible and involves binding with superoxide, implicating it in the EC mechanism, which leads back to the formation of Fe(III)TMPyP (Bettelheim and Kuwana, 2002; Pasternack and Halliwell, 2002).



This work, (Sokolov, Sepunaru, and Compton, 2017), the reaction mechanism of the electrochemical oxygen reduction reaction (ORR) was observed using hemoglobin (Hb) immobilized within a Nafion-modified electrode. Hemoglobin can interact with oxygen and serves as a suitable candidate catalyst for ORR because the oxy-hemoglobin complex, in the Fe (III) oxidation state, is known to combine with a dioxygen radical via covalent bonding. The modified electrode, denoted as Nafion–Hb–Nafion, was prepared by sequentially drop-casting Nafion layers and hemoglobin layers. In an O₂-saturated solution, a large oxygen reduction peak can be observed at -0.51 V, attributed to the iron active site, which plays a key role in the catalytic response. To determine the electron transfer process, the transfer coefficient (α) of the Nafion–Hb–Nafion modified electrode is 0.57 ± 0.07 . This value, being less than 1, indicates that the initial electron transfer is rate-determining. In the oxygen reduction reaction (ORR) mechanism of the Nafion–Hb–Nafion electrode, oxygen is first reduced at the electrode surface by generating superoxide. This superoxide then binds with hemoglobin Fe(III) adjacent to the electrode. Fe(III) accepts a second electron from the superoxide species, leading to the formation of hydrogen peroxide (Sokolov et al., 2017).



The analytical performance of the developed method is compared with other previous electrochemical sensors for dioxygen detection in **Table 2.5**.

Table 2.5 Comparison of the analytical performances of electrochemical DO sensors.

Electrodes	Catalyst/redox mediator	Electrode modification	Method	DO linear range (μM)	Sensitivity ($\mu\text{A } \mu\text{M}^{-1}$)	LOD (μM)	References
1. ITS/PLL-GA/GCE	Indigotetrasulfonate (ITS) (deposit)	Electrodeposition	RDE	0 - 178.4	0.906	2.2	(Tsai, Wang, and Chen, 2011)
2. SiO ₂ /SnO ₂ /MnPc/RDE	Mn (II) Phthalocyanine (deposit)	Covalent bonding with SiO ₂ /SnO ₂ / MnPc	DPV	-	0.147	0.0007	(Santos, Landers, and Gushikem, 2011)
3. NiCo ₂ O ₄ /rGO/[BMIM][PF ₆]/GCE	NiCo ₂ O ₄ (deposit)	Covalent bonding with ionic liquid (IL) by combining NiCo ₂ O ₄ /rGO	CV	-	0.3485	-	(Yu et al., 2020)
4. Nano-Cu/glassy carbon disk electrode (GCE)	Copper nanoparticle (nano-Cu) (deposit)	Electrodeposition	AMP	1.4973 - 18.7163	-	0.1123	(J. Yang, Chen, Zhou, and Wu, 2011)
5. ITO-IrOx/RDE	ITO-IrOx (deposit)	Covalent bonding with ITO-IrOx	LSV	0.0125 - 0.3650	-	0.0153	(Siddika, Hasan, Oyshi, and Hasnat, 2023)
6. rGO/Ag/GCE electrodes	Reduced graphene oxide (RGO) (deposit)	Galvanic displacement method	AMP	-	0.205	0.03	(Fu et al., 2015)
7. PtNPs/copper-core microelectrode	Platinum nanoparticles (deposit)	Covalent bonding with copper-core electrode	CV	10.0 - 195.0	0.0090	-	(Fang et al., 2015)

Table 2.5 Comparison of the analytical performances of electrochemical DO sensors (continued).

Electrodes	Catalyst/redox mediator	Electrode modification	Method	DO linear range (μM)	Sensitivity ($\mu\text{A } \mu\text{M}^{-1}$)	LOD (μM)	References
8.GCE	Ag nanodendrites (deposit)	Electrodeposition	AMP	1.0 - 66.7	0.169	0.043	(D. Zhang, Fang, Miao, Ma, and Chen, 2013)
9. Fe_3O_4 @ α - SiO_2 @hemin/ p-GCE	Hemin and Fe_3O_4 (deposit)	Covalent hemin binding to the Fe_3O_4 @ α - SiO_2 particles	CV	160.0 - 1,1000.0	0.0106	5.32	(Feng, Li, Li, Wang, and Zhang, 2011)

Abbreviations:

[BMIM][PF₆]: ionic liquid 1-butyl-3-methylimidazolium hexafluorophosphate, Ag: silver nanoparticles, Fe₃O₄: iron oxide, IrOx: iridium-based nanoparticles, ITO: indium tin oxide, ITS: indigotetrasulfonate, MnPc: manganese (II) phthalocyanine, Nano-Cu: nano-copper, NiCo₂O₄: nickel cobalt oxide, PLL-GA: poly-L-lysine (PLL)-glutaraldehyde (GA), PtNP: platinum nanoparticle, rGO: reduced graphene oxide, SiO₂: silicon dioxide, SnO₂: tin (IV) oxide

2.4 References

- Anson, F. C. (1975). Patterns of ionic and molecular adsorption at electrodes. *Acc. Chem. Res.*, *8*, 400-407.
- Aparna, T. K., Sivasubramanian, R., and Dar, M. A. (2018). One-pot synthesis of Au-Cu₂O/rGO nanocomposite based electrochemical sensor for selective and simultaneous detection of dopamine and uric acid. *J. Alloys Compd.*, *741*, 1130-1141.
- Batchelor-McAuley, C., and Compton, R. G. (2012). Voltammetry of multi-electron electrode processes of organic species. *J. Electroanal. Chem.*, *669*, 73-81.
- Bettelheim, A., and Kuwana, T. (2002). Rotating-ring-disk analysis of iron tetra(N-methylpyridyl) porphyrin in electrocatalysis of oxygen. *Anal. Chem.*, *51*(13), 2257-2260.
- Brainina, K. Z., and Kazakov, Y. E. (2020). Electrochemical hybrid methods and sensors for antioxidant/oxidant activity monitoring and their use as a diagnostic tool of oxidative stress: future perspectives and challenges. *Chemosensors*, *8*(4).
- Brett, C. M. A., and Brett, A. M. O. (1993). *Electrochemistry: principles, methods, and applications*: oxford university press.
- Buledi, J. A., Ameen, S., Memon, S. A., Fatima, A., Solangi, A. R., Mallah, A., Logo, F. K. E., Malakmohammadi, S., Agarwal, S., and Gupta, V. K. (2021). An improved non-enzymatic electrochemical sensor amplified with CuO nanostructures for sensitive determination of uric acid. *Open Chem.*, *19*(1), 481-491.
- Cai, W., Zhao, X., Liu, C., Xing, W., and Zhang, J. (2014). 2 - Electrode kinetics of electron-transfer reaction and reactant transport in electrolyte solution. In W. Xing, G. Yin, and J. Zhang (Eds.), *Rotating electrode methods and oxygen reduction electrocatalysts* (pp. 33-65). Amsterdam: Elsevier.
- Cheng, Y., Shi, J., Zhang, Q., Fang, C., Chen, J., and Li, F. (2022). Recent progresses in adsorption mechanism, architectures, electrode materials and applications for advanced electrosorption system: A review. *Polymers (Basel)*, *14*(15).
- Christensen, P. A., and Hamnet, A. (1993). *Techniques and mechanisms in electrochemistry*: Springer Netherlands.

- Collman, J. P., Elliott, C. M., Halbert, T. R., and Tovrog, B. S. (1977). Synthesis and characterization of "face-to-face" porphyrins. *Proc. Natl. Acad. Sci. U S A*, 74(1), 18-22.
- Compton, R., and Banks, C. (2007). *Understanding Voltammetry*.
- de Villiers, K. A., Kaschula, C. H., Egan, T. J., and Marques, H. M. (2007). Speciation and structure of ferriprotoporphyrin IX in aqueous solution: spectroscopic and diffusion measurements demonstrate dimerization, but not mu-oxo dimer formation. *J. Biol. Inorg. Chem.*, 12(1), 101-117.
- Elgrishi, N., Rountree, K. J., McCarthy, B. D., Rountree, E. S., Eisenhart, T. T., and Dempsey, J. L. (2017). A practical beginner's guide to cyclic voltammetry. *J. Chem. Educ.*, 95(2), 197-206.
- Fang, Y., Zhang, D., Xia, Q., Hong, S., Xu, Y., and Guo, Y. (2015). Fabrication of a needle microsensor and its applications in the detection of dissolved oxygen. *J. Sens.*, 2015, 1-7.
- Farahi, A., Hammani, H., Kajai, A., Lahrich, S., Bakasse, M., and El Mhammedi, M. A. (2019). Electro-catalytic detection of dopamine at carbon paste electrode modified with activated carbon: analytical application in blood samples. *Int. J. Environ. Anal. Chem.*, 100(3), 295-310.
- Feng, J.-J., Li, Z.-H., Li, Y.-F., Wang, A.-J., and Zhang, P.-P. (2011). Electrochemical determination of dioxygen and hydrogen peroxide using $\text{Fe}_3\text{O}_4@\text{SiO}_2$ @hemin microparticles. *Mikrochim. Acta.*, 176(1-2), 201-208.
- Fu, L. I., Zheng, Y., Fu, Z., Wang, A., and Cai, W. E. N. (2015). Dissolved oxygen detection by galvanic displacement-induced graphene/silver nanocomposite. *Bull. Mater. Sci.*, 38(3), 611-616.
- Gao, Y., and Chen, J. (2005). Electrocatalysis of carbon dioxide with hemin and hemin-coated latex. *J. Electroanal. Chem.*, 583(2), 286-291.
- Gileadi, E. (1967). Adsorption in Electrochemistry. In E. Gileadi (Ed.), *Electrosorption* (pp. 1-18). Boston, MA: Springer US.
- Glanc, M., Sophocleous, M., Atkinson, J. K., and Garcia-Breijo, E. (2013). The effect on performance of fabrication parameter variations of thick-film screen printed

- silver/silver chloride potentiometric reference electrodes. *Sens. Actuators A: Phys.*, *197*, 1-8.
- Glantzounis, G. K., Tsimoyiannis, E. C., Kappas, A. M., and Galaris, D. A. (2005). Uric acid and oxidative stress. *Curr. Pharm. Des.*, *11*(32), 4145-4151.
- Govindasamy, M., Chen, S.-M., Mani, V., Sathiyar, A., Merlin, J. P., Al-Hemaid, F. M. A., and Ali, M. A. (2016). Simultaneous determination of dopamine and uric acid in the presence of high ascorbic acid concentration using cetyltrimethylammonium bromide–polyaniline/activated charcoal composite. *RSC Adv.*, *6*(102), 100605-100613.
- Guelcin, I., Oktay, M., Koeksal, E., Serbetci, H., Beydemir, S., and Kuefrevioglu, O. (2008). Antioxidant and radical scavenging activities of uric acid. *Asian J. Chem.*, *20*(3).
- Hibbert, D. B. (1993). Introduction to electrochemistry. In D. B. Hibbert (Ed.), *Introduction to electrochemistry* (pp. 1-10). London: Macmillan Education UK.
- Hsu, L. H.-H., Deen, M. J., and Selvaganapathy, P. R. (2017). Complete solid state dissolved oxygen sensor using hemin electrocatalyst and palladium-reusable reference electrode. *IEEE Sens. J.*, 1-1.
- Hsu, L. H. H., and Selvaganapathy, P. R. (2013, 3-6 Nov. 2013). Development of a low cost Hemin based dissolved oxygen sensor with anti-biofouling coating for water monitoring. Paper presented at the SENSORS, 2013 IEEE.
- Huang, X., and Groves, J. T. (2018). Oxygen activation and radical transformations in heme proteins and metalloporphyrins. *Chem. Rev.*, *118*(5), 2491-2553.
- Jindal, K., Tomar, M., and Gupta, V. (2012). CuO thin film based uric acid biosensor with enhanced response characteristics. *Biosens Bioelectron*, *38*(1), 11-18.
- Kameda, T., Horikoshi, K., Kumagai, S., Saito, Y., and Yoshioka, T. (2020). Adsorption of urea, creatinine, and uric acid from three solution types using spherical activated carbon and its recyclability. *Chin. J. Chem. Eng.*, *28*(12), 2993-3001.
- Krishnamoorthy, K., Sudha, V., Senthil Kumar, S. M., and Thangamuthu, R. (2018). Simultaneous determination of dopamine and uric acid using copper oxide nano-rice modified electrode. *J. Alloys Compd.*, *748*, 338-347.

- Lakard, S., Pavel, I. A., and Lakard, B. (2021). Electrochemical biosensing of dopamine neurotransmitter: A review. *Biosensors (Basel)*, 11(6).
- Lawal, A. T., Bolarinwa, H. S., Animasahun, L. O., Adeoye, M. D., Abdulsalami, I. O., and Alabi, K. A. (2019). Progress in carbon nanotube-based electrochemical biosensors – A review. *FUJNAS*, 8(2).
- Li, W., Aoki, K. J., Chen, J., and Nishiumi, T. (2015). Conditions of predominant occurrence of catalytic reduction of O₂ by ferrous hemin over formation of ferrous hemin-O₂ adduct. *J. Electroanal. Chem.*, 743, 134-138.
- Liu, C., Liang, X., Liu, X., Wang, Q., Zhan, L., Zhang, R., Qiao, W., and Ling, L. (2008). Surface modification of pitch-based spherical activated carbon by CVD of NH₃ to improve its adsorption to uric acid. *Appl. Surf. Sci.*, 254(21), 6701-6705.
- Marahel, F., Ghaedi, M., and Ansari, A. (2015). Zinc oxide nanoparticles loaded on activated carbon and its application for adsorption removal of uric acid. *Synth. React. Inorg. M.*, 45(9), 1387-1395.
- Mei, L.-P., Feng, J.-J., Wu, L., Chen, J.-R., Shen, L., Xie, Y., and Wang, A.-J. (2016). A glassy carbon electrode modified with porous Cu₂O nanospheres on reduced graphene oxide support for simultaneous sensing of uric acid and dopamine with high selectivity over ascorbic acid. *Mikrochim. Acta.*, 183(6), 2039-2046.
- Mikhelson, K. N. (2018). Voltammetric sensing of dopamine in urine samples with electrochemically activated commercially available screen-printed carbon electrodes. *Int. J. Biosens. Bioelectron.*, 4(4).
- Moeller, T., Bailar, J. C., Kleinberg, J., Guss, C. O., Castellion, M. E., and Metz, C. (1980). 24 - ELECTROCHEMISTRY. In T. Moeller, J. C. Bailar, J. Kleinberg, C. O. Guss, M. E. Castellion, and C. Metz (Eds.), *Chemistry* (pp. 744-764): Academic Press.
- Momtazan, F., Vafaei, A., Ghaedi, M., Ghaedi, A. M., Emadzadeh, D., Lau, W.-J., and Baneshi, M. M. (2018). Application of copper sulfide nanoparticles loaded activated carbon for simultaneous adsorption of ternary dyes: Response surface methodology. *Korean J. Chem. Eng.*, 35(5), 1108-1118.
- Maurya, R., Das, R., Tripathi, A. K., and Neergat, M. (2022). Relationship between the electron-transfer coefficients of the oxygen reduction reaction estimated from

- the Gibbs free energy of activation and the Butler-Volmer equation. *Phys. Chem. Chem. Phys.*, 25(1), 700-707.
- Nimse, S. B., and Pal, D. (2015). Free radicals, natural antioxidants, and their reaction mechanisms. *RSC Advances*, 5(35), 27986-28006.
- Ning, J., He, Q., Luo, X., Wang, M., Liu, D., Wang, J., Li, G., and Liu, J. (2018). Determination of uric acid in co-presence of dopamine and ascorbic acid using cuprous oxide nanoparticle-functionalized graphene decorated glassy carbon electrode. *Catalysts*, 8(10).
- Noroozifar, M., Khorasani-Motlagh, M., Jahromi, F. Z., and Rostami, S. (2013). Sensitive and selective determination of uric acid in real samples by modified glassy carbon electrode with holmium fluoride nanoparticles/multi-walled carbon nanotube as a new biosensor. *Sens. Actuators B: Chem.*, 188, 65-72.
- Öztürk Doğan, H., Kurt Urhan, B., Çepni, E., and Eryiğit, M. (2019). Simultaneous electrochemical detection of ascorbic acid and dopamine on Cu₂O/CuO/electrochemically reduced graphene oxide (Cu_xO/ERGO)-nanocomposite-modified electrode. *Microchem. J.*, 150.
- Pasternack, R. F., and Halliwell, B. (2002). Superoxide dismutase activities of an iron porphyrin and other iron complexes. *J. Am. Chem. Soc.*, 101(4), 1026-1031.
- Qi, S., Zhao, B., Tang, H., and Jiang, X. (2015). Determination of ascorbic acid, dopamine, and uric acid by a novel electrochemical sensor based on pristine graphene. *Electrochim. Acta.*, 161, 395-402.
- Sajid, M., Nazal, M. K., Mansha, M., Alsharaa, A., Jillani, S. M. S., and Basheer, C. (2016). Chemically modified electrodes for electrochemical detection of dopamine in the presence of uric acid and ascorbic acid: A review. *TrAC, Trends Anal. Chem.*, 76, 15-29.
- Santos, L. S., Landers, R., and Gushikem, Y. (2011). Application of manganese (II) phthalocyanine synthesized in situ in the SiO₂/SnO₂ mixed oxide matrix for determination of dissolved oxygen by electrochemical techniques. *Talanta*, 85(2), 1213-1216.

- Şavk, A., Aydın, H., Cellat, K., and Şen, F. (2020). A novel high performance non-enzymatic electrochemical glucose biosensor based on activated carbon-supported Pt-Ni nanocomposite. *J. Mol. Liq.*, 300.
- Savk, A., Ozdil, B., Demirkan, B., Nas, M. S., Calimli, M. H., Alma, M. H., Inamuddin, Asiri, A. M., and Sen, F. (2019). Multiwalled carbon nanotube-based nanosensor for ultrasensitive detection of uric acid, dopamine, and ascorbic acid. *Mater. Sci. Eng. C*, 99, 248-254.
- Sheikh-Mohseni, M. A., and Pirsai, S. (2016). Nanostructured conducting polymer/copper oxide as a modifier for fabrication of L-DOPA and uric Acid electrochemical sensor. *Electroanalysis*, 28(9), 2075-2080.
- Shen, H., Thomas, T., Rasaki, S. A., Saad, A., Hu, C., Wang, J., and Yang, M. (2019). Oxygen reduction reactions of Fe-N-C catalysts: current status and the way forward. *Electrochem. Energy Rev.*, 2(2), 252-276.
- Sheng, Z.-H., Zheng, X.-Q., Xu, J.-Y., Bao, W.-J., Wang, F.-B., and Xia, X.-H. (2012). Electrochemical sensor based on nitrogen doped graphene: simultaneous determination of ascorbic acid, dopamine and uric acid. *Biosens Bioelectron.*, 34(1), 125-131.
- Si, F., Zhang, Y., Yan, L., Zhu, J., Xiao, M., Liu, C., Xing, W., and Zhang, J. (2014). 4 - Electrochemical oxygen reduction reaction. In W. Xing, G. Yin, and J. Zhang (Eds.), *Rotating Electrode Methods and Oxygen Reduction Electrocatalysts* (pp. 133-170). Amsterdam: Elsevier.
- Siddika, M., Hasan, M. M., Oyshi, T. A., and Hasnat, M. A. (2023). Electrocatalytic reduction of O₂ by ITO-IrOx: implication for dissolved oxygen sensor in the alkaline medium. *Electrochem*, 4(2), 145-155.
- Sokolov, S. V., Sepunaru, L., and Compton, R. G. (2017). Taking cues from nature: Hemoglobin catalysed oxygen reduction. *Appl. Mater. Today.*, 7, 82-90.
- Song, Y., Gong, C., Su, D., Shen, Y., Song, Y., and Wang, L. (2016). A novel ascorbic acid electrochemical sensor based on spherical MOF-5 arrayed on a three-dimensional porous carbon electrode. *Anal. Methods*, 8(10), 2290-2296.

- Sophocleous, M., and Atkinson, J. K. (2017). A review of screen-printed silver/silver chloride (Ag/AgCl) reference electrodes potentially suitable for environmental potentiometric sensors. *Sens. Actuators A: Phys.*, *267*, 106-120.
- Sun, C. L., Chang, C. T., Lee, H. H., Zhou, J., Wang, J., Sham, T. K., and Pong, W. F. (2011). Microwave-assisted synthesis of a core-shell MWCNT/GONR heterostructure for the electrochemical detection of ascorbic acid, dopamine, and uric acid. *ACS Nano*, *5*(10), 7788-7795.
- Sun, C. L., Lee, H. H., Yang, J. M., and Wu, C. C. (2011). The simultaneous electrochemical detection of ascorbic acid, dopamine, and uric acid using graphene/size-selected Pt nanocomposites. *Biosens. Bioelectron*, *26*(8), 3450-3455.
- Tsai, T.-H., Wang, S.-H., and Chen, S.-M. (2011). Electrodeposited indigotetrasulfonate film onto glutaraldehyde-cross-linked poly-L-lysine modified glassy carbon electrode for detection of dissolved oxygen. *J. Electroanal. Chem.*, *659*(1), 69-75.
- Uskoković, V. (2021). A historical review of glassy carbon: Synthesis, structure, properties and applications. *Carbon Trends*, *5*.
- Venton, B. J., and DiScenza, D. J. (2020). Chapter 3 - Voltammetry. In B. Patel (Ed.), *Electrochemistry for Bioanalysis* (pp. 27-50): Elsevier.
- Waddell, K. M., Darby, D. W., Theobald, S. M., and Management, U. S. B. o. L. (1985). *Chemical and physical characteristics of water and sediment in scofield reservoir, Carbon County, Utah*: U.S. Geological Survey.
- Wang, C., Du, J., Wang, H., Zou, C. e., Jiang, F., Yang, P., and Du, Y. (2014). A facile electrochemical sensor based on reduced graphene oxide and Au nanoplates modified glassy carbon electrode for simultaneous detection of ascorbic acid, dopamine and uric acid. *Sens. Actuators B: Chem.*, *204*, 302-309.
- Wang, C., Li, J., Shi, K., Wang, Q., Zhao, X., Xiong, Z., Zou, X., and Wang, Y. (2016). Graphene coated by polydopamine/multi-walled carbon nanotubes modified electrode for highly selective detection of dopamine and uric acid in the presence of ascorbic acid. *J. Electroanal. Chem.*, *770*, 56-61.

- Wang, H., Ren, F., Wang, C., Yang, B., Bin, D., Zhang, K., and Du, Y. (2014). Simultaneous determination of dopamine, uric acid and ascorbic acid using a glassy carbon electrode modified with reduced graphene oxide. *RSC Advances*, 4(51), 26895-26901.
- Wang, J. (2006). *Analytical Electrochemistry*: Wiley.
- Wang, Q., Wen, X., and Kong, J. (2020). Recent progress on uric acid detection: A review. *Crit. Rev. Anal. Chem.*, 50(4), 359-375.
- Wang, Y., Hosono, T., and Hasebe, Y. (2013). Hemin-adsorbed carbon felt for sensitive and rapid flow-amperometric detection of dissolved oxygen. *Microchimica Acta.*, 180(13-14), 1295-1302.
- Waryani, B., Tahira, A., Ameen, S., Willande, M., Abbasi, A. R., and Ibupoto, Z. H. (2020). The enzyme free uric acid sensor based on iron doped CuO nanostructures for the determination of uric acid from commercial seafood. *J. Electron. Mater.*, 49(10), 6123-6129.
- Yan, Q., Zhi, N., Yang, L., Xu, G., Feng, Q., Zhang, Q., and Sun, S. (2020). A highly sensitive uric acid electrochemical biosensor based on a nano-cube cuprous oxide/ferrocene/uricase modified glassy carbon electrode. *Sci. Rep.*, 10(1), 10607.
- Yang, J., Chen, J., Zhou, Y., and Wu, K. (2011). A nano-copper electrochemical sensor for sensitive detection of chemical oxygen demand. *Sens. Actuators B: Chem.*, 153(1), 78-82.
- Yang, S., Li, G., Yin, Y., Yang, R., Li, J., and Qu, L. (2013). Nano-sized copper oxide/multi-wall carbon nanotube/Nafion modified electrode for sensitive detection of dopamine. *J. Electroanal. Chem.*, 703, 45-51.
- Yu, L., Liu, J., Yin, W., Yu, J., Chen, R., Song, D., Liu, Q., Li, R., and Wang, J. (2020). Ionic liquid combined with NiCo₂O₄/rGO enhances electrochemical oxygen sensing. *Talanta*, 209, 120515.
- Zannotti, M., and Giovannetti, R. (2015). Kinetic evidence for the effect of salts on the oxygen solubility using laboratory prototype aeration system. *J. Mol. Liq.*, 211, 656-666.

- Zhang, D., Fang, Y., Miao, Z., Ma, M., and Chen, Q. (2013). Electrochemical determination of dissolved oxygen based on three dimensional electrosynthesis of silver nanodendrites electrode. *J. Appl. Electrochem.*, 44(3), 419-425.
- Zhang, S., Xu, F., Liu, Z. Q., Chen, Y. S., and Luo, Y. L. (2019). Novel electrochemical sensors from poly[N-(ferrocenyl formacyl) pyrrole]@multi-walled carbon nanotubes nanocomposites for simultaneous determination of ascorbic acid, dopamine and uric acid. *Nanotechnology*, 31(8), 085503.
- Zhang, W., Yuan, R., Chai, Y.-Q., Zhang, Y., and Chen, S.-H. (2012). A simple strategy based on lanthanum–multiwalled carbon nanotube nanocomposites for simultaneous determination of ascorbic acid, dopamine, uric acid and nitrite. *Sens. Actuators B: Chem.*, 166-167, 601-607.
- Zhao, D., Yu, G., Tian, K., and Xu, C. (2016). A highly sensitive and stable electrochemical sensor for simultaneous detection towards ascorbic acid, dopamine, and uric acid based on the hierarchical nanoporous PtTi alloy. *Biosens Bioelectron*, 82, 119-126.
- Zheng, Z., Qiu, H., Zheng, M., Weng, S., Huang, Z., Xian, R., and Lin, X. (2014). Selective electrochemical determination of dopamine in serum in the presence of ascorbic acid and uric acid by using a CuO nanoleaf electrode. *Anal. Methods*, 6(19), 7923-7927.

CHAPTER III

EXPERIMENTAL

3.1 Uric acid, ascorbic acid and dopamine sensor

3.1.1 Chemical Reagents

All chemical reagents were of analytical grade and used as received: sodium L-lactate ($C_3H_5NaO_3$, $\geq 99.0\%$, Sigma-Aldrich), citric acid anhydrous ($C_6H_8O_7$, 99.5% , QRëC), urea (CH_4N_2O , $\geq 99.0\%$, Sigma-Aldrich), calcium chloride ($CaCl_2$, 94.0% , APS Ajax Finechem), sodium chloride ($NaCl$, $\geq 99.0\%$, Sigma-Aldrich), magnesium sulfate anhydrous ($MgSO_4$, $\geq 98.0\%$, Tokyo Chemical Industry), sodium bicarbonate (Na_2HCO_3 , 99.8% , QRëC), L-ascorbic acid ($C_6H_8O_6$, $\geq 99.0\%$, Sigma-Aldrich), dopamine hydrochloride ($(HO)_2C_6H_3CH_2CH_2NH_2 \cdot HCl$, $\geq 97.5.0\%$, Sigma-Aldrich), uric acid ($C_5H_4N_4O_3$, $\geq 99.0\%$, Sigma-Aldrich), ethanol (C_2H_5OH , $\geq 99.9\%$, QRëC), hydrochloric acid (HCl , 37.0% , RCI Labscan), hydrogen peroxide (H_2O_2 , 35% , ANaPURE), sodium phosphate monobasic (NaH_2PO_4 , $\geq 99.0\%$, Sigma-Aldrich), sodium phosphate dibasic (Na_2HPO_4 , $\geq 99.0\%$, Sigma-Aldrich), hexaammineruthenium (III) chloride (98.0% , Thermo Scientific), and Nafion (D-520 dispersion, 5.0% w/w in water and 1-propanol, Alfa Aesar). Microporous carbon was obtained from IRPC Public Company Limited, Thailand. Copper (II) oxide (CuO powder, <50 nm diameter) and copper (I) oxide (Cu_2O powder, <5 μm diameter) were obtained from Sigma-Aldrich. Multi-walled carbon nanotube ($20-40$ nm diameter, $5-15$ μm length, $\geq 95\%$) was purchased from Tokyo Chemical Industry. The commercially available electrode materials (CuO , Cu_2O , multi-walled carbon nanotube, and microporous carbon) were used as received without further purification, modification, or activation.

3.1.2 Electrochemical Studies

All electrochemical experiments were carried out using a Metrohm 910 PSTAT Mini potentiostat (Metrohm, Netherlands) and a standard three-electrode system in a Faraday cage thermostated at 25 °C. A glassy carbon electrode (GCE, 3.0 mm diameter, Italsens, Netherlands), a silver/silver chloride electrode (Ag/AgCl in saturated KCl, Italsens, Netherlands), and a platinum coil (Redoxme AB, Sweden) were used as working, reference, and counter electrodes, respectively.

In differential pulse voltammetry (DPV) analysis of the AA, DA, and UA mixtures, when it was not possible to determine the regression front baseline, peak currents were assessed by selecting two baseline points on either side of the DPV peak. These points were then connected to create a linear baseline (Brown and Anson, 2002). It is noteworthy that the currents extrapolated to this linear baseline on a microporous carbon electrode are similar to the response observed in a blank electrolyte, validating this method as appropriate for baseline correction in DPV measurements of the solution mixtures.

3.1.3 Electrode Preparation and Characterization

The glassy carbon electrode (GCE) working electrode was cleaned by polishing with 1.0, 0.3, and 0.05 μm alumina powder (Buehler, USA) on soft lapping pads (Buehler, USA) prior to use. In the preparation of modified electrodes, 1.0 mg of microporous carbon, CuO, Cu₂O, or CNT was dispersed in 1.0 mL of ethanol and sonicated for 5 minutes. Subsequently, the suspension was drop-cast onto a clean GCE surface and dried in a vacuum oven (Faithful, DZ-A/BC II Series, Huanghua City, China) at 55 °C for 10 minutes. Additionally, to assess the effect of Nafion coating, a 0.5 wt% Nafion solution in ethanol (1.0 μL) was coated onto the treated GCE surface and dried in a vacuum oven. The porosity of microporous carbon was investigated using N₂ adsorption/desorption isotherms. The specific surface area and pore sizes

were calculated using the Brunauer-Emmett-Teller (BET) analysis at the pressures $5.8 \times 10^{-7} \leq P/P_0 \leq 1.00$ at 77 K carried out using a 3Flex Physisorption – Surface Characterization Analyzer (Micromeritics, ATS Scientific Inc., Burlington, Canada). The morphology of microporous carbon was characterized using a field emission scanning electron microscope (FE-SEM, 3.00 kV, Zeiss AURIGA). Surface chemical analysis of microporous carbon was performed using Fourier transform infrared spectroscopy (ATR-FTIR, Bruker Tensor 27, Germany) in the spectral range of 400 - 4000 cm^{-1} . The electroactive surface area of the electrodes was estimated by cyclic voltammetry measurements in 1.0 mM hexaamineruthenium (III) or RuHex in the presence of 0.10 M KCl supporting electrolyte at varied scan rates (10 – 400 mV s^{-1}). The thickness and optical profile of the microporous carbon electrodes were measured using a laser confocal microscope (OLYMPUS OLS5100, Tokyo, Japan).

3.1.4 Application to Synthetic Urine Samples

The developed method was validated by spiking and recovery tests (standard addition) of AA, DA, and UA in synthetic urine samples in the presence of 0.10 M HCl. Synthetic urine was prepared according to Jiang et al (Jiang et al., 2016). The synthetic urine consists of 11.0 mM sodium L-lactate, 2.0 mM citric acid, 25.0 mM NaHCO_3 , 170.0 mM urea, 2.5 mM CaCl_2 , 90.0 mM NaCl , 2.0 mM MgSO_4 , 10.0 mM Na_2SO_4 , 7.0 mM NaH_2PO_4 , and 7.0 mM Na_2HPO_4 . The samples were subjected to differential pulse voltammetry in the potential range of - 0.2 to + 0.9 V at an MC/GCE electrode at the scan rate of 10 mV s^{-1} , pulse amplitude of 0.01 V, and pulse width of 50 ms. The obtained results were analyzed and reported as percentage recovery (the mean value of triplicate measurements \pm standard deviation).

3.2 Oxygen sensor

3.2.1 Chemical reagents

All chemical reagents were of analytical grade and used as received: hemin ($C_{34}H_{32}ClFeN_4O_4$, >95.0%, Tokyo Chemical Industry Co., Ltd. (APAC)), potassium chloride (KCl, >99.0%, Sigma-Aldrich), and sodium hydroxide (NaOH, >98.5%, Sigma-Aldrich). Oxygen (O_2 , >99.0%) and nitrogen gases (N_2 , >99.0%) were purchased from Thai Special Gas Co., Ltd. Hemin solutions were prepared by dissolving them in deionized water containing 0.040 M NaOH to enhance the solubility of hemin, along with 1.0 M KCl, which served as a supporting electrolyte. The concentration of O_2 was measured using a commercially available DO meter (PDO-520 LUTRON Dissolved Oxygen Meter).

3.2.2 Characterization of hemin powder and hemin solution

The UV-visible spectra of hemin solutions were recorded over wavelengths ranging from 200 to 900 nm using a UV-vis Spectrophotometer (Cary60, Agilent Technologies, United States). Additionally, the functional groups of hemin powder were analyzed using Fourier transform infrared spectroscopy (ATR-FTIR, Bruker Tensor 27, Germany) within the spectral range of 400 – 4000 cm^{-1} .

3.2.3 Preparation of hemin solutions at various KCl concentrations at saturated O_2 conditions

A 200 μM hemin solution was prepared by directly dissolving hemin in a small quantity of 0.04 M NaOH and deionized (DI) water, containing different KCl concentrations 0.1 M, 0.4 M, 0.7 M, and 1.0 M KCl. The hemin solution was purged with O_2 gas at a flow rate of 0.50 L min^{-1} for 3 minutes. The GCE was immediately immersed in the hemin solution after bubbling saturated O_2 gas. CV measurements

were conducted within the potential range from -0.1 V to 0.1 V with a scan rate of 100 mV s⁻¹.

3.2.4 Preparation of hemin solution in high salt concentration in the absence of O₂ molecules

The hemin solutions (0 – 100 μM) were prepared by dissolving hemin directly in a small quantity of 0.04 M NaOH and deionized (DI) water, containing 1.0 M KCl concentration. The hemin solution was bubbled with N₂ gas at a flow rate of 0.50 L min⁻¹ for 3 minutes. The GCE was immediately immersed in the hemin solution after bubbling N₂ gas. CV measurements were conducted within the potential range from -0.1 V to 0.1 V, with a scan rate of 100 mV s⁻¹.

3.2.5 Preparation of O₂ saturated 1.0 M KCl without hemin

1.0 M KCl concentration was bubbled with O₂ gas at a flow rate of 0.50 L min⁻¹ for 3 minutes. The GCE was immediately immersed in the hemin solution after bubbling saturated O₂ gas. CV measurements were conducted within the potential range from -0.1 V to 0.1 V with a scan rate of 100 mV s⁻¹.

3.2.6 Preparation of various hemin solution at saturated O₂ concentrations

The hemin solutions (0 – 80 nM) were prepared by dissolving hemin directly in a small quantity of 0.04 M NaOH and deionized (DI) water, containing 1.0 M KCl concentration. The hemin solution was purged with O₂ gas at a flow rate of 0.50 L min⁻¹ for 3 minutes. The GCE was immediately immersed in the hemin solution after bubbling saturated O₂ gas. CV measurements were conducted within the potential range from -0.1 V to 0.1 V with a scan rate of 100 mV s⁻¹.

3.2.7 Preparation of hemin solution at various O₂ concentrations

A hemin solution was prepared by directly dissolving hemin in a small quantity of 0.04 M NaOH and deionized (DI) water, containing 1.0 M KCl. The specific O₂ concentration in the hemin solution was varied by altering the partial pressure of O₂ or using N₂ over different time durations at a flow rate of 0.50 L min⁻¹. The GCE was immediately immersed in the hemin solution after bubbling N₂ or O₂ gas. The concentration of O₂ was confirmed using a commercially available DO meter. The O₂ concentration decreases with increasing duration of time. CV measurements were conducted within the potential range from - 0.1 V to 0.1 V with a scan rate of 100 mV s⁻¹.

3.2.8 Electrochemical measurements

All electrochemical experiments were conducted using a Palmsens4 potentiostat within a Faraday cage maintained at 25 °C, employing a standard three-electrode system. The working electrode was a glassy carbon electrode (GCE, 3.0 mm diameter, Italsens, Netherlands), the reference electrode was a silver/silver chloride electrode (Ag/AgCl in saturated KCl, Italsens, Netherlands), and the counter electrode was a platinum coil (Redoxme AB, Sweden). Deionized water (DI) was obtained from the Elga Purelab Ultra water purification system (Elga Labwater, UK). The electrochemical properties of hemin were investigated through cyclic voltammetry measurements (CV) at a glassy carbon electrode within the potential range from -0.1 V to 0.1 V, with a scan rate of 100 mV s⁻¹.

3.3 Reference

Brown, A. P., and Anson, F. C. (2002). Cyclic and differential pulse voltammetric behavior of reactants confined to the electrode surface. *Anal. Chem.*, 49(11), 1589-1595.

Jiang, G., Wang, J., Yang, Y., Zhang, G., Liu, Y., Lin, H., Zhang, G., Li, Y., and Fan, X. (2016). Fluorescent turn-on sensing of bacterial lipopolysaccharide in artificial urine sample with sensitivity down to nanomolar by tetraphenylethylene based aggregation induced emission molecule. *Biosens Bioelectron*, 85, 62-67.



CHAPTER IV

SELECTIVE ELECTRO-OXIDATION OF MOLECULAR BIOMARKERS AT MICROPOROUS CARBON ELECTRODES

4. Results and discussion

First, the electrochemical properties of AA, DA, and UA were investigated at different electrode materials: CuO, Cu₂O, Nafion, carbon nanotube (CNT), and microporous carbon (MC). The electrode which showed the highest selectivity and sensitivity in the analysis of AA, DA, and UA was then chosen for further studies. The measuring conditions such as pH, scan rates, and pulse amplitude were optimized. The developed sensor was then validated in synthetic urine sample and applied in the investigation of peroxide scavenging properties.

4.1 Effects of electrode material

The electrochemical behaviors of AA, DA, and UA were investigated at selected low-cost copper- and carbon-based electrode materials, including copper (II) oxide (CuO), copper (I) oxide (Cu₂O), carbon nanotube (CNT), and microporous carbon (MC). The materials (10 µg) were immobilized on the glassy carbon electrode (GCE) and subjected to voltammetric measurements in 100 µM AA, 100 µM DA, and 100 µM UA in the presence of 0.10 M KCl electrolyte at the scan rate of 10 mV s⁻¹.

Overall, electrode modifications with CuO, Cu₂O, CNT, and MC yielded higher peak currents and thus higher sensitivities than a bare GCE due to an increase in the electroactive surface area (**Figure 4.1**). However, the voltammetric waveshapes and the selectivity of the measurements differ from material to material.

At bare GCE (**Figure 4.1a**), CNT/GCE (**Figure 4.1b**), and CuO/GCE (**Figure 4.1c**), the voltammetric responses showed broad overlapping oxidation peaks of AA, DA, and UA, indicating poor selectivity of the electrodes. It is therefore not possible to

determine the concentrations of individual AA, DA, and UA species due to the overlapping peak positions.

At $\text{Cu}_2\text{O}/\text{GCE}$ (**Figure 4.1d**), three anodic peaks were observed in the oxidation of AA, DA, and UA at 0.21 V, 0.40 V, and 0.64 V, respectively. However, the peaks were still relatively broad and slightly overlapping, lowering the accuracy in the quantification of each species.

At MC/GCE (**Figure 4.1e**), three well-resolved anodic peaks of AA, DA, and UA were observed at 0.14 V, 0.40 V, and 0.56 V, respectively. The occurrence of the AA, DA, and UA peaks at low overpotentials (cf. bare GCE) clearly indicated the electrocatalytic activities of the microporous carbon. The large separation of the peak potentials allows simultaneous selective detection of the individual concentrations of AA, DA, and UA.

The microporosity of the electrode material altered the mass transport behaviours of AA, DA, and UA from 'planar/linear diffusion' to 'thin layer diffusion,' causing the shift in the peak potentials. As the electrochemical parameters such as formal potentials (E_f), standard electrochemical rate constants (k_0) and transfer coefficients (β) of the three species are different, the voltammetric peaks shifted to different extents, which in this case inducing wider separation of the voltammetric peaks. In addition, the presence of various functional groups on the surface of the microporous carbon and the different interactions of the surface with AA, DA, and UA, which take part in the inner-sphere electron transfer processes, may also contribute to the improved selectivity of the electrode (Ngamchuea and Chaisiwamongkhon, 2018).

In addition to nanomaterials, the use of conductive polymers as part of the protective and selective electrode component has been widely employed in electrochemical sensors (Naveen, Gurudatt, and Shim, 2017). Nafion, in particular, has been demonstrated to show enhanced analytical performances towards the detection of molecular biomarkers such as serotonin (Khoshnevisan et al., 2019), histamine (Liu and Cao, 2021) as well as uric acid, ascorbic acid, and dopamine (Atta, Galal, Ali, and El-Said, 2014; Z. Xu et al., 2019). In an attempt to further improve the

performance of microporous carbon electrodes, the effect of Nafion coating was next evaluated in **Figure 4.1f**.

At Nafion/MC/GCE, the anodic peaks of DA and UA were observed at 0.40, and 0.56 V, respectively. The peak currents of DA increased, while that of UA decreased and the signal of AA completely disappeared in the presence of Nafion coating. The effects of pH on the electrochemical responses of AA, DA, and UA at Nafion/MC/GCE electrodes have also been investigated as shown in **Figure 4.2**. The pK_a values of AA, DA, and UA are 4.17, (Shad et al., 2011) 8.87, (Jeong and Jeon, 2008; Tukimin, Abdullah, and Sulaiman, 2018) and 5.40, (Benn et al., 2018) respectively. At pH 1.0, AA, DA, and UA are in their protonated forms, and the clear peaks of all the three species were observed at Nafion/MC/GCE electrodes. The Nafion/MC/GCE electrodes can thus also be used in the simultaneous detection of AA, DA, and UA under acidic conditions ($pH < pK_a$). At pH 7 under the measuring conditions, AA and UA were thus negatively charged, while DA was neutral. The electrostatic repulsion between the sulfonic groups of Nafion and the negatively charged AA and UA lowered the voltammetric responses of the two species. Under neutral conditions, Nafion coating may thus be suitable for selective analysis of DA the presence of AA and UA interferences. At pH 10, the CV curve were low and broad. However, the responses at Nafion/MC/GCE and MC/GCE (without Nafion) were not significantly different. Nafion was thus not employed in this work. Other electrically charged coating materials may also be selected to suit the choice of the analyte of interest, considering the pK_a of the analytes and the coating material. However, if the analysis of all the three compounds is required under neutral condition, it is preferable to use MC/GCE electrodes without Nafion coating.

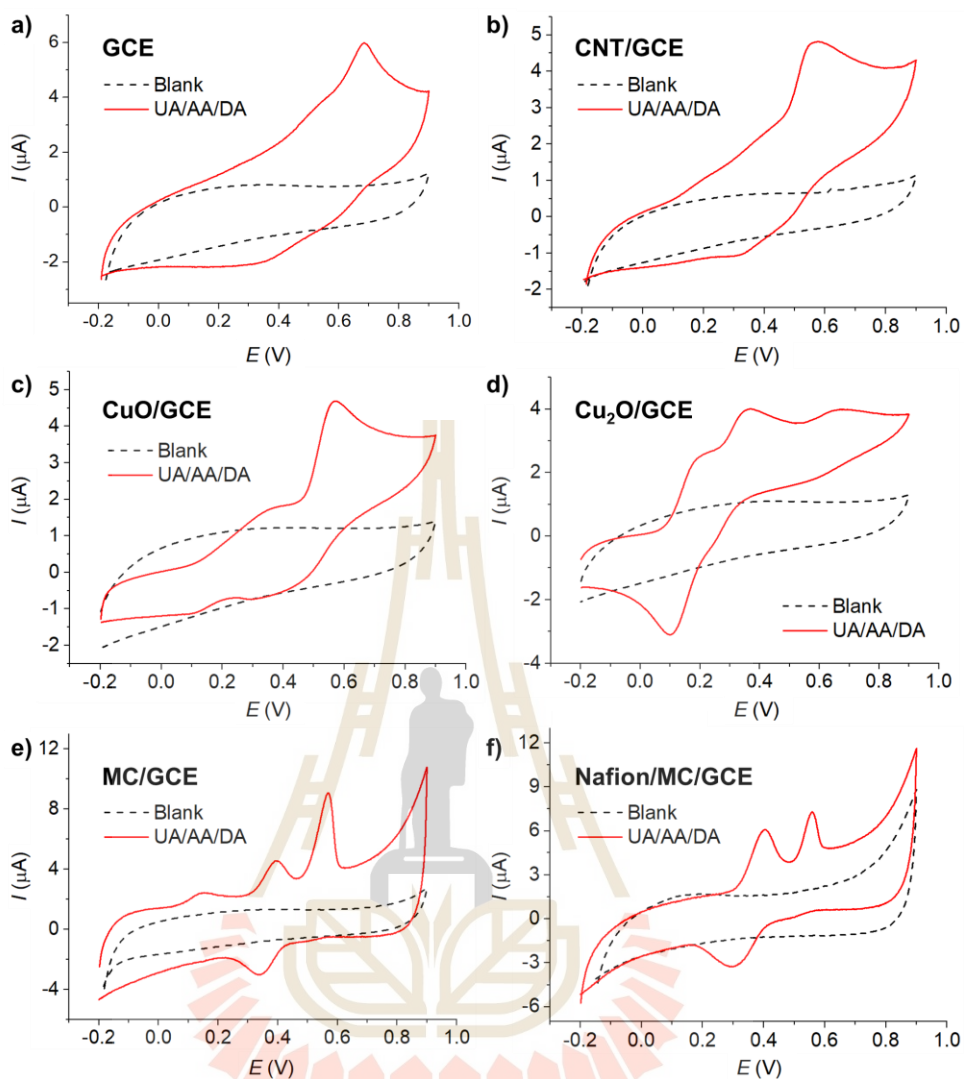


Figure 4.1 CV of 100 μM AA, 100 μM DA, and 100 μM UA in 0.10 M KCl (pH \sim 7) at different working electrodes: (a) GCE, (b) carbon nanotube (CNT/GCE), (c) copper(II) oxide (CuO/GCE), (d) copper(I) oxide (Cu₂O/GCE), (e) microporous carbon (MC/GCE), (f) Nafion-coated microporous carbon (Nafion/MC/GCE). Scan rate: 10 mV s^{-1} . E vs. Ag/AgCl (saturated KCl) reference electrode.

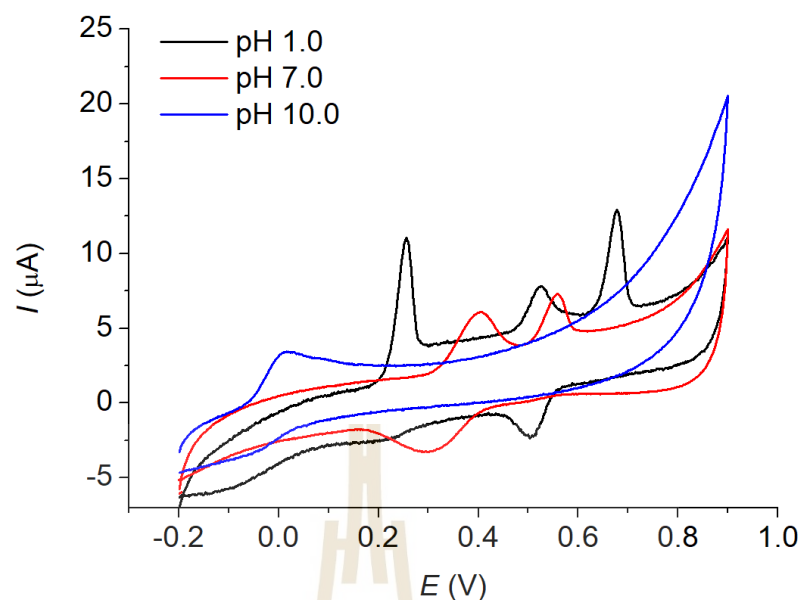


Figure 4.2 CV of 500 μM AA, 100 μM DA, and 100 μM UA at Nafion/MC/GCE electrodes at different pH. Scan rate: 10 mV s^{-1} . E vs. Ag/AgCl (saturated KCl) reference electrode.

4.2 Characterization of microporous carbon

Figure 4.3a shows the SEM image of microporous carbon. A large number of pores in the range of 2 – 34 nm were observed throughout the sample. Due to the limited resolution of the SEM (ca. 0.5 – 2 nm), only larger pores were observed, and the size distribution measured using SEM was biased towards the more easily observable larger pores. The nitrogen adsorption-desorption isotherm of microporous carbon was further used to determine the pore sizes and surface area of the microporous carbon. The microporous carbon exhibited type I isotherm (**Figure 4.3b**), confirming the characteristic microporous structure (Kaya, Şahin, and Saka, 2018). The specific surface area of the microporous carbon was determined by the Brunauer-Emmett-Teller (BET) analysis in **Figure 4.3b** (inlay) to be 1,270 $\text{m}^2 \text{g}^{-1}$ (Kaewket, Maensiri, and Ngamchuea, 2020). The pore sizes were determined from the desorption loop from the amount of N_2 adsorbate lost in the desorption step (Dollimore and Heal 1964). The Brunauer-Emmett-Teller (BET), Barrett-Joyner-Halenda (BJH), and Dollimore-Heal (DH) models predicted the average pore diameters of 1.89 nm, 2.93 nm, and 2.95 nm, respectively. The latter two models, however, used Kelvin equation of pore filling which is only applicable to mesopores and small macropores

(Dollimore and Heal 1964). From the average diameters and the morphology observed in the SEM images, the results suggested that the material consisted of a mixture of micropores and mesopores.

FT-IR analysis was used to identify functional groups on the surface of microporous carbon (**Figure 4.3c**). The broad band at $3,700\text{ cm}^{-1}$ was attributed to the O-H stretching. The stretching band of the carbonyl C=O group was observed at 1692 cm^{-1} . The bands at 1554 cm^{-1} and 2320 cm^{-1} corresponded to C=C stretching (Mojoudi et al., 2019). The peak at 1098 cm^{-1} can be assigned to C-O stretching vibration. The C-C stretching was also observed in the range of $400 - 700\text{ cm}^{-1}$ (Zhao et al., 2019; Shu et al., 2017; Hesas, Arami-Niya, Daud, and Sahu, 2013). There were thus several functional groups on the surface of micro-porous carbon which may interact with AA, DA, and UA through H-bonding and electrostatic attraction.

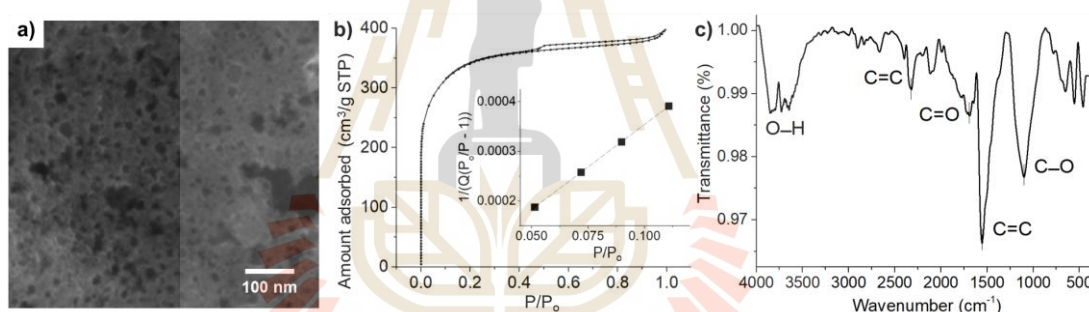


Figure 4.3 (a) SEM image, (b) N_2 adsorption-desorption isotherm, (inlay) a plot of $1/[Q(P_0/P-1)]$ against the relative pressure (P/P_0) for the determination of BET surface area, where Q is the amount of N_2 adsorbed on microporous carbon ($\text{cm}^3\text{ g}^{-1}\text{ STP}$), and (c) FT-IR spectra of microporous carbon.

4.3 Cyclic voltammetry of AA, DA, and UA at MC/GCE

4.3.1 Peak identification

The voltammograms of the individual species as well as the mixtures of AA, DA, and UA were investigated in 0.10 M KCl electrolyte at the scan rate of 10 mV s^{-1} (**Figure 4.4a**). The oxidation peaks of AA, DA, and UA were identified at 0.14 V , 0.40 V , and 0.56 V , respectively.

The voltammetric peaks of AA, DA, and UA became better resolved in acidic solution (0.10 M HCl, pH = 1, **Figure 4.4b**), possibly due to the change in the protonation states of the analytes and the surface function groups of microporous carbon altering the interaction between the two components. The effects of the solution pH will be further investigated next.

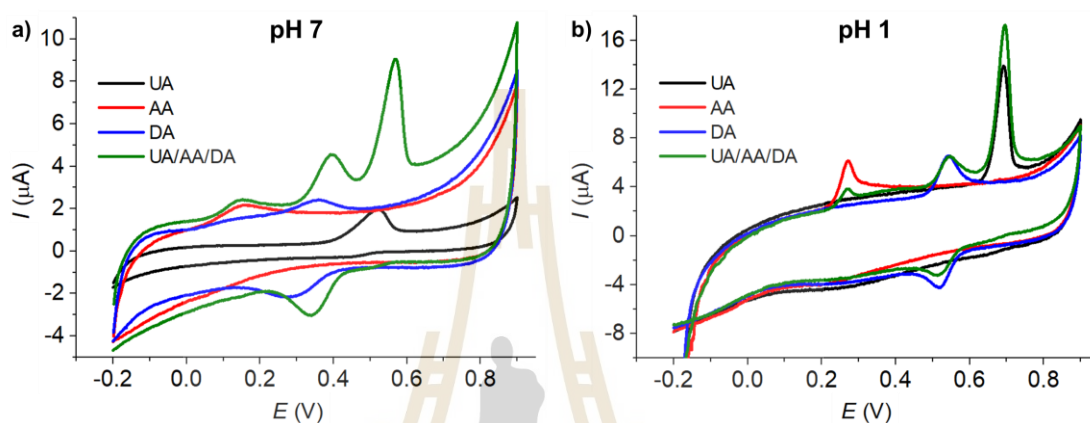


Figure 4.4 CV of (Red) 100 μM AA, (Blue) 100 μM DA, (Black) 100 μM UA and (Green) the mixture of 100 μM AA, 100 μM DA, and 100 μM UA at MC/GCE at the scan rate of 10 mV s^{-1} in different electrolytes: (a) 0.10 M KCl and (b) 0.10 M HCl. E vs. Ag/AgCl (saturated KCl) reference electrode.

4.3.2 Effects of pH

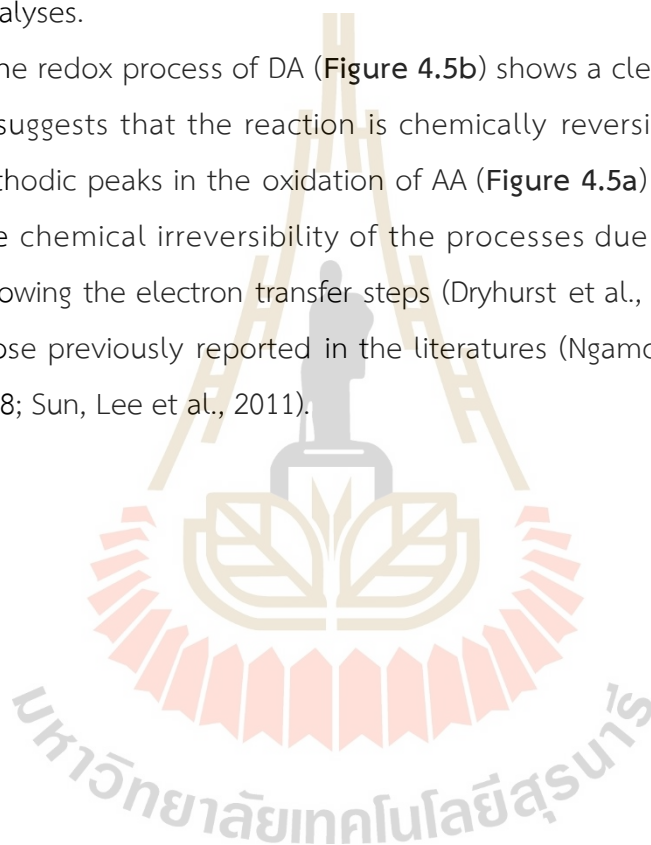
The effects of pH on the voltammetric responses of AA, DA, and UA were investigated at MC/GCE electrodes (**Figures 4.5a - c**). The anodic peak potentials (E_p) of all the three species lowered with increasing pH with the slopes of $-55.50 \pm 0.40 \text{ mV pH}^{-1}$ for DA and $-55.05 \pm 0.83 \text{ mV pH}^{-1}$ for UA, close to the theoretical Nernstian value of 59 mV pH^{-1} for an $\text{ne}^- \text{nH}^+$ process (Ngamchuea et al., 2020; Noroozifar et al., 2013). For AA, a well-defined anodic peak was only observed at pH 1.0. At other pH values, the peaks were low and broad, making it difficult to accurately determine the peak potentials.

The effects of pH on the voltammetric responses of the mixture of 100 μM AA, DA, and UA were next investigated at MC/GCE electrodes (**Figure 4.5d**). In the solution mixtures, the anodic peak potentials (E_p) of DA and UA negatively shifted

with pH with the slopes of $-56.75 \pm 0.02 \text{ mV pH}^{-1}$ and $-56.37 \pm 0.03 \text{ mV pH}^{-1}$, respectively. The slopes of E_p vs. pH of DA and UA measured in the solution mixtures were not significantly different from when measured on their own, clearly indicating that the oxidation of AA, DA, or UA is independent of the other two species.

The anodic peak currents (I_p) increased as the solutions became more acidic. The peaks were also sharper and narrower in acidic conditions, allowing better separation of the oxidation peaks of AA, DA and UA. The pH of 1.0 was thus chosen for further analyses.

The redox process of DA (**Figure 4.5b**) shows a clear backward cathodic peak which suggests that the reaction is chemically reversible. The absence of backward cathodic peaks in the oxidation of AA (**Figure 4.5a**) and UA (**Figure 4.5c**) indicates the chemical irreversibility of the processes due to further chemical reactions following the electron transfer steps (Dryhurst et al., 1972). The results are similar to those previously reported in the literatures (Ngamchuea and Batchelor-McAuley, 2018; Sun, Lee et al., 2011).



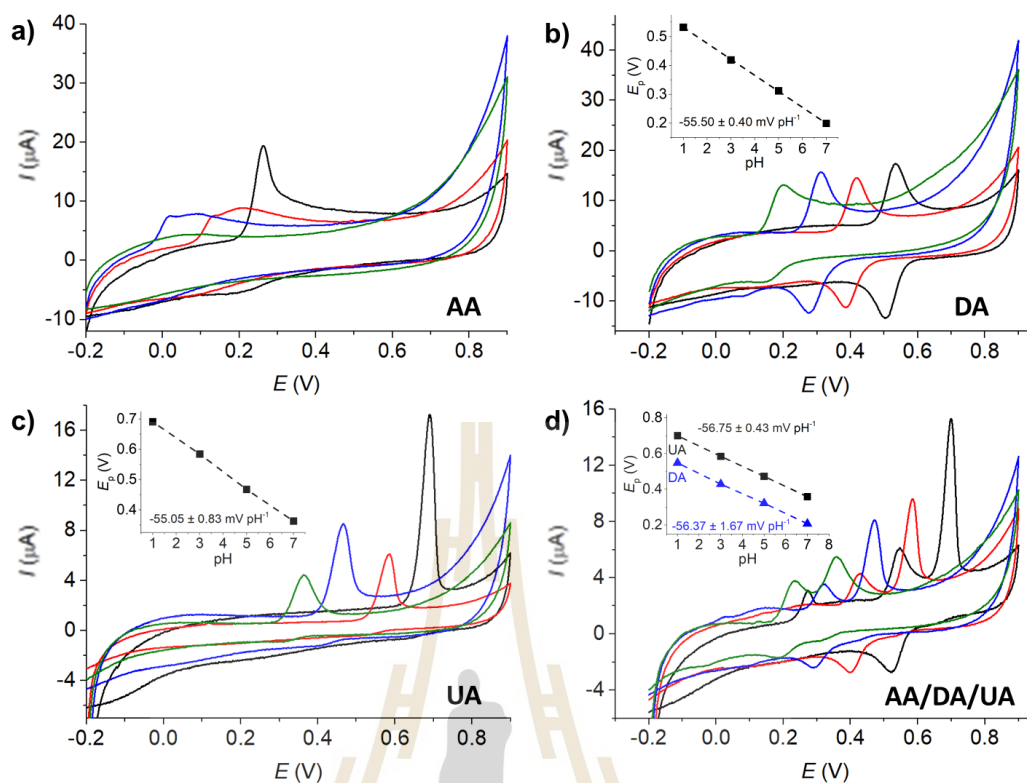


Figure 4.5 CV of (a) 100 μM AA, (b) 100 μM DA, (c) 100 μM UA, and (d) 100 μM AA, DA, and UA mixture at MC/GCE at the scan rate of 10 mV s^{-1} in aqueous buffers of various pH: (black) pH 1.0, (red) pH 3.0, (blue) pH 5.0, (green) pH 7.0. E vs. Ag/AgCl (saturated KCl) reference electrode.

4.3.3 Tafel analysis

Tafel analysis (equation 4.1) was used to investigate electron transfer kinetics at bare GCE and MC/GCE electrodes (Guidelli et al., 2014; Li, Lin, Batchelor-McAuley, Chen, and Compton, 2018).

$$\frac{\partial \ln I}{\partial E} = \frac{(n' + \beta_{n'+1})F}{RT} \quad (4.1)$$

Where I is the electrical current, E is the potential, F is the Faraday constant ($96,485 \text{ C mol}^{-1}$), R is the molar gas constant ($8.314 \text{ J K}^{-1} \text{ mol}^{-1}$), T is the absolute temperature (298 K), n' is the number of electron transfer before the rate determining step (RDS), $\beta_{n'+1}$ is the anodic transfer coefficient of the RDS. The line of

best fit of $\ln I$ vs. E was determined using currents in the range of 15 - 50% of the peak current to eliminate the mass transport effect (Kaewket et al., 2020).

Analysis of the voltammograms at the slow scan rate of 10 mV s^{-1} yielded the $n' + \beta_{n'+1}$ values at a bare GCE of 0.14 ± 0.05 , 0.17 ± 0.02 , and 0.46 ± 0.10 for AA, DA, and UA, respectively. At an MC/GCE, $n' + \beta_{n'+1}$ were determined to be 0.53 ± 0.01 , 0.34 ± 0.05 , and 0.69 ± 0.01 for AA, DA, and UA, respectively. The results thus indicated that AA, DA, and UA have similar mechanisms with the first e^- transfer being the rate determining step ($n' = 0$).

4.3.4 Effects of scan rates

Cyclic voltammetry at varied scan rates of $100 \text{ }\mu\text{M}$ UA and the mixture of $100 \text{ }\mu\text{M}$ AA, DA, and UA were first investigated at a bare GCE (Figures 4.6a - b). The anodic peak currents of UA increased linearly with square root of scan rates, indicating a diffusion-controlled process. In the mixtures of AA, DA, and UA, the oxidation responses of the three species strongly overlapped and showed the poor selectivity of the measurements at all scan rates.

The diffusion coefficient of UA was analyzed at a bare GCE (electrode surface area = $7.068 \times 10^{-6} \text{ m}^2$). The electrode size has been checked by length measurements under a microscope to yield the diameter of $3.00 \pm 0.01 \text{ mm}$. The GCE has also been characterized using hexaammineruthenium (III) or RuHex in the presence of 0.10 M KCl supporting electrolyte, a standard outer-sphere redox probe as shown in Figure 4.7. The scan rates were varied between $10 - 400 \text{ mV s}^{-1}$. The temperature was controlled at $25 \text{ }^\circ\text{C}$ (298 K). The diffusion coefficient of hexaammineruthenium (III) was calculated using the Randles-Sevcik equation (equation. 4.3) (Compton and Banks, 2018) for an electrochemically reversible one-electron transfer process to yield the diffusion coefficient of RuHex of $8.61 \times 10^{-10} \pm 0.06 \times 10^{-10} \text{ m}^2 \text{ s}^{-1}$, close to the value reported in the literature ($8.43 \times 10^{-10} \pm 0.03 \times 10^{-10} \text{ m}^2 \text{ s}^{-1}$).

$$I_p = 0.446FAc^* \sqrt{\frac{FDv}{RT}} \quad (4.2)$$

Where I_p is the peak current, F is the Faraday's constant (96,485 C mol⁻¹), A is the electrode surface area (m²), c^* is the bulk concentration of the redox analyte, v is the voltage scan rate (V s⁻¹), R is the molar gas constant (8.314 J K⁻¹ mol⁻¹), T is the absolute temperature (K), and D is the analyte diffusion coefficient (m² s⁻¹).

Next, the electrolyte was 0.10 M HCl. The diffusion coefficient of UA was determined by **equation 4.2** to be $5.09 \times 10^{-9} \pm 0.02 \times 10^{-9}$ m² s⁻¹, in the same order of magnitude as the value previously reported in the literature (3.2×10^{-5} m² s⁻¹) (Gupta and Ganesan, 2015).

$$I_p = 0.496 \sqrt{n' + \beta_{n'+1}} n F A c^* \sqrt{\frac{FvD}{RT}} \quad (4.3)$$

Where I_p is the peak current, n' is the number of electron transfer before the rate determining step (RDS), $\beta_{n'+1}$ is the anodic transfer coefficient of the RDS, n is the total number of electron transfer ($n = 2$), (Ngamchuea and Batchelor-McAuley, 2018) v is the voltage scan rate (V s⁻¹), F is the Faraday's constant (96,485 C mol⁻¹), A is the electrode surface area (m²), c^* is the bulk concentration of the redox analyte, R is the molar gas constant (8.314 J K⁻¹ mol⁻¹), T is the absolute temperature (K), and D is the analyte diffusion coefficient (m² s⁻¹) (Compton and Banks, 2018).

At MC/GCE electrodes, the anodic peak currents of UA also increased linearly with square root of scan rates, indicating a diffusion-controlled process (**Figure 4.6c**). The simultaneous oxidation of AA, DA, and UA gave well-defined and widely separated peaks at MC/GCE electrodes (**Figure 4.6d**). The three anodic peaks of AA, DA, and UA were better resolved at slow scan rates. The scan rate of 10 mV s⁻¹ was thus chosen as the optimal condition for the simultaneous detection of AA, DA, and UA.

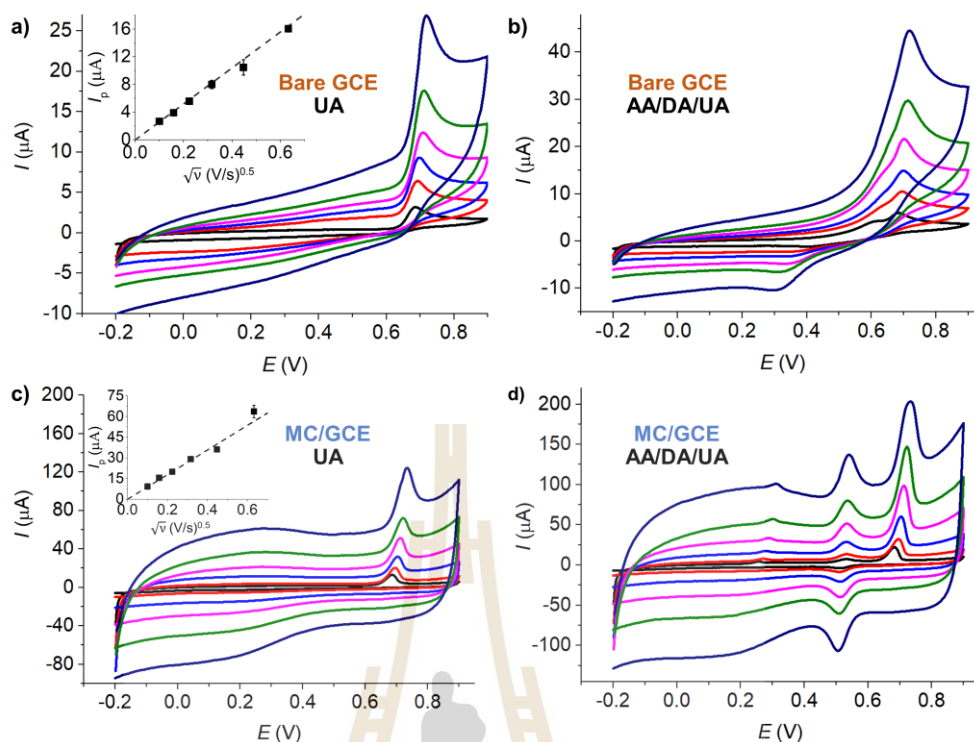


Figure 4.6 CV at bare GCE at varied scan rates of (a) 100 μM UA and (b) 100 μM AA, DA, UA. CV at MC/GCE at varied scan rates of (c) 100 μM UA and (d) 100 μM AA, DA, UA. (black) 10 mV s^{-1} , (red) 25 mV s^{-1} , (blue) 50 mV s^{-1} , (pink) 100 mV s^{-1} , (green) 200 mV s^{-1} , and (dark blue) 400 mV s^{-1} . All measurements were performed in the presence of 0.10 M HCl at pH 1.0. E vs. Ag/AgCl (saturated KCl) reference electrode.

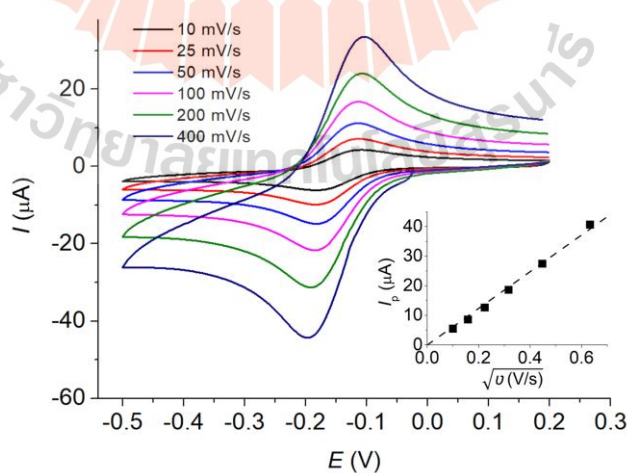


Figure 4.7: CV of 1.0 mM hexaammineruthenium(III) in 0.10 M KCl at a bare GCE at varied scan rates (10 – 400 mV s^{-1}). The inlay shows a plot of cathodic peak currents against square root of scan rates.

4.3.5 Effects of the amount of microporous carbon

The effect of the amount of microporous carbon deposited on the electrode was investigated in **Figure 4.8a – 4.8b**. At the amounts below 1.2 μg , the voltammetric peak currents increased with increasing amounts of microporous carbon. The peak current of UA oxidation then reached a maximum value at 1.2 μg of microporous carbon (**Figure 4.8a**). In the AA, DA, and UA solution mixtures (**Figure 4.8b**), the peak currents still increased with the amount of microporous carbon after 1.2 μg . However, the responses also started to level off after 1.2 μg and no longer increased proportionally with the amount dropcasted.

The electroactive surface areas of the electrodes modified with different amounts of microporous carbon were further determined using a standard outer-sphere redox probe, 1.0 mM hexaammineruthenium (III) in 0.10 M KCl to estimate the electroactive surface area of the MC/GCE electrodes immobilized with different amounts of microporous carbon. The results which are presented in **Figure 4.9** showed that the electroactive surface area increased with the amount of microporous carbon in a similar trend to that observed for the responses of AA, DA, and UA in **Figure 4.8**. However, the increase became less at large amounts of a large excess (multiple layers) of microporous carbon may hinder mass transport of the analytes to the electrode surface due to slow diffusion within the microporous structures (Ngamchuea, Tschulik, Eloul, and Compton, 2015).

The thickness and optical profile of the microporous carbon layers were next measured and presented in **Figure 4.8c – 4.8d**. The thickness of the microporous carbon layers increased with the amount drop casted. The thick layers of microporous carbon hinder mass transport of the analytes to the electrode surface due to slow diffusion within the microporous structures (Ngamchuea et al., 2015). An increase in the amount of microporous carbon also caused the capacitive background currents to be significantly large. Importantly, the peak positions of AA, DA, and UA were not significantly altered by the amount of microporous carbon. The amount of 1.2 μg of microporous carbon was thus chosen as the optimal condition for the analysis of AA, DA, and UA.

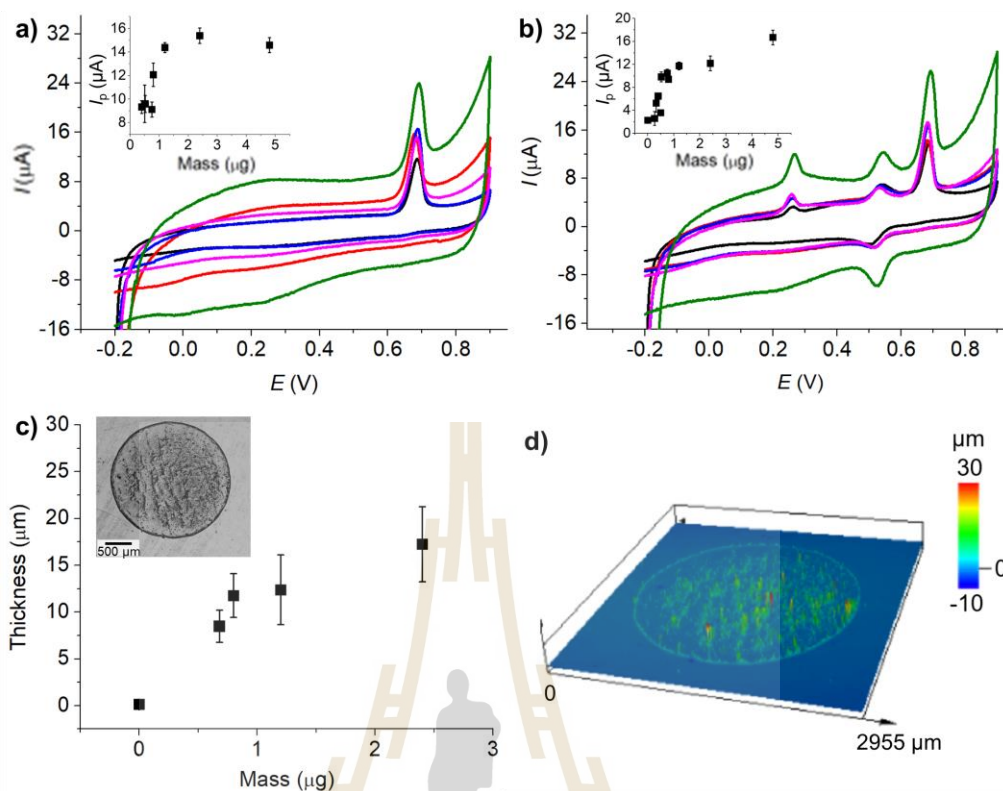


Figure 4.8 (a) CV of 100 μM UA, and (b) CV of 100 μM UA, AA, and DA at MC/GCE prepared using different amounts of microporous carbon: (black) 0.75 μg, (red) 0.8 μg, (blue) 1.2 μg, (pink) 4.4 μg, (green) 4.8 μg. Scan rate: 10 mV s⁻¹. Inlays: the plots of the anodic peak currents (I_p) vs. the amount of microporous carbon. E vs. Ag/AgCl (saturated KCl) reference electrode. (c) Average thickness of the dropcasted microporous carbon at different amounts (Inlay: confocal microscopic image of the MC (1.2 μg)/GCE surface). (d) Optical profile of the MC (1.2 μg)/GCE surface.

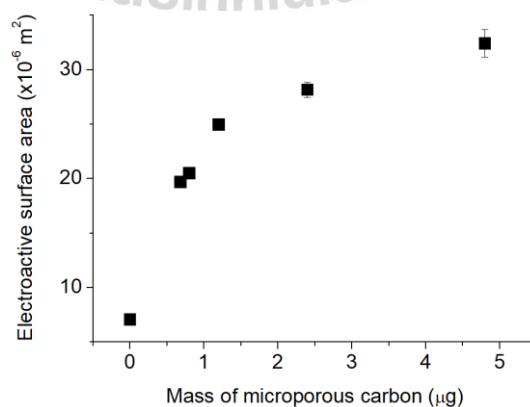


Figure 4.9 The plot of electroactive surface areas of MP/GCE electrodes against the amount of immobilized microporous carbon.

4.3.6 Calibration curve: CV

Figure 4.10 shows the cyclic voltammograms of AA, DA, and UA at different concentrations and the calibration curves in the inlays. At a bare GCE, AA can be detected with the linear range of 1 – 1,200 μM , the sensitivity of $0.007 \mu\text{A } \mu\text{M}^{-1}$, and the limit of detection (LOD) of 24.7 μM . For DA detection at a bare GCE, the linear range, sensitivity, and LOD were 1 – 140 μM , $0.014 \mu\text{A } \mu\text{M}^{-1}$, and 14.6 μM respectively. UA detection at a bare GCE had the linear range of 0 – 60 μM , the sensitivity of $0.024 \mu\text{A } \mu\text{M}^{-1}$, and the LOD of 4.6 μM .

At MC/GCE electrodes, the quantification of AA had the linear range of 1 – 1200 μM , the sensitivity of $0.018 \mu\text{A } \mu\text{M}^{-1}$, and the LOD of 5.1 μM . DA measurements at MC/GCE yielded the linear range of 1 – 140 μM , the sensitivity of $0.0465 \mu\text{A } \mu\text{M}^{-1}$, and the LOD of 1.4 μM . For UA at MC/GCE, the linear range, sensitivity, and LOD were 1 – 60 μM , $0.16 \mu\text{A } \mu\text{M}^{-1}$, and 1.8 μM , respectively. The results thus clearly demonstrated the improved sensitivities and LOD at the microporous carbon electrodes.

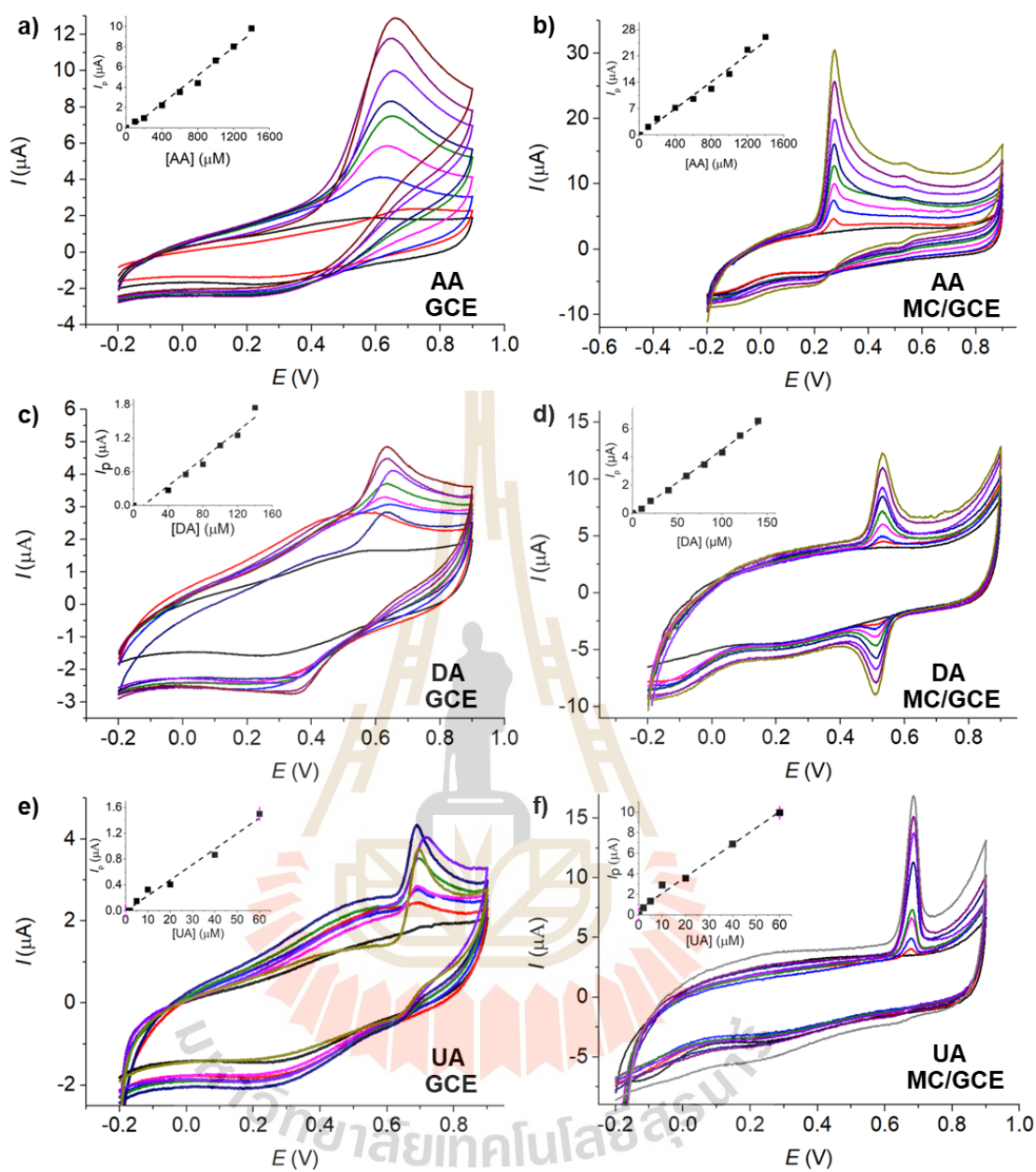


Figure 4.10 CV of varied [AA] at (a) bare GCE and (b) MC/GCE. CV of varied [DA] at (c) bare GCE and (d) MC/GCE. CV of varied [UA] at e) bare GCE and f) MC/GCE. Electrolyte: 0.10 M HCl. Scan rate: 10 mV s^{-1} .

4.4 Differential pulse voltammetry of AA, DA, and UA at MC/GCE

Next, differential pulse voltammetry (DPV) was employed to enhance the analytical performances of MC/GCE electrodes in the determination of AA, DA, and UA.

4.4.1 Peak identification

The solutions of 1,200 μM AA, 60 μM DA, 100 μM UA, and the mixture of 100 μM UA, 1,200 μM AA, and 60 μM DA in 0.10 M HCl were subjected to DPV measurements at an MC/GCE at the scan rate of 10 mV s^{-1} , the pulse amplitude of 10 mV, and the pulse width of 50 ms (Figure 4.12a). The oxidation peaks of AA, DA, and UA were identified at 0.27 V, 0.53 V, and 0.69 V by comparing the DPV responses of the mixtures with those of the individual species.

4.4.2 Effects of DPV parameters

The effect of potential pulse amplitude was investigated in the range of 10 – 200 mV at the pulse width of 50 ms (Figure 4.12b). The pulse amplitude of 10 mV gave rise to well separated anodic peak potentials of 100 μM AA, DA, and UA, and thus displayed good selectivity for the simultaneous detection of the three species. The low, flat, and reproducible baseline current at the 10 mV pulse amplitude was also preferable for electrochemical measurement and was thus chosen for the analysis.

4.4.3 Reproducibility tests

The reproducibility of the measurements at MC/GCE was next examined. The relative standard deviations (RSD, $n = 5$) of DPV peak currents of 200 μM AA, DA, and UA at MC/GCE electrodes were 0.3%, 0.8%, and 1.3%, respectively, indicating excellent reproducibility of the developed method.

4.4.4 Calibration curves: DPV

Figures 4.11c – 4.11e demonstrate the differential pulse voltammograms of varied concentrations of AA, DA, or UA in the presence of interferences from the other two species. It was found that AA, DA, and UA do not interfere with the detection of one another, indicating excellent selectivity of the developed electrochemical sensor. The linear ranges were observed to be 100 – 2,000 μM , 10 – 150 μM , and 10 – 150 μM for AA, DA, and UA, respectively (Figure 4.11) and above the maximum concentration stated, the signals no longer increased linearly with the concentration of the redox analyte as shown in Figure 4.12. The sensitivities of the measurements were $6.8 \pm 0.2 \text{ nA } \mu\text{M}^{-1}$ for AA, $261.4 \pm 3.4 \text{ nA } \mu\text{M}^{-1}$ for DA, and $93.5 \pm 2.6 \text{ nA } \mu\text{M}^{-1}$ for UA. The Limit of quantitation (LOQ) of AA, DA, and UA at MC/GCE were 70.0 μM , 0.6 μM , and 5.2 μM , respectively. The Limit of quantitation obtained in this work are significantly lower than the levels of AA, DA, and UA anticipated in human urine (AA: 458 – 9602 μM , (Brigden, Edgell, McPherson, Leadbeater, and Hoag, 1992) DA: 0.3 – 3.13 μM , (Dalirirad and Steckl, 2020) UA: 149 – 416 μM (Buledi et al., 2021)). The developed method will thus be useful for the monitoring of the three molecules in bodily fluids.



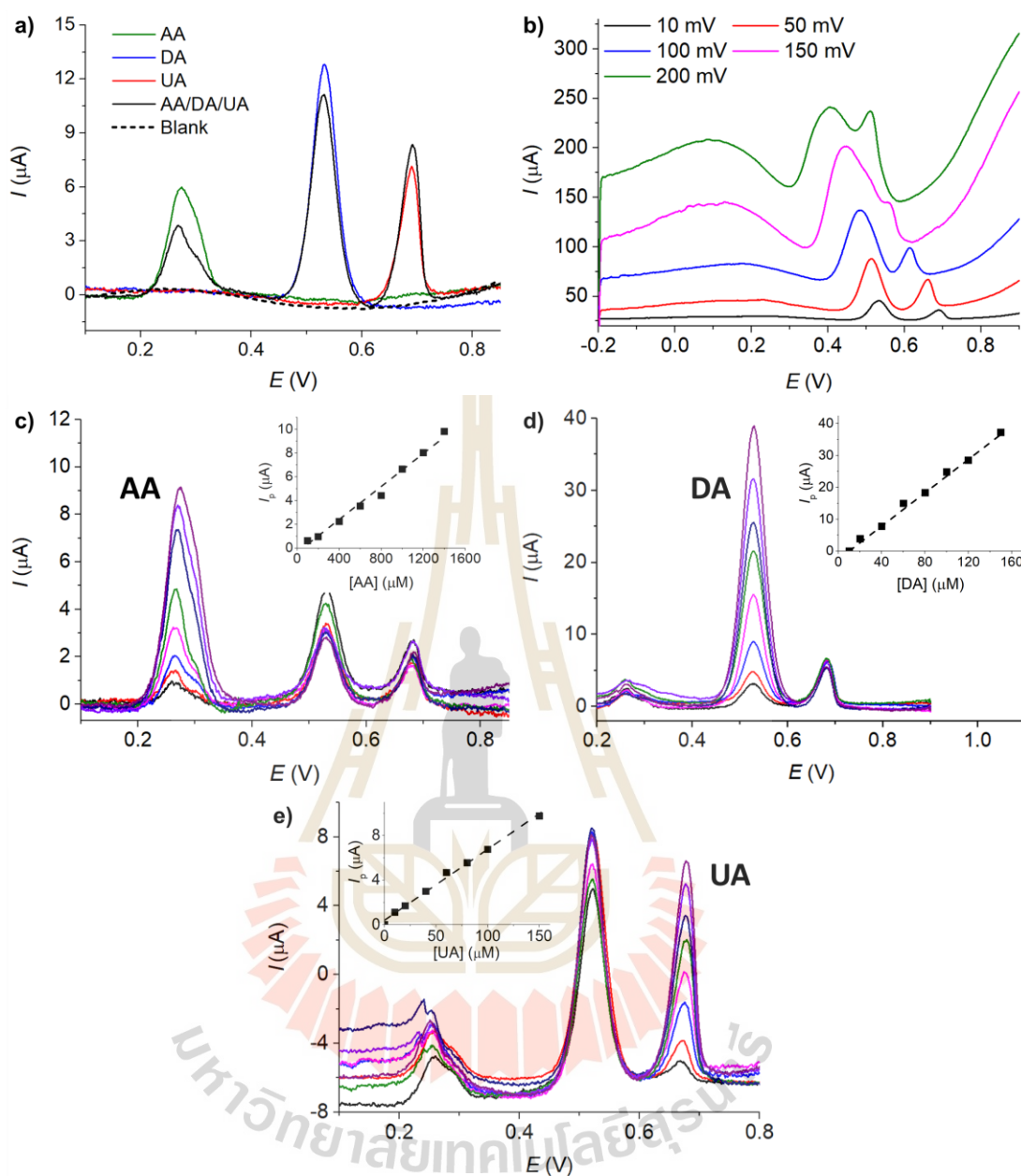


Figure 4.11 (a) DPV of AA, DA, UA, the mixture of AA, DA, and UA, and a blank electrolyte. (b) DPV of the mixture of AA, DA, and UA at different pulse amplitudes (10 – 200 mV). (c) DPV of varied [AA] in the presence of 20 μM DA and 20 μM UA. (d) DPV of varied [DA] in the presence of 500 μM AA and 50 μM UA, (e) DPV of varied [UA] in the presence of 300 μM AA and 20 μM DA. Electrolyte: 0.10 M HCl. Electrode: MC/GCE. Scan rate: 10 mV s^{-1} . Otherwise stated: pulse amplitude = 10 mV and pulse width = 50 ms. E vs. Ag/AgCl (saturated KCl) reference electrode.

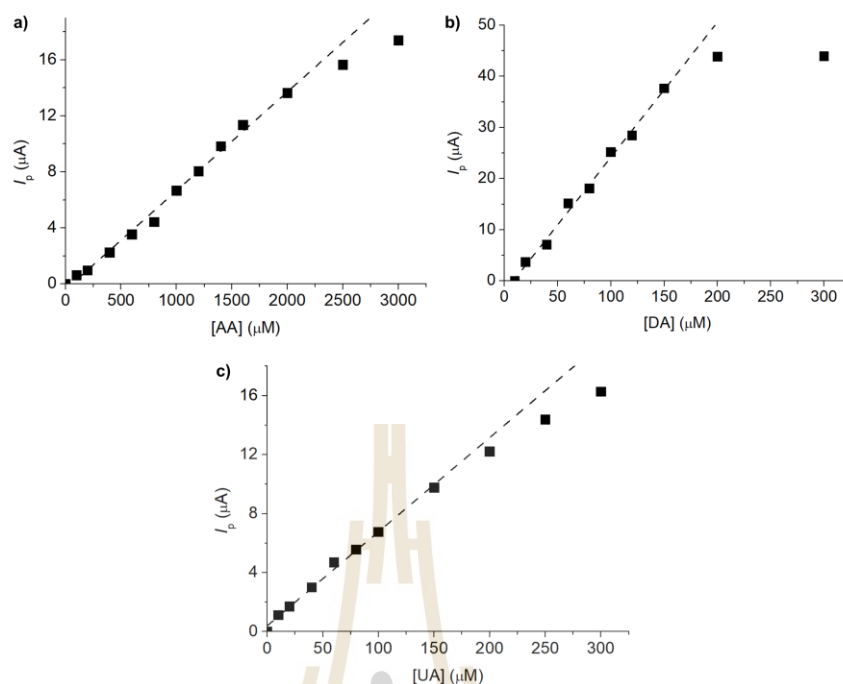


Figure 4.12 The calibration plots of DPV peak currents against the concentrations of (a) AA, (b) DA, and (c) UA. Working electrode: MC/GCE. Electrolyte: 0.10 M HCl. Scan rate: 10 mV s^{-1} .

4.5 Validation in synthetic urine

Normal urine contains various contaminants and impurities that may interfere with the electrochemical response. The composition of urine changes according to gender, age, race, food intake, presence of medication and exercise. It changes throughout the day in the same individual according to the requirements for normal bodily functions. Another difficulty is the collection and storage problems, which have been emphasised in many studies (Sarigul, Korkmaz, and Kurultak, 2019). So that in this work, the use of synthetic urine, which contains a number of metabolites and electrolytes in the same concentration ranges as expected from a real urine sample, is sufficient to validate the applicability of the sensor.

The developed sensor was next validated in synthetic urine sample prepared according to Jiang., (Jiang et al., 2016) and using differential pulse voltammetry (DPV). **Figure 4.13** compares the differential pulse voltammograms of 2,500 μM AA, 100 μM DA, and 200 μM UA in standard 0.10 M HCl electrolyte vs. in synthetic urine sample in the presence of 0.10 M HCl. This sensor demonstrated excellent separation

between the oxidation peaks of DA, UA, and AA. Synthetic urine does not significantly interfere with the potential positions of UA, AA, and DA, and no significant changes in the AA and DA signals were observed. However, it does interfere with the electrochemical detection of UA by 37.5%. The current responses decreased, which was probably caused by the obstruction of UA oxidation on the MC/GCE sensor by interfering ions in synthetic urine, which can significantly interfere with UA detection.

Next, the %recovery was evaluated. The concentrations of 500 μM AA, 2.0 μM DA, and 200 μM UA were spiked into synthetic urine and subjected to DPV measurements at MC/GCE under the optimized conditions (1.2 μg MC, scan rate: 10 mV s^{-1} , pulse amplitude 10 mV, pulse width 50 ms). The employed concentrations were chosen to be within the normal levels of AA, DA, and UA found in human urine (AA: 458 – 9602 μM , (Brigden et al., 1992) DA: 0.3 – 3.13 μM , (Dalirirad and Steckl., 2020) UA: 149 – 416 μM (Buledi et al., 2021)). The percentage recoveries determined by standard addition methods were 96%, 102%, and 101% for AA, DA, and UA, respectively, suggesting high accuracy of the method and excellent tolerance to possible interferences presented in the synthetic urine sample.

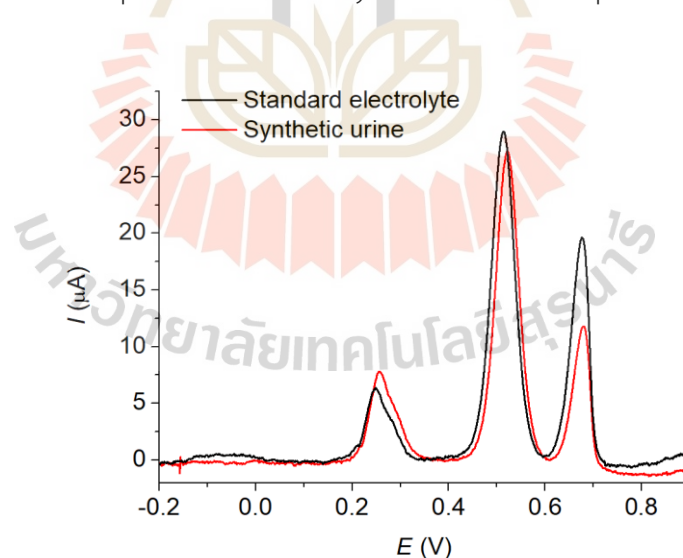


Figure 4.13 DPV at MC/GCE electrode in the mixture of 2,500 μM AA, 100 μM DA, and 200 μM UA in 0.10 M HCl standard electrolyte vs. in synthetic urine sample in the presence of 0.10 M HCl at the pulse amplitude of 10 mV, the pulse width of 50 ms, and the scan rate of 10 mV s^{-1} . E vs. Ag/AgCl (saturated KCl) reference electrode.

4.6 Application of the developed sensor in the evaluation of peroxide scavenging activity of uric Acid

As uric acid is an important antioxidant in human plasma, we next applied our developed sensor in the investigation of the scavenging properties of uric acid towards reactive oxygen species (ROS) by using hydrogen peroxide (H_2O_2) as a model system (Guelcin et al., 2008). The solutions of 100 μM or 200 μM UA were mixed with various concentrations of H_2O_2 (0.0 – 50.0 mM H_2O_2) and kept in a dark place at room temperature for 24 hours. UA concentrations were then measured electrochemically by the developed method.

The % of UA consumed in the reaction with H_2O_2 was calculated by equation 4.4:

$$\% \text{ UA consumed} = [(I_{p,\text{control}} - I_{p,\text{sample}}) / I_{p,\text{control}}] \times 100 \quad (4.4),$$

where $I_{p,\text{control}}$ and $I_{p,\text{sample}}$ are the peak currents of UA in the absence and presence of H_2O_2 , respectively.

Gülçin (Guelcin et al., 2008) suggested that the ‘% UA consumed’ parameter can be used in the estimation of peroxide scavenging activity of UA. **Figure 4.14** showed that higher percentages of UA were consumed at higher H_2O_2 concentrations. Higher percentages of UA were consumed when the initial concentration of UA was lower. When 100 μM UA was used, the peroxide scavenging activity approached the limiting value of $46.7 \pm 0.8\%$ at the $[\text{H}_2\text{O}_2]/[\text{UA}]$ ratio of ca. 350 - fold, close to the value reported by Gülçin et al., in spectrophotometric measurements ($41.1 \pm 2.9\%$) (Guelcin et al., 2008). With the developed simple electrochemical method, it was thus possible to determine the peroxide scavenging activity of UA. The advantage of the electrochemical method over the previously used spectrophotometric technique (Guelcin et al., 2008) is that there is no interference between the responses of UA and H_2O_2 as shown in **Figure 4.15**.

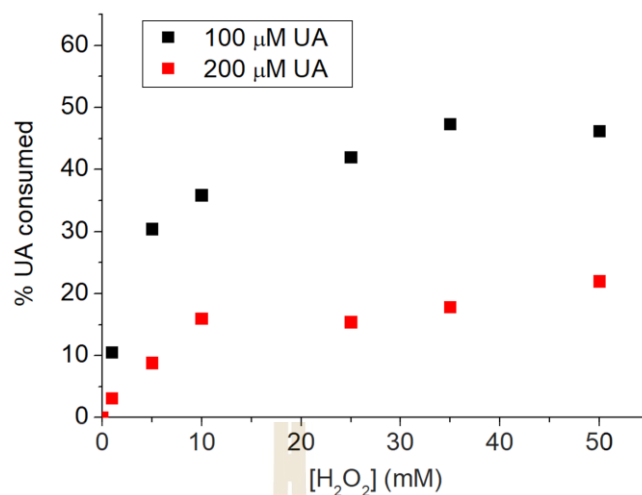


Figure 4.14 % UA consumed after (black) 100 μM UA or (red) 100 μM UA were incubated with 0.0 – 50.0 mM H_2O_2 for 24 hours.

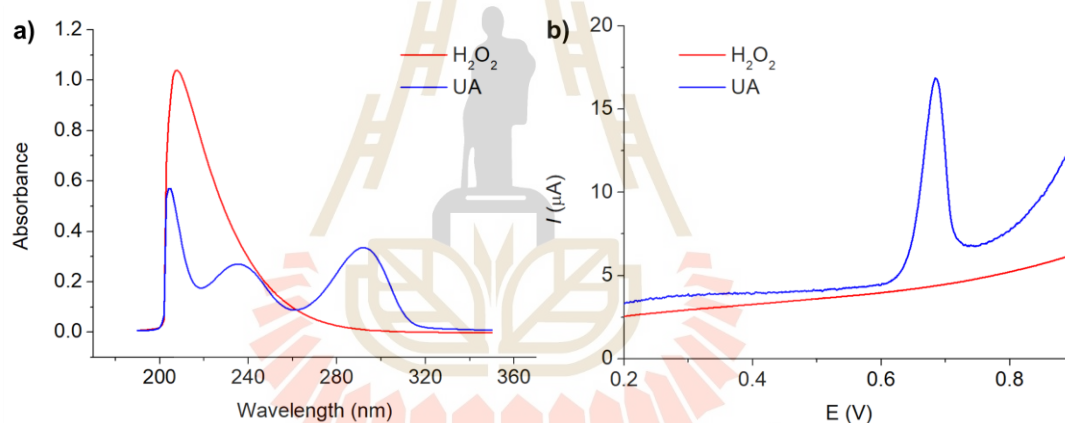


Figure 4.15 (a) UV-visible spectra and (b) voltammograms of (red) 30 mM H_2O_2 and (blue) 100 μM uric acid (UA).

4.7 Conclusion

The electrochemical behaviors of AA, DA, and UA were investigated at various electrode materials including Cu_2O , CuO , carbon nanotube, and microporous carbon. The superior sensitivity and selectivity of microporous carbon in the simultaneous analysis of AA, DA, and UA were clearly demonstrated. The highly porous structure of the carbon material greatly increased the electroactive surface area, enhancing the sensitivity of the measurement. The selectivity of the electrochemical detection was significantly improved by the microporosity and the presence of various surface

functional groups on microporous carbon. The synergistic effect of microporous carbon enables it to be a suitable electrode material for the analysis of AA, DA, and UA, better than its alternatives such as carbon nanotubes and copper oxides. Excellent sensitivities and limits of detection with 100% recoveries were achieved. The sensor was capable of detecting AA, DA, and UA simultaneously and selectively in the presence of various interferences in synthetic urine. Furthermore, we have shown that the developed electrochemical sensor can be applied in the evaluation of peroxide scavenging activity using UA as a paradigmatic example. Overall, the developed sensor shows strong potentials for applications which require fast measurements of AA, DA, and/or UA in biological fluids.

4.8 References

- Ames, B. N., Cathcart, R., Schwiers, E., and Hochstein, P. (1981). Uric acid provides an antioxidant defense in humans against oxidant- and radical-caused aging and cancer: a hypothesis. *Proc. Natl. Acad. Sci. U. S. A.* 78(11), 6858-6862.
- Amić, A., Marković, Z., Dimitrić Marković, J. M., Lučić, B., Stepanić, V., and Amić, D. (2016). The $2\text{H}^+/2\text{e}^-$ free radical scavenging mechanisms of uric acid: thermodynamics of NH bond cleavage. *Comput. Theor. Chem.*, 1077, 2-10.
- Aparna, T. K., Sivasubramanian, R., and Dar, M. A. (2018). One-pot synthesis of Au-Cu₂O /rGO nanocomposite based electrochemical sensor for selective and simultaneous detection of dopamine and uric acid. *J. Alloys Compd.*, 741, 1130-1141.
- Atta, N. F., Galal, A., Ali, S. M., and El-Said, D. M. (2014). Improved host-guest electrochemical sensing of dopamine in the presence of ascorbic and uric acids in a β -cyclodextrin/Nafion®/polymer nanocomposite. *Anal. Methods*, 6(15), 5962-5971.
- Benn, C. L., Dua, P., Gurrell, R., Loudon, P., Pike, A., Storer, R. I., and Vangjeli, C. (2018). Physiology of hyperuricemia and urate-lowering treatments. *Front. Med.*, 160.
- Brainina, K. Z., and Kazakov, Y. E. (2020). Electrochemical hybrid methods and sensors for antioxidant/oxidant activity monitoring and their use as a diagnostic tool of oxidative stress: future perspectives and challenges. *Chemosensors*, 8(4).

- Brigden, M. L., Edgell, D., McPherson, M., Leadbeater, A., and Hoag, G. (1992). High incidence of significant urinary ascorbic acid concentrations in a west coast population--implications for routine urinalysis. *Clin. Chem.*, *38*(3), 426-431.
- Buledi, J. A., Ameen, S., Memon, S. A., Fatima, A., Solangi, A. R., Mallah, A., Karimi, F., Malakmohammadi, S., Agarwal, S., and Gupta, V. K. (2021). An improved non-enzymatic electrochemical sensor amplified with CuO nanostructures for sensitive determination of uric acid. *Open Chem.*, *19*(1), 481-491.
- Cai, H.-L., Li, H.-D., Yan, X.-Z., Sun, B., Zhang, Q., Yan, M., Zhang, W.-Y., Jiang, P., Zhu, R.-H., Liu, Y.-P., Fang, P.-F., Xu, P., Yuan, Y.-H., Zhang, X.-H., Hu, L., Yang, W., and Ye, H.-S. (2012). Metabolomic analysis of biochemical changes in the plasma and urine of first-episode neuroleptic-naive schizophrenia patients after treatment with risperidone. *J. Proteome Res.*, *11*(8), 4338-4350.
- Chaisiwamongkhol, K., Ngamchuea, K., Batchelor-McAuley, C., and Compton, R. G. (2016). Electrochemical detection and quantification of gingerol species in ginger (*Zingiber officinale*) using multiwalled carbon nanotube modified electrodes. *Analyst*, *141*(22), 6321-6328.
- Chen, S., Zheng, H., Wang, J., Hou, J., He, Q., Liu, H., Xiong, C., Kong, X., and Nie, Z. (2013). Carbon nanodots as a matrix for the analysis of low-molecular-weight molecules in both positive-and negative-ion matrix-assisted laser desorption/ionization time-of-flight mass spectrometry and quantification of glucose and uric acid in real samples. *Anal. Chem*, *85*(14), 6646-6652.
- Compton, R. G., and Banks, C. E. (2018). *Understanding voltammetry*: World Scientific.
- Dalirirad, S., and Steckl, A. J. (2020). Lateral flow assay using aptamer-based sensing for on-site detection of dopamine in urine. *Anal. Biochem.*, *596*, 113637.
- De Andrade, K. Q., Moura, F. A., Dos Santos, J. M., De Araújo, O. R. P., de Farias Santos, J. C., and Goulart, M. O. F. (2015). Oxidative stress and inflammation in hepatic diseases: therapeutic possibilities of N-acetylcysteine. *Int. J. Mol. Sci.*, *16*(12), 30269-30308.
- Dollimore, D., and Heal, G. (1964). An improved method for the calculation of pore size distribution from adsorption data. *J. Appl. Chem.*, *14*(3), 109-114.

- Dryhurst, G. (1972). Electrochemical oxidation of uric acid and xanthine at the pyrolytic graphite electrode mechanistic interpretation of electrochemistry. *J. Electrochem. Soc.*, 119(12), 1659-1664.
- Du, J., Cullen, J. J., and Buettner, G. R. (2012). Ascorbic acid: chemistry, biology and the treatment of cancer. *Biochim. Biophys. Acta - Rev. Cancer*, 1826(2), 443-457.
- Ensafi, A. A., Taei, M., and Khayamian, T. (2009). A differential pulse voltammetric method for simultaneous determination of ascorbic acid, dopamine, and uric acid using poly (3-(5-chloro-2-hydroxyphenylazo)-4, 5-dihydroxynaphthalene-2, 7-disulfonic acid) film modified glassy carbon electrode. *J. Electroanal. Chem.*, 633(1), 212-220.
- Farahi, A., Hammani, H., Kajai, A., Lahrich, S., Bakasse, M., and El Mhammedi, M. A. (2019). Electro-catalytic detection of dopamine at carbon paste electrode modified with activated carbon: analytical application in blood samples. *Intern. J. environ. anal. chem.*, 100(3), 295-310.
- Govindasamy, M., Chen, S.-M., Mani, V., Sathiyar, A., Merlin, J. P., Al-Hemaid, F. M. A., and Ali, M. A. (2016). Simultaneous determination of dopamine and uric acid in the presence of high ascorbic acid concentration using cetyltrimethylammonium bromide-polyaniline/activated charcoal composite. *RSC Advances*, 6(102), 100605-100613.
- Guelcin, I., Oktay, M., Koeksal, E., Serbetci, H., Beydemir, S., and Kuefrevioglu, O. (2008). Antioxidant and radical scavenging activities of uric acid. *Asian J. Chem.*, 20(3).
- Guidelli, R., Compton, R. G., Feliu, J. M., Gileadi, E., Lipkowsky, J., Schmickler, W., and Trasatti, S. (2014). Defining the transfer coefficient in electrochemistry: An assessment (IUPAC Technical Report). *Pure Appl. Chem.*, 86(2), 245-258.
- Gupta, R., and Ganesan, V. (2015). Gold nanoparticles impregnated mesoporous silica spheres for simultaneous and selective determination of uric acid and ascorbic acid. *Sens. Actuators B: Chem.*, 219, 139-145.
- Hesas, R. H., Arami-Niya, A., Daud, W. M. A. W., and Sahu, J. (2013). Preparation and characterization of activated carbon from apple waste by microwave-assisted

- phosphoric acid activation: application in methylene blue adsorption. *Bioresources*, 8(2), 2950-2966.
- Jeong, H., and Jeon, S. (2008). Determination of dopamine in the presence of ascorbic acid by nafion and single-walled carbon nanotube film modified on carbon fiber microelectrode. *Sensors*, 8(11), 6924-6935.
- Jiang, G., Wang, J., Yang, Y., Zhang, G., Liu, Y., Lin, H., Zhang, G., Li, Y., and Fan, X. (2016). Fluorescent turn-on sensing of bacterial lipopolysaccharide in artificial urine sample with sensitivity down to nanomolar by tetraphenylethylene based aggregation induced emission molecule. *Biosens. Bioelectron.*, 85, 62-67.
- Jindal, K., Tomar, M., and Gupta, V. (2012). CuO thin film based uric acid biosensor with enhanced response characteristics. *Biosens. Bioelectron.*, 38(1), 11-18.
- Kaewket, K., Maensiri, S., and Ngamchuea, K. (2020). Adsorptive stripping voltammetry at microporous carbon: Determination and adsorption characteristics of environmental contaminants. *Colloids Interface Sci. Commun.*, 38, 100310.
- Kameda, T., Horikoshi, K., Kumagai, S., Saito, Y., and Yoshioka, T. (2020). Adsorption of urea, creatinine, and uric acid from three solution types using spherical activated carbon and its recyclability. *Chin. J. Chem. Eng.*, 28(12), 2993-3001.
- Kaya, M., Şahin, Ö., and Saka, C. (2018). Preparation and TG/DTG, FT-IR, SEM, BET surface area, iodine number and methylene blue number analysis of activated carbon from pistachio shells by chemical activation. *Int. J. Chem. React. Eng.*, 16(2).
- Khoshnevisan, K., Maleki, H., Honarvarfard, E., Baharifar, H., Gholami, M., Faridbod, F., Larijani, B., Majidi, R. F., and Khorramizadeh, M. R. (2019). Nanomaterial based electrochemical sensing of the biomarker serotonin: a comprehensive review. *Mikrochim. Acta.*, 186(1), 1-21.
- Krishnamoorthy, K., Sudha, V., Senthil Kumar, S. M., and Thangamuthu, R. (2018). Simultaneous determination of dopamine and uric acid using copper oxide nano-rice modified electrode. *J. Alloys Compd.*, 748, 338-347.
- Lakard, S., Pavel, I. A., and Lakard, B. (2021). Electrochemical biosensing of dopamine neurotransmitter: A review. *Biosensors (Basel)*, 11(6).

- Lawal, A. T., Bolarinwa, H. S., Animasahun, L. O., Adeoye, M. D., Abdulsalami, I. O., and Alabi, K. A. (2019). Progress in Carbon nanotube-based electrochemical biosensors – A review. *FUJNAS*, 8(2).
- Li, D., Lin, C., Batchelor-McAuley, C., Chen, L., and Compton, R. G. (2018). Tafel analysis in practice. *J. Electroanal. Chem.*, 826, 117-124.
- Li, M., Guo, W., Li, H., Dai, W., and Yang, B. (2014). Electrochemical biosensor based on one-dimensional MgO nanostructures for the simultaneous determination of ascorbic acid, dopamine, and uric acid. *Sens. Actuators B: Chem.*, 204, 629-636.
- Lisowska-Myjak, B. (2010). Serum and urinary biomarkers of acute kidney injury. *Blood Purif.*, 29(4), 357-365.
- Liu, C., Liang, X., Liu, X., Wang, Q., Zhan, L., Zhang, R., Qiao, W., and Ling, L. (2008). Surface modification of pitch-based spherical activated carbon by CVD of NH₃ to improve its adsorption to uric acid. *Appl. Surf. Sci.*, 254(21), 6701-6705.
- Liu, J., and Cao, Y. (2021). An electrochemical sensor based on an anti-fouling membrane for the determination of histamine in fish samples. *Anal. Methods*, 13(5), 685-694.
- López-Suárez, A., Elvira-González, J., Bascuñana-Quirell, A., Rosal-Obrador, J., Michán-Doña, A., Escribano-Serrano, J., and Benítez-Rodríguez, E. (2006). Concentraciones séricas de uratos y excreción urinaria de ácido úrico en individuos con síndrome metabólico. *Med. Clin.*, 126(9), 321-324.
- Maiuolo, J., Oppedisano, F., Gratteri, S., Muscoli, C., and Mollace, V. (2016). Regulation of uric acid metabolism and excretion. *Int. J. Cardiol.*, 213, 8-14.
- Manocha, S. M. (2003). Porous carbons. *Sadhana*, 28(1-2), 335-348.
- Marahel, F., Ghaedi, M., and Ansari, A. (2015). Zinc oxide nanoparticles loaded on activated carbon and its application for adsorption removal of uric acid. *Syn. React. Inorg. Metaorg. Nanometal. Chem.*, 45(9), 1387-1395.
- Martillo, M. A., Nazzal, L., and Crittenden, D. B. (2014). The crystallization of monosodium urate. *Curr. Rheumatol. Rep.*, 16(2), 400.
- Mei, L.-P., Feng, J.-J., Wu, L., Chen, J.-R., Shen, L., Xie, Y., and Wang, A.-J. (2016). A glassy carbon electrode modified with porous Cu₂O nanospheres on reduced

- graphene oxide support for simultaneous sensing of uric acid and dopamine with high selectivity over ascorbic acid. *Mikrochim. Acta*, 183(6), 2039-2046.
- Mirrahimov, A. E., Voore, P., Khan, M., and Ali, A. M. (2015). Tumor lysis syndrome: A clinical review. *World J. Crit. Care Med.*, 4(2), 130-138.
- Mojoudi, N., Mirghaffari, N., Soleimani, M., Shariatmadari, H., Belver, C., and Bedia, J. (2019). Phenol adsorption on high microporous activated carbons prepared from oily sludge: equilibrium, kinetic and thermodynamic studies. *Sci. Rep.*, 9(1), 19352.
- Momtazan, F., Vafaei, A., Ghaedi, M., Ghaedi, A. M., Emadzadeh, D., Lau, W.-J., and Baneshi, M. M. (2018). Application of copper sulfide nanoparticles loaded activated carbon for simultaneous adsorption of ternary dyes: Response surface methodology. *Korean J. Chem. Eng.*, 35(5), 1108-1118.
- Moretti, M., Fraga, D. B., and Rodrigues, A. L. S. (2017). Preventive and therapeutic potential of ascorbic acid in neurodegenerative diseases. *CNS neurosci. ther.*, 23(12), 921-929.
- Naveen, M. H., Gurudatt, N. G., and Shim, Y.-B. (2017). Applications of conducting polymer composites to electrochemical sensors: A review. *Appl. Mater. Today*, 9, 419-433.
- Ngamchuea, K., Batchelor-McAuley, C., and Compton, R. G. (2018). Understanding electroanalytical measurements in authentic human saliva leading to the detection of salivary uric acid. *Sens. Actuators B: Chem.*, 262, 404-410.
- Ngamchuea, K., Chaisiwamongkhol, K., Batchelor-McAuley, C., and Compton, R. G. (2018). Chemical analysis in saliva and the search for salivary biomarkers—a tutorial review. *Analyst*, 143(1), 81-99.
- Ngamchuea, K., Eloul, S., Tschulik, K., and Compton, R. G. (2015). Advancing from rules of thumb: quantifying the effects of small density changes in mass transport to electrodes. Understanding Natural Convection. *Anal. Chem.*, 87(14), 7226-7234.
- Ngamchuea, K., Lin, C., Batchelor-McAuley, C., and Compton, R. G. (2017). Supported microwires for electroanalysis: sensitive amperometric detection of reduced glutathione. *Anal. Chem.*, 89(6), 3780-3786.

- Ngamchuea, K., Tharat, B., Hirunsit, P., and Suthirakun, S. (2020). Electrochemical oxidation of resorcinol: mechanistic insights from experimental and computational studies. *RSC advances*, 10(47), 28454-28463.
- Ngamchuea, K., Tschulik, K., Eloul, S., and Compton, R. G. (2015). In situ detection of particle aggregation on electrode surfaces. *Chemphyschem*, 16(11), 2338-2347.
- Ngamchuea, K., Wannapaiboon, S., Nongkhunsan, P., Hirunsit, P., and Fongkaew, I. (2022). Structural and electrochemical analysis of copper-creatinine complexes: application in creatinine detection. *J. Electrochem. Soc.*, 169(2), 020567.
- Nimse, S. B., and Pal, D. (2015). Free radicals, natural antioxidants, and their reaction mechanisms. *RSC Advances*, 5(35), 27986-28006.
- Ning, J., He, Q., Luo, X., Wang, M., Liu, D., Wang, J., Li, G., and Liu, J. (2018). Determination of uric acid in co-presence of dopamine and ascorbic acid using cuprous oxide nanoparticle-functionalized graphene decorated glassy carbon electrode. *Catalysts*, 8(10).
- Noroozifar, M., Khorasani-Motlagh, M., Jahromi, F. Z., and Rostami, S. (2013). Sensitive and selective determination of uric acid in real samples by modified glassy carbon electrode with holmium fluoride nanoparticles/multi-walled carbon nanotube as a new biosensor. *Sens. Actuators B: Chem.*, 188, 65-72.
- Öztürk Doğan, H., Kurt Urhan, B., Çepni, E., and Eryiğit, M. (2019). Simultaneous electrochemical detection of ascorbic acid and dopamine on Cu₂O/CuO/electrochemically reduced graphene oxide (Cu_xO/ERGO)-nanocomposite-modified electrode. *Microchem. J.*, 150.
- Pandikumar, A., How, G. T. S., See, T. P., Omar, F. S., Jayabal, S., Kamali, K. Z., Yusoff, N., Jamil, A., Ramaraj, R., John, S. A., Lim, H. N., and Huang, N. M. (2014). Graphene and its nanocomposite material based electrochemical sensor platform for dopamine. *Rsc Advances*, 4(108), 63296-63323.
- Qi, S., Zhao, B., Tang, H., and Jiang, X. (2015). Determination of ascorbic acid, dopamine, and uric acid by a novel electrochemical sensor based on pristine graphene. *Electrochim. Acta*, 161, 395-402.

- Sajid, M., Nazal, M. K., Mansha, M., Alsharaa, A., Jillani, S. M. S., and Basheer, C. (2016). Chemically modified electrodes for electrochemical detection of dopamine in the presence of uric acid and ascorbic acid: A review. *TrAC, Trends Anal. Chem.*, 76, 15-29.
- Şavk, A., Aydın, H., Cellat, K., and Şen, F. (2020). A novel high performance non-enzymatic electrochemical glucose biosensor based on activated carbon-supported Pt-Ni nanocomposite. *J. Mol. Liq.*, 300.
- Savk, A., Ozdil, B., Demirkan, B., Nas, M. S., Calimli, M. H., Alma, M. H., Inamuddin, Asiri, A. M., and Sen, F. (2019). Multiwalled carbon nanotube-based nanosensor for ultrasensitive detection of uric acid, dopamine, and ascorbic acid. *Mater. Sci. Eng. C. Mater. Biol. Appl.*, 99, 248-254.
- Sarigul, N., Korkmaz, F., and Kurultak, İ. (2019). A new artificial urine protocol to better imitate human urine. *Scientific Reports*, 9(1), 20159.
- Shad, Z., Arsalan, A., Barto, R., Khan, M. F., and Ahmed, I. (2011). Physicochemical, biochemical and antioxidant properties of ascorbic acid. *Baqai j. health sci.*, 14(2), 33-40.
- Sheikh-Mohseni, M. A., and Pirsai, S. (2016). Nanostructured conducting polymer/copper oxide as a modifier for fabrication of L-DOPA and uric acid electrochemical sensor. *Electroanalysis*, 28(9), 2075-2080.
- Sheng, Z.-H., Zheng, X.-Q., Xu, J.-Y., Bao, W.-J., Wang, F.-B., and Xia, X.-H. (2012). Electrochemical sensor based on nitrogen doped graphene: simultaneous determination of ascorbic acid, dopamine and uric acid. *Biosens. Bioelectron.*, 34(1), 125-131.
- Shu, J., Cheng, S., Xia, H., Zhang, L., Peng, J., Li, C., and Zhang, S. (2017). Copper loaded on activated carbon as an efficient adsorbent for removal of methylene blue. *RSC advances*, 7(24), 14395-14405.
- Sohouli, E., Khosrowshahi, E. M., Radi, P., Naghian, E., Rahimi-Nasrabadi, M., and Ahmadi, F. (2020). Electrochemical sensor based on modified methylcellulose by graphene oxide and Fe₃O₄ nanoparticles: Application in the analysis of uric acid content in urine. *J. Electroanal. Chem.*, 877, 114503.

- Song, Y., Gong, C., Su, D., Shen, Y., Song, Y., and Wang, L. (2016). A novel ascorbic acid electrochemical sensor based on spherical MOF-5 arrayed on a three-dimensional porous carbon electrode. *Anal. Methods.*, 8(10), 2290-2296.
- Sorice, A., Guerriero, E., Capone, F., Colonna, G., Castello, G., and Costantini, S. (2014). Ascorbic acid: its role in immune system and chronic inflammation diseases. *Mini-Rev. Med. Chem.*, 14(5), 444-452.
- Sun, C. L., Chang, C. T., Lee, H. H., Zhou, J., Wang, J., Sham, T. K., and Pong, W. F. (2011). Microwave-assisted synthesis of a core-shell MWCNT/GONR heterostructure for the electrochemical detection of ascorbic acid, dopamine, and uric acid. *ACS Nano*, 5(10), 7788-7795.
- Sun, C. L., Lee, H. H., Yang, J. M., and Wu, C. C. (2011). The simultaneous electrochemical detection of ascorbic acid, dopamine, and uric acid using graphene/size-selected Pt nanocomposites. *Biosens. Bioelectron.*, 26(8), 3450-3455.
- Thanh, T. S., Qui, P. T., Tu, N. T. T., Toan, T. T. T., Hoa, T. T. B., Son, L. V. T., Nguyen. D. M., Tuyen, T. N., and Khieu, D. Q. (2021). Electrochemical determination of uric acid in urine by using zeolite imidazolite framework-11 modified electrode. *J. Nanomater.*, 2021.
- Tukimin, N., Abdullah, J., and Sulaiman, Y. (2018). Electrodeposition of poly(3,4-ethylenedioxythiophene)/reduced graphene oxide/manganese dioxide for simultaneous detection of uric acid, dopamine and ascorbic acid. *J. Electroanal. Chem.*, 820, 74-81.
- Wang, C., Du, J., Wang, H., Zou, C. e., Jiang, F., Yang, P., and Du, Y. (2014). A facile electrochemical sensor based on reduced graphene oxide and Au nanoplates modified glassy carbon electrode for simultaneous detection of ascorbic acid, dopamine and uric acid. *Sens. Actuators B: Chem.*, 204, 302-309.
- Wang, C., Li, J., Shi, K., Wang, Q., Zhao, X., Xiong, Z., Zou, X., and Wang, Y. (2016). Graphene coated by polydopamine/multi-walled carbon nanotubes modified electrode for highly selective detection of dopamine and uric acid in the presence of ascorbic acid. *J. Electroanal. Chem.*, 770, 56-61.

- Wang, H., Ren, F., Wang, C., Yang, B., Bin, D., Zhang, K., and Du, Y. (2014). Simultaneous determination of dopamine, uric acid and ascorbic acid using a glassy carbon electrode modified with reduced graphene oxide. *RSC Advances*, 4(51), 26895-26901.
- Waryani, B., Tahira, A., Ameen, S., Willande, M., Abbasi, A. R., and Ibupoto, Z. H. (2020). The enzyme free uric acid Sensor based on iron doped CuO nanostructures for the determination of uric acid from commercial seafood. *J. Electron. Mater.*, 49(10), 6123-6129.
- Xia, C., and Ning, W. (2011). A novel bio-electrochemical ascorbic acid sensor modified with $\text{Cu}_4(\text{OH})_6\text{SO}_4$ nanorods. *Analyst*, 136(2), 288-292.
- Xu, M., Li, D., Yan, Y., Guo, T., Pang, H., and Xue, H. (2017). Porous high specific surface area-activated carbon with co-doping N, S and P for high-performance supercapacitors. *RSC advances*, 7(69), 43780-43788.
- Xu, Z., Zhang, M.-q., Zou, H.-q., Liu, J.-s., Wang, D.-z., Wang, J., and Wang, L.-d. (2019). Non-enzymatic electrochemical detection of uric acid with electrodeposited Nafion film. *J. Electroanal. Chem.*, 841, 129-134.
- Yan, Q., Zhi, N., Yang, L., Xu, G., Feng, Q., Zhang, Q., and Sun, S. (2020). A highly sensitive uric acid electrochemical biosensor based on a nano-cube cuprous oxide/ferrocene/uricase modified glassy carbon electrode. *Sci. Rep.*, 10(1), 10607.
- Yang, S., Li, G., Yin, Y., Yang, R., Li, J., and Qu, L. (2013). Nano-sized copper oxide/multi-wall carbon nanotube/Nafion modified electrode for sensitive detection of dopamine. *J. Electroanal. Chem.*, 703, 45-51.
- Ye, N., Gao, T., and Li, J. (2014). Hollow fiber-supported graphene oxide molecularly imprinted polymers for the determination of dopamine using HPLC-PDA. *Anal. Methods*, 6(18), 7518-7524.
- Zhang, S., Xu, F., Liu, Z. Q., Chen, Y. S., and Luo, Y. L. (2019). Novel electrochemical sensors from poly[N-(ferrocenyl formacyl) pyrrole]@multi-walled carbon nanotubes nanocomposites for simultaneous determination of ascorbic acid, dopamine and uric acid. *Nanotechnology*, 31(8), 085503.

- Zhang, W., Yuan, R., Chai, Y.-Q., Zhang, Y., and Chen, S.-H. (2012). A simple strategy based on lanthanum–multiwalled carbon nanotube nanocomposites for simultaneous determination of ascorbic acid, dopamine, uric acid and nitrite. *Sens. Actuators B: Chem.*, 166-167, 601-607.
- Zhao, D., Yu, G., Tian, K., and Xu, C. (2016). A highly sensitive and stable electrochemical sensor for simultaneous detection towards ascorbic acid, dopamine, and uric acid based on the hierarchical nanoporous PtTi alloy. *Biosens. Bioelectron.*, 82, 119-126.
- Zhao, Y., Cho, C.-W., Cui, L., Wei, W., Cai, J., Wu, G., and Yun, Y.-S. (2019). Adsorptive removal of endocrine-disrupting compounds and a pharmaceutical using activated charcoal from aqueous solution: kinetics, equilibrium, and mechanism studies. *Environ. Sci. Pollut. Res.*, 26(33), 33897-33905.
- Zheng, P., Chen, J.-j., Huang, T., Wang, M.-j., Wang, Y., Dong, M.-x., Huang, Y-j., Zhou, L-k., and Xie, P. (2013). A novel urinary metabolite signature for diagnosing major depressive disorder. *J. Proteome Res.*, 12(12), 5904-5911.

CHAPTER V
CATALYSIS OF THE REDUCTION OF OXYGEN BY IRON (III)
PORPHYRIN (HEMIN) AT GLASSY CARBON ELECTRODE
IN HIGH SALT CONCENTRATION

5. Results and discussion

5.1 Characterization of hemin

Hemin exists as a mixture of dimeric species in aqueous solution, including π - π dimers and μ -oxo dimers, but not higher aggregates (Asher, de Villiers, and Egan, 2009; de Villiers et al., 2007). The UV-vis spectra of a 50.0 – 175.0 μ M hemin solution in 0.050 M (1.0 M) KCl (**Figure 5.1**) show a broad band at the wavelength of 398 nm, characteristic of the Soret band attributed to π - π^* absorption in the porphyrin ring structure (Harada et al., 2009). Weaker absorptions or Q - bands are observed in the wavelength range of 500 – 750 nm. The UV-vis spectra at various hemin concentrations show an increase in absorbance with rising hemin concentrations. The extinction coefficient of hemin solutions and hemin in KCl solution were determined using the absorbance at a wavelength of 396.46 nm. The values obtained were $5.58 \pm 0.0012 \times 10^4 \text{ M}^{-1}\text{cm}^{-1}$ and $4.00 \pm 0.0015 \times 10^4 \text{ M}^{-1} \text{ cm}^{-1}$, respectively, using Beer-Lambert's law (**Equation 5.1**) (Yang, Xia, Lei, and Wang, 2010).

$$A = \epsilon bc \quad (5.1)$$

Where A is the absorbance of a solution, ϵ is the molar absorptivity of the absorbing species, b is the path length, and c is the concentration of the absorbing species.

The extinction coefficient in high salt concentrations is lower than that of dimeric species in aqueous solution due to the apparent hydrodynamic radii of hemin being larger in high salt concentrations compared to those in aqueous solution (Asher et al., 2009). This work investigates the role of hemin in high salt concentration solutions, where higher concentrations may promote aggregation or complex formation of hemin. In **Figure 5.1a**, a broader Soret band was observed in various hemin solutions in 0.050 M KCl (1.0 M KCl). This broadening is attributed to the presence of a μ -oxo dimer hemin structure and the formation of π - π stacks of the μ -oxo dimers, leading to the formation of large aggregates in high salt concentrations (Asher et al., 2009).

The IR spectra of hemin exhibited a characteristic absorption peak at 1693 cm^{-1} representing the carboxyl group of hemin (Niu, Liu, Li, Wang, and Yuan 2020) and the band at 1272 cm^{-1} was attributed to the C–N secondary stretching vibration in the hemin skeleton structure (Shu et al., 2019). The hemin monomer shows a doublet band at about 900 cm^{-1} , while the hemin dimer exhibits a sharp peak at 933 cm^{-1} , indicating the presence of the oxo-bridged (Fe–O–Fe) structure of the μ -oxo dimer (de Villiers et al., 2007), the asymmetric stretching vibration of the oxygen-atom between the two metal complex residues (**Figure 5.1b**) (Brown, Jones, and Lantzke 1969).

Table 5.1 Extinction coefficients of Hemin at 393 nm in aqueous solutions and in 0.050 M KCl (1.0 M KCl).

Solution	Extinction coefficient (ϵ , $\text{M}^{-1}\text{cm}^{-1}$)
Hemin solution	$5.58 \pm 0.0012 \times 10^4$
Hemin solution in 0.050 M KCl (1.0 M KCl)	$4.00 \pm 0.0015 \times 10^4$

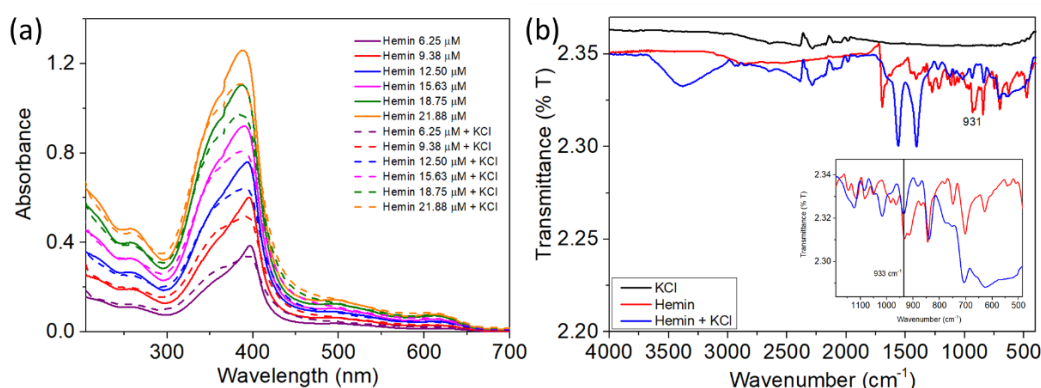


Figure 5.1 (a) UV-visible spectra at varied hemin concentrations (6.25 – 21.88 μM) in aqueous 1.0 M KCl solutions. (b) FT-IR spectra of KCl, hemin solution (monomer) and hemin solution in KCl (dimer).

5.2 The stability of the hemin solution color in electrolyte solutions

Electrochemical measurements require the presence of supporting electrolytes to balance charge in the voltammetric technique. The introduction of various salts such as NaCl, KCl, and LiCl also affects the oxygen concentration in water, as the solution salinity depends on the nature of the cation in the added salt. All of these salts contain chloride ions (Cl^-), and the main difference between them lies in the cation, which can influence the hydrogen bond network between the salt and water differently. This work used a common supporting electrolyte, KCl, K^+ has a lower charge density than Na^+ and Li^+ , leading to a less ordered structure of bulk water around itself or the lowest effect on the hydrogen-bonded network compared to other salts due to the increase in the hydration entropy values ($\Delta_s S$) of the surrounding solvent. This permits the oxygen molecule to be easily transferred to bulk water (Zannotti and Giovannetti, 2015).

In this section, the stability of the hemin solution color in electrolyte solutions was investigated under various supporting electrolyte conditions using UV-vis spectrophotometry, as depicted in **Figure 5.2**. After bubbling O_2 through the solution of 200 μM hemin in 0.005 M (0.10 M), 0.020 M (0.4 M), 0.035 M (0.7 M) KCl at a flow rate of 0.50 L min^{-1} for 3 minutes, the characteristic reddish-brown color faded, with the absorbance at 385 nm decreasing by $71.45 \pm 0.10\%$, $60.57 \pm 0.40\%$, $34.26 \pm 0.30\%$, respectively, as illustrated in **Figure 5.2a**.

On the other hand, at high KCl concentrations ranging from 0.050 M (1.0 M) to 0.15 M (3.0 M), hemin demonstrated remarkable stability. It showed no change in color or absorbance ($\leq 5\%$) even after bubbling with N_2 and O_2 . This stability persisted even after aging the samples for an extended period, exceeding 3 months. These findings suggest that the interaction between hemin and N_2 or O_2 gas in high salt concentration is not strong enough to induce any changes in the Soret absorption bands or in the color of the hemin solution.

Normally, the concentration of the supporting electrolyte should be inert and not interact with the electroactive species, typically varying between 0.1 and 1.0 M (Carucci, Salis, and Magner, 2017). In this study, we utilized hemin concentrations in a 1.0 M KCl solution to investigate O_2 reduction. This KCl concentration falls within the suitable range for supporting electrolyte concentration and remains unchanged in color after O_2 bubbling, thereby facilitating the investigation of electrocatalytic dioxygen reduction.

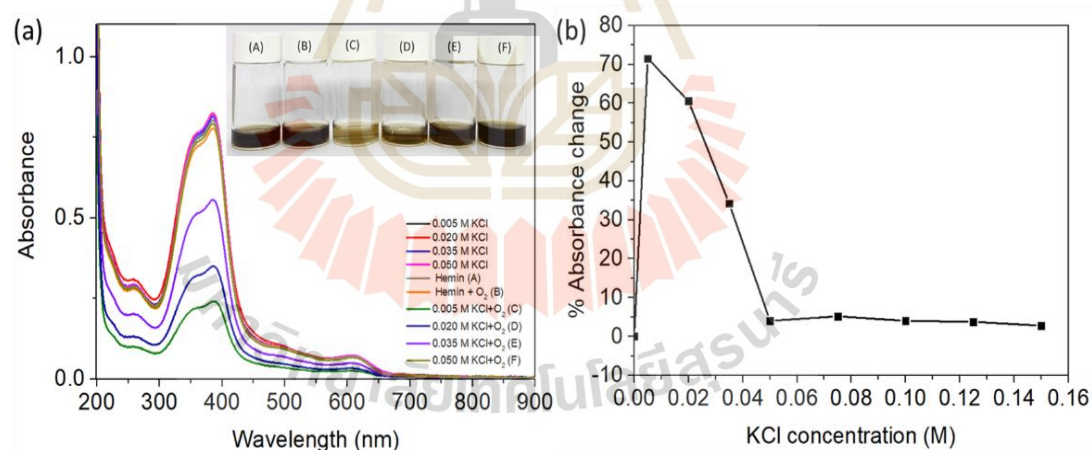


Figure 5.2 (a) 100 μ M hemin solution in (A) 0.005 M KCl and (B) 0.020 M KCl, (C) 0.035 M KCl and (D) 0.050 M KCl after bubble O_2 at the flow rate of 0.50 L min^{-1} for 3 minutes, (A) hemin solution without KCl, (B) hemin solution after bubble O_2 gas, (C) hemin solution + 0.005 M KCl after bubble O_2 gas, (D) hemin solution + 0.020 M KCl after bubble O_2 gas, (E) hemin solution + 0.035 M KCl after bubble O_2 gas, (F) hemin solution + 0.050 M KCl after bubble O_2 gas and (b) % absorbance change at various KCl concentration.

5.3 Electrochemical properties of hemin in high salt concentration without oxygen molecules

Hemin exists in both monomeric and dimeric forms, which contribute to multiple redox sites in the cyclic voltammetry (CV) curve (Liang, Song, and Liao, 2011). In this work, hemin exhibits two anodic redox peaks at -0.47 V and 0.7 V. The weak anodic peak observed at -0.47 V corresponds to the oxidation potentials of the Fe(III)/Fe(II) center in hemin (Palanisamy et al., 2019; Zhao, Chu, and Yang, 2017). Moreover, an oxidation peak of hemin centered at 0.7 V reported by Liang et al. (Liang et al., 2011). The anodic current of hemin in the absence of O₂ in 1.0 M KCl was observed to be proportional to the hemin concentration as shown in **Figure 5.3** (Aoki et al., 2014). Thus, the wave at 0.7 V should be caused by the oxidation of hemin. Additionally, the anodic peak current of hemin at 0.7 V was proportional to the square roots of the scan rate, indicating diffusion control (**Figure 5.4a**) (Aoki, Li, Chen, and Nishiumi, 2014). The hemin-modified electrode only exhibits the diffusion-controlled current of hemin when applied to either platinum or gold electrodes (Li, Aoki, Chen, and Nishiumi, 2015). A linear relationship between I_{pa} and hemin concentration exists in the range of 25 to 100 μM , with a sensitivity of $0.1793 \mu\text{A} \mu\text{M}^{-1}$. The detection limit was found to be 23.095 μM .

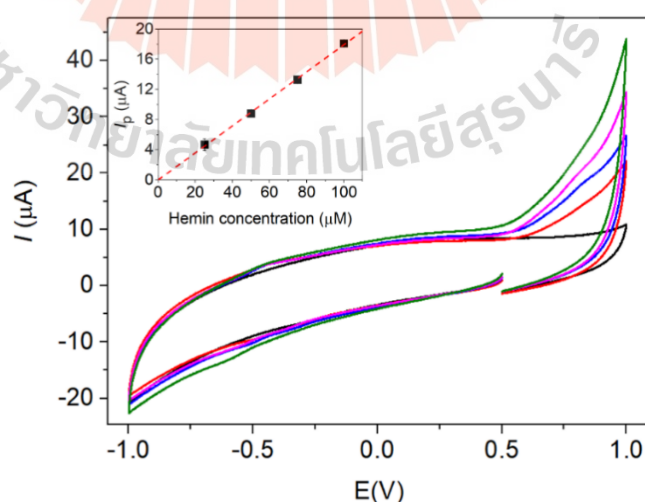


Figure 5.3 CV of varied hemin concentration in deoxygenated 1.0 M KCl at a scan rate of 100 mV s^{-1} . Hemin concentration: (black) $0 \mu\text{M}$, (red) $25 \mu\text{M}$, (blue) $50 \mu\text{M}$, (pink) $75 \mu\text{M}$, and (green) $100 \mu\text{M}$.

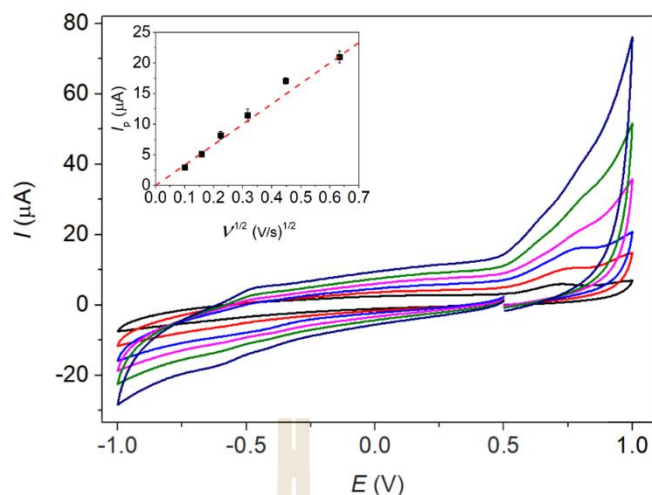


Figure 5.4 CV of 200 μM deoxygenated hemin in 1.0 M KCl at varied scan rate. The inlay shows the plot of the reduction peak currents against the square root of scan rate. (black) 10 mV s^{-1} , (red) 25 mV s^{-1} , (blue) 50 mV s^{-1} , (pink) 100 mV s^{-1} , (green) 200 mV s^{-1} , and (dark blue) 400 mV s^{-1} .

5.4 Electrochemical properties of dioxygen in high salt concentration in the absence of hemin

The catalytic reduction of dioxygen in high salt concentration was observed within the potential range of -0.3 to -0.5 V at various scan rates, as illustrated in **Figure 5.5**. The cathodic current increases while the anodic current disappears. The reduction current of saturated O_2 demonstrates proportionality to the square root of the scan rate, suggesting a diffusion-controlled process (Zheng et al., 2002). At low scan rates (10 – 50 mV s^{-1}), the peak potentials remained unchanged. However, at high scan rates (100 – 400 mV s^{-1}), the peak potentials exhibited a slight shift towards more negative values (Li, Aoki, Chen, and Nishiumi, 2015).

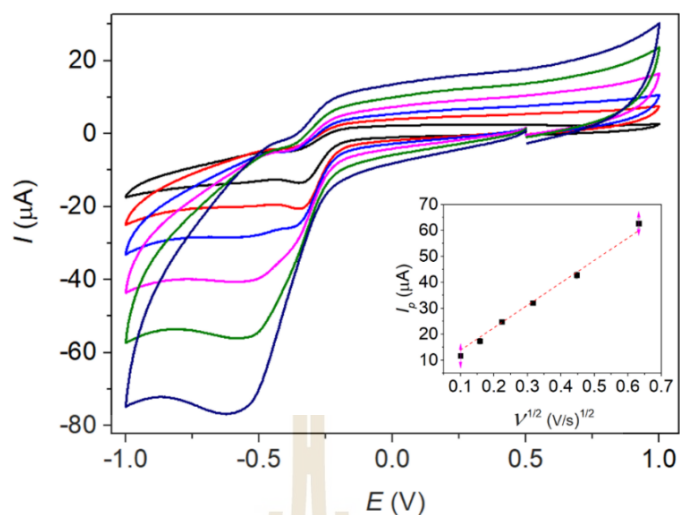


Figure 5.5 CV of O_2 -saturated 1.0 M KCl solution at varied scan rate. The inlay shows the plot of the reduction peak currents against the square root of scan rate. (black) 10 mV s^{-1} , (red) 25 mV s^{-1} , (blue) 50 mV s^{-1} , (pink) 100 mV s^{-1} , (green) 200 mV s^{-1} , and (dark blue) 400 mV s^{-1} .

In saturated O_2 concentration, the diffusion coefficient of O_2 at bare GCE without hemin was calculated to be $0.75 \times 10^{-10} \text{ m}^2 \text{ s}^{-1}$ where $\alpha_{n'+1} = 0.57 \pm 0.003$ using the following **equation 5.6**: ($n=4$)

$$I_p = 0.496 \sqrt{n' + \alpha_{n'+1}} n F A c^* \sqrt{\frac{FvD}{RT}} \quad (5.2)$$

Where I_p is the peak current, n' is the number of electron transfer before the rate determining step, n is the total number of electrons transfer ($n=4$), $\alpha_{n'+1}$ is the cathodic transfer coefficient of the rate determining step, A is the electrode surface area, D is the diffusion coefficient, c^* is the bulk concentration, V is the voltage scan rate, F is the Faraday constant ($96,485 \text{ C mol}^{-1}$), R is the molar gas constant ($8.314 \text{ J K}^{-1} \text{ mol}^{-1}$), and T is the absolute temperature.

In **figure 5.6**, the bare glassy carbon electrode (GCE) could not detect saturated O_2 concentrations in high salt concentration, but it was able to detect low O_2 concentrations in 1.0 M KCl, which approached the O_2 content in the KCl solution when N_2 was bubbled (as indicated by the purple line). The wave at -0.5 V can be

attributed to the catalytic reduction of O_2 (Zhao et al., 2017). A linear relationship between the peak currents and O_2 concentrations was observed in the range of 181.25 to 312.50 μM , with a sensitivity of $0.13 \mu\text{A} \mu\text{M}^{-1}$ and a detection limit of 36.67 μM .

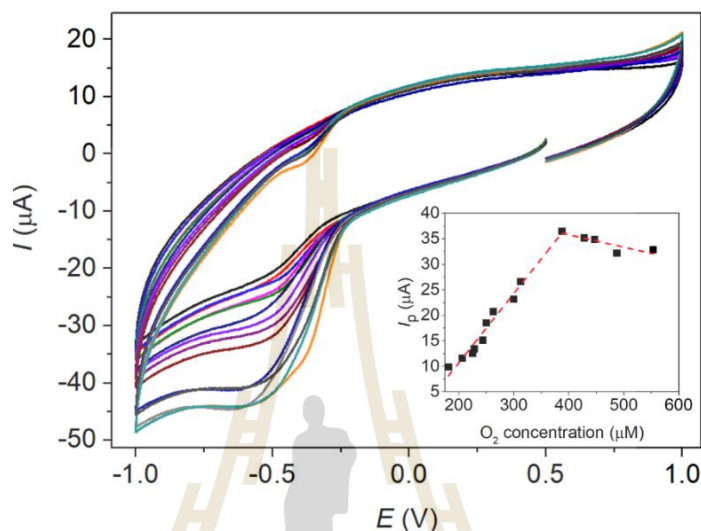


Figure 5.6 CV of O_2 -saturated and deoxygenated 1 M KCl solution at a scan rate of 100 mV s^{-1} . The inlay shows the plot of the reduction peak currents against the O_2 concentration.

5.5 Electrochemical properties of hemin in high salt concentration with oxygen molecules

The electrochemistry of hemin in aqueous solutions is constrained by solubility and aggregation behavior (A. Toader and Volanschi, 2007). In this study, a hemin solution was utilized to catalyze the reduction of O_2 using cyclic voltammetry (CV) at a bare glassy carbon electrode (GCE). A comparison of oxygen-saturated, normal-aerated, and deaerated conditions of KCl and hemin solution was observed. The reduction of O_2 at the bare GCE occurred at -0.45 V in the air-saturated hemin solution (black, **Figure 5.7**), while the oxidation peak of hemin appeared at 0.70 V .

In the KCl solution, only the cathodic wave at -0.45 V was observed (pink, **Figure 5.7**). However, under aerated conditions, the reductive current significantly increased (green, **Figure 5.7**). The reduction peak of the hemin solution disappears

under deaerated conditions; no reduction peak of the central ion (Fe^{3+} to Fe^{2+}) (blue line) at -0.45 was observed (Berezina, Bazanov, Maksimova, and Semeikin, 2017; Le and Jeong, 2018).

In this work, hemin exhibits strong electrocatalytic activity for O_2 reduction. The Fe^{3+} porphyrin can bind with superoxides ($\text{O}_2^{\bullet-}$) through covalent bonding (Ortiz de Montellano et al., 1998; Sokolov et al., 2017). A high reduction peak current (red, **Figure 5.7**) at -0.45 V in the O_2 -saturated hemin - KCl solution was observed due to the formation of a complex between hemin and the O_2 molecule, [Hemin (Fe^{3+}) - O_2] and a charge-transfer-complex chain of O_2 and Fe^{3+} atom (Gao and Chen, 2005) (K. J. Aoki et al., 2014; K. J. Aoki, Taniguchi, and Chen, 2020; Appleby, Savy, and Caro, 1980; Kolpin and Swofford, 2002; Le and Jeong, 2018; Li, Aoki, Chen, and Nishiumi, 2015; Singh and Buttry, 2012). The air-saturated solution exhibited only the cathodic wave, with the peak located at the same potential as in the deaerated solution. The oxygen reduction at about -0.45 V occurs at a potential closely related to the redox potential of the iron porphyrin couple (Bettelheim and Kuwana, 2002).

The similarity in the observed CV response for these electrodes is attributed to the iron active site in the porphyrin ring, which plays a key role in the catalytic response (K. J. Aoki et al., 2014; Gao and Chen, 2005; Sokolov et al., 2017). In this work, the sensitivity of O_2 significantly increases in the presence of hemin, and the large aggregates of the μ -oxo dimers in the hemin structure in high salt concentrations do not influence the electrocatalytic O_2 reduction. Metalloporphyrin, in general, exhibits the ability to catalyze the reduction of oxygen, leading to the generation of water through a four-electron process or hydrogen peroxide through a two-electron process. Subsequently, hydrogen peroxide was further reduced to form water (Šljukić, Banks, and Compton, 2005). O_2 undergoes reduction in the gap between two porphyrin rings at the axial position of the iron with a parallel conformation. Porphyrin monomers can bind an O_2 molecule and reduce O_2 via a $4e^-$ process, as shown in **scheme 5.1**. The reduction of O_2 with 4 electrons typically results in the formation of water (H_2O) that reported by Collman et al (Collman, Elliott, Halbert, and Tovrog, 1977) (Antoniadou, Jannakoudakis, and Theodoridou, 1989). Additionally, Fe-N_4 structure can catalyze 4-electron oxygen reduction and the product is water (Si et al.,

2014). So that, in this work, the suggested model for the hemin-catalyzed reduction of O_2 was observed as follows and illustrated in **Scheme 5.2** (Chatterjee, Sengupta, Mondal, Dey, and Dey, 2017; Kolpin and Swofford, 2002; Singha, Mondal, Nayek, Dey, and Dey, 2020; Sokolov et al., 2017; Vasudevan et al., 2013).

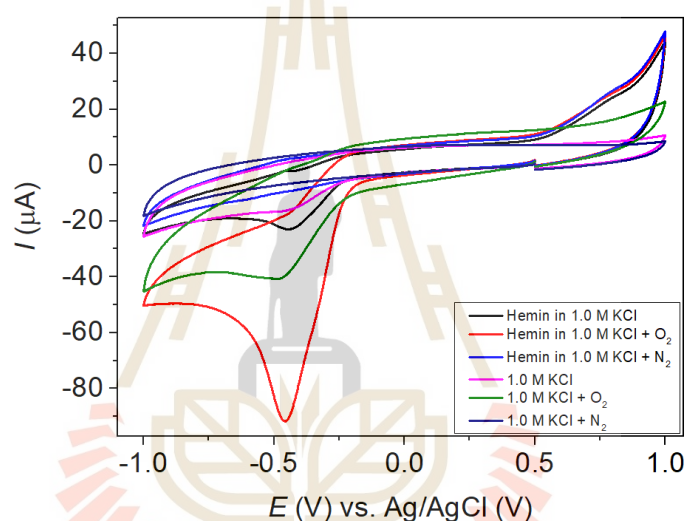
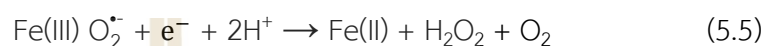
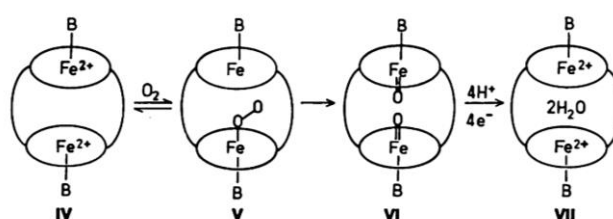
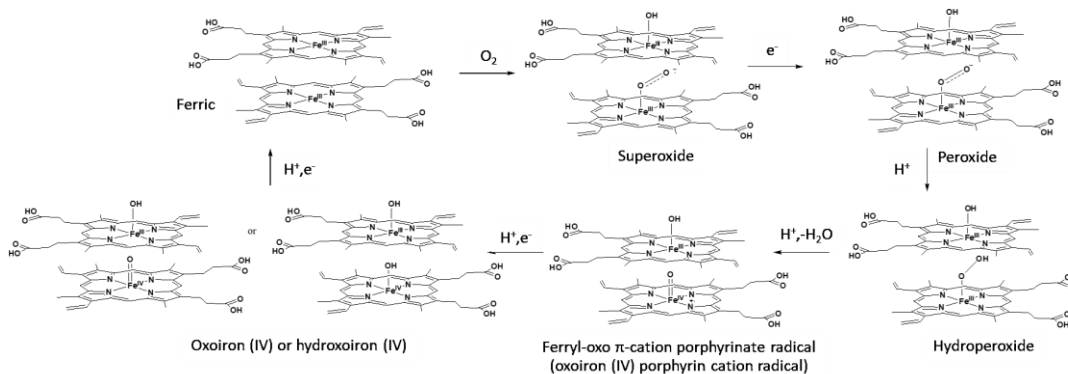


Figure 5.7 CV of 200 μM hemin in 1.0 M KCl (black), hemin saturated with O_2 (red), hemin saturated with N_2 (blue), blank KCl (pink), blank KCl saturated with O_2 (green), at scan rate 100 mV s^{-1} .



Scheme 5.1 Proposed reaction of O_2 with a "face-to-face" binary Fe^{2+} porphyrin. B is an axial base too large to fit in the cavity. Ovals represent porphyrin rings (Collman, 1977).



Scheme 5.2 Oxygen reduction mechanism by hemin in high salt concentration (Huang and Groves, 2018).

The O_2 reduction mechanism involves a multistep process that includes electron transfers, chemical reactions, and the formation of various chemical intermediates (Sokolov et al., 2017). The two Fe (III) heme molecules bind with one O_2 molecule to form a complex and generate the dioxygen adduct (Li et al., 2015). In this work, a binuclear "face-to-face" $\pi - \pi$ dimeric structure of Fe (III) macrocyclic complex can bind and reduce O_2 in the space between the two metal atoms and the porphyrin rings in parallel conformation, with the Fe-Fe gap approximately ranging from 4.5 to 6.8 Å (Collman et al., 1977; Mihara et al., 2017; Si et al., 2014).

At the surface of glassy carbon electrode, the dioxygen superoxide radical ($\text{O}_2^{\bullet-}$) is the initial species of O_2 reduction ($\text{O}_2 + \text{e}^- \rightarrow \text{O}_2^{\bullet-}$) that is generated electron transfer from the GC electrode (Le and Jeong, 2018). Iron (Fe^{3+}) has the capability to bind with $\text{O}_2^{\bullet-}$, resulting in the formation of the initial ferric superoxide intermediate. With the addition of the first electron, the superoxide undergoes transformation into a ferric peroxide. Protonation of the ferric peroxide further leads to the formation of a ferric hydroperoxide, $\text{Fe}^{\text{III}}\text{-OOH}$. The distal oxygen of the hydroperoxide species is protonated by a second proton, causing heterolytic O–O bond cleavage to produce a highly reactive high-valent ferryl-oxo π -cation porphyrinate radical. Protonation of the ferryl-oxo π cation porphyrinate radical and re-reduction of Fe by an electrode surface could result in the overall catalytic reduction of O_2 to H_2O . Furthermore, the interaction between Fe (III) and $\text{O}_2^{\bullet-}$ is continuously reversibility during the catalytic process (Collman et al., 1977; Huang and Groves, 2018; Kim 2020; Song and Zhang,

2008; Antoniadou et al., 1989; Pegis et al., 2019). In this work, the addition of an inert salt does not affect the behavior of the electroactive species (oxygen gas) through changes in ionic strength (Compton, Laborda, and Ward, 2013).

The voltammetric behavior of hemin was observed at a bare glassy carbon electrode in O₂-saturated 1.0 M KCl over a wide range of scan rates from 10 to 400 mV s⁻¹. The well-defined peak current exhibited a linear relationship with the square root of the scan rate in the bulk of the salt solution, indicating a diffusion-controlled process (Koichi Jeremiah Aoki et al., 2014; Singh and Buttry, 2012; Ye et al., 2004). The corresponding peak potentials remained almost unchanged, as shown in **Figure 5.8**. In saturated O₂ concentration, the diffusion coefficient of O₂ in the hemin solution was found to be $3.86 \times 10^{-9} \text{ m}^2 \text{ s}^{-1}$, calculated from **equation 5.2**. This value is higher than that in a blank KCl solution and is consistent with values reported in previous studies (Jamnongwong, Loubiere, Dietrich, and Hébrard, 2010; Schmitz, Anlauf, and Rehrmann, 2013).

Figure 5.9 presents a comparison of the scan rate dependence of the cathodic peak current of O₂ for O₂-saturated Hemin solution (**Figure 5.8**) and O₂-saturated blank solutions (**Figure 5.5**). The component above the proportional line of the blank solution indicates that the catalytic peak current of the hemin solution was more than 2.4 times that of the blank solution. Therefore, hemin proves to be an effective electrocatalyst mediating the oxygen reduction reaction in high salt concentration (Li et al., 2015).

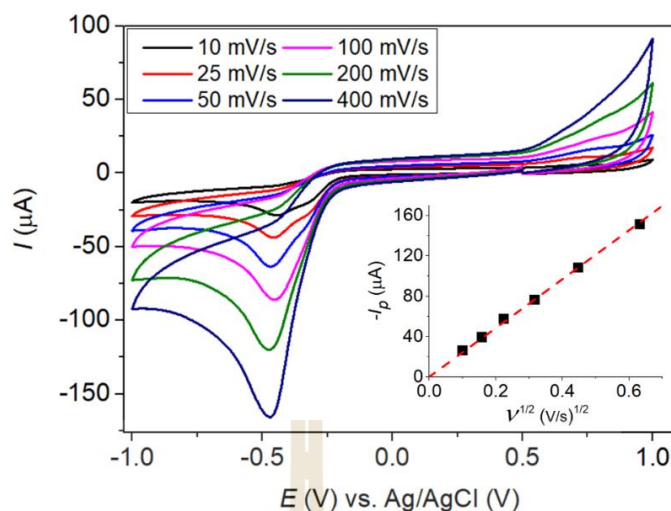


Figure 5.8: CV of 200 μM hemin in 1.0 M KCl at bare GCE and at varied scan rates after bubble O_2 3.0 mins (flow rate 0.50 ml min^{-1}). (black) 10 mV s^{-1} , (red) 25 mV s^{-1} , (blue) 50 mV s^{-1} , (pink) 100 mV s^{-1} , (green) 200 mV s^{-1} , and (dark blue) 400 mV s^{-1} .

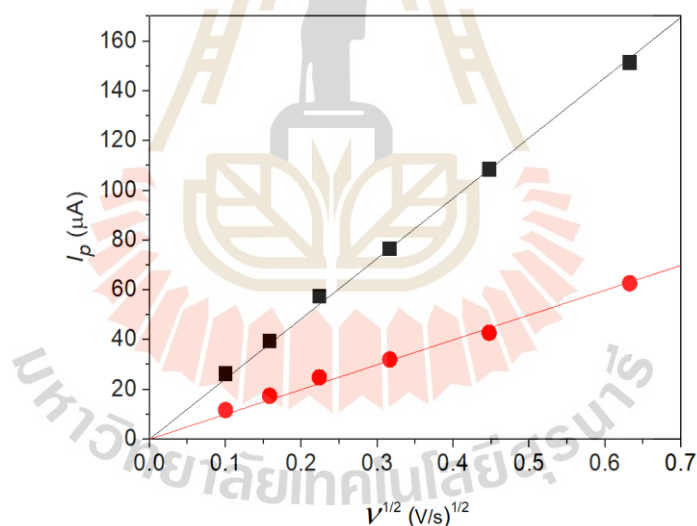


Figure 5.9: Scan rate dependence of the cathodic peak current of O_2 in O_2 saturated hemin solution and O_2 saturated 1.0 M KCl at bare GCE.

The effect of hemin concentration on the catalytic current increase in saturated O_2 solution was observed in **Figure 5.10**. The cathodic peak current in an O_2 -saturated hemin solution exhibits a linear increase with the rising concentration of hemin in the nanomolar range. This behavior is attributed to the specificity of hemin for O_2 , allowing more hemin molecules to bind with O_2 and resulting in an increased peak

current. In **Figures 5.10 to 5.12**, the maximum peak current was observed at nanomolar concentrations of hemin. However, as the concentration of hemin increases to micromolar levels, the peak current levels off and remains constant at 5 μM of the O_2 -saturated hemin concentration.

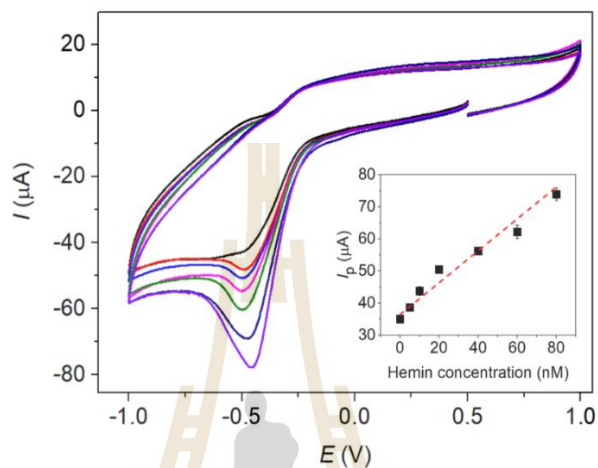


Figure 5.10 CV of varied hemin concentration ranging from 5 nM to 80 nM in 1.0 M KCl solution at a scan rate of 100 mV s^{-1} . The inlay shows the plot of the reduction peak currents against the hemin concentration. (black) 0 nM, (red) 5 nM, (blue) 10 nM, (pink) 20 nM, (green) 40 nM, (dark blue) 60 nM, and (purple) 80 nM.

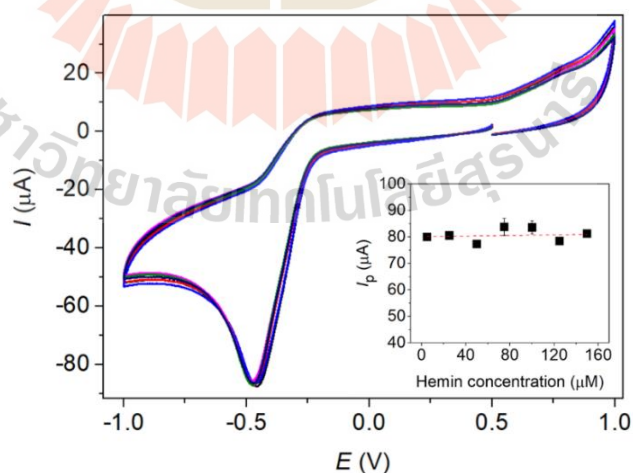


Figure 5.11 CV of varied hemin concentration ranging from 5 μM to 150 μM in 1.0 M KCl solution at a scan rate of 100 mV s^{-1} . The inlay shows the plot of the reduction peak currents against the Hemin concentration.

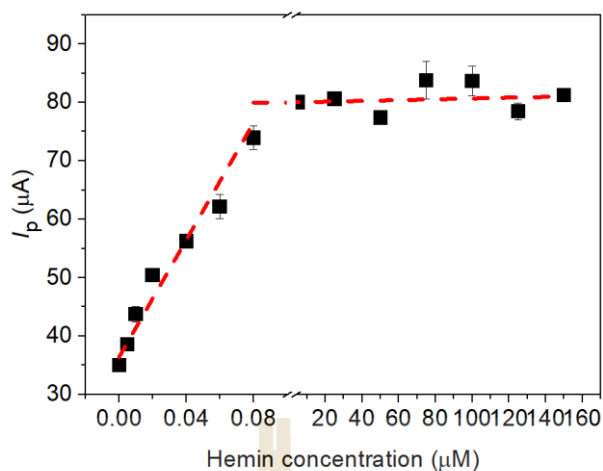


Figure 5.12 Calibration of varied hemin concentration ranging from 5 nM to 150 μM in 1.0 M KCl solution at a scan rate of 100 mV s^{-1} .

5.6 Tafel analysis

Tafel analysis (equation. 5.6) was used to investigate the electron transfer kinetics of O_2 reduction at a bare GCE in an oxygen-saturated hemin solution at a low scan rate (Compton and Banks, 2007).

$$\frac{\partial \ln I}{\partial E} = \frac{n' + \alpha_{n'+1} F}{RT} \quad (5.6)$$

Where n' is the number of electron transfer before the rate determining step (RDS), $\alpha_{n'+1}$ is the cathodic transfer coefficient of the RDS, I is the electrical current, E is the potential, F is the Faraday constant ($96,485 \text{ C mol}^{-1}$), R is the molar gas constant ($8.314 \text{ J K}^{-1} \text{ mol}^{-1}$), T is the absolute temperature (298 K), (Guidelli et al., 2014)

The voltammograms obtained at a slow scan rate of 10 mV s^{-1} were used to calculate the cathodic transfer coefficient, $\alpha_{n'+1}$, from Tafel slope of this slow step. The line of best fit for $\ln I$ vs. E was determined using currents in the range of 15–50% of the peak current to mitigate the mass transport effect. The calculated $\alpha_{n'+1}$ was determined to be 0.57 ± 0.003 , consistent with previous literature reports (Clark, Ngamchuea, Batchelor-McAuley, and Compton, 2017; Sokolov, Sepunaru, and Compton, 2017).

5.7 Calibration plot

The dissolved oxygen sensor was used to investigate the activity of O₂ in a high KCl concentration under interference ion-free conditions. The O₂ concentration was varied by changing the time interval of O₂ bubbling. This sensor exhibited a rapid response after the addition of saturated O₂ gas. The cathodic current slowly decreased with increasing time intervals due to the declining O₂ concentration. Subsequently, N₂ was employed to replace O₂, facilitating control over a low concentration range of O₂. The O₂ concentration was confirmed using a DO meter.

The calibration of O₂ concentration is depicted in **Figure 5.13**. A linear response of the reduction peak current at - 0.45 V was observed within the concentration range of 75 – 610 μM. The results obtained from the developed sensor were consistent with those measured using the DO meter. This calibration plot illustrates the relationship between current and O₂ concentration suggesting that the interaction between O₂ molecules and ferrous-hemin leads to changes in the CV response. (inset image of Fig. 5.10) The sensitivity and LOD of this sensor were determined to be 0.14 μA μM⁻¹ and 11.79 μM, respectively. The linearity of the cathodic peak current can be expressed as $I_{pc} (A) = 0.13x (R^2 = 0.99)$. This indicates that hemin catalyst solution can be utilized for sensitive detection of dissolved oxygen (DO) (Zheng et al., 2002a). If dissolved oxygen levels drop to 3.0 mg L⁻¹, it indicates a dangerous situation for supporting common aquatic life including hypoxia (Ali, Anushka, and Mishra 2022). Therefore, this sensor can effectively detect the low concentration range of O₂ in wastewater. Moreover, the advantage of this sensor can prevent the loss of hemin from the hemin-modified electrode surface during cyclic voltammetry (CV) cycling.

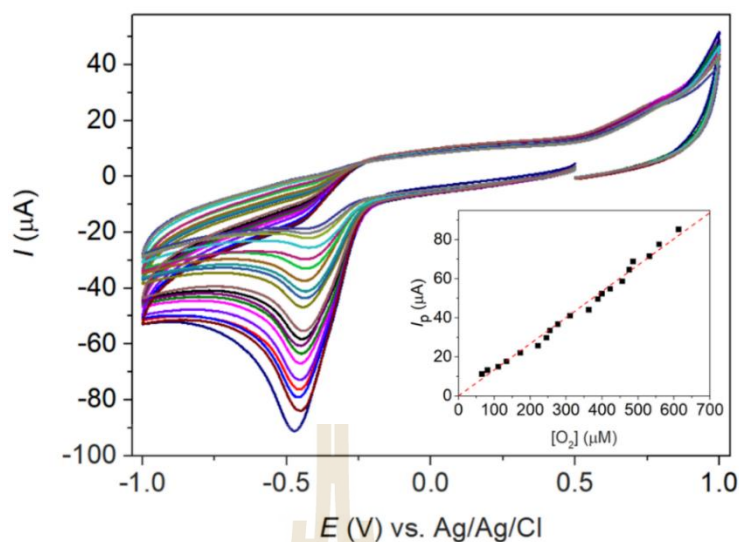


Figure 5.13 CV of 200 μM hemin in 1.0 M KCl at varied concentration of O_2 by bubbling N_2 gas (75.00 – 256.25 μM) and varied concentration of O_2 (328.13 - 610.00 μM) at scan rate 100 mV s^{-1} (Inset: average calibration plot of O_2 reduction of 200 μM hemin at varied concentration of O_2)

5.8 The effect of hemin as a catalyst in high salt concentration

This investigation aims to explore the apparent dependence on the hemin catalyst in high salt concentration. **Figure 5.14** presents a comparison of the O_2 calibration plots between hemin solutions and the blank solution under both deoxygenated and O_2 -saturated conditions. In a blank solution (1.0 M KCl) or in the absence of hemin, there is a limitation in detecting a high range of O_2 concentrations. In contrast, a hemin solution demonstrates high sensitivity to oxygen (O_2) within a high O_2 concentration range as shown in **Figure 5.14**. Due to its prosthetic group, which is similar to cytochrome oxidase and heme, hemin has been extensively studied as a mediator for electrocatalyzing the reduction of O_2 (Toader, Volanschi, Lazarescu, and Lazarescu, 2010; Zheng et al., 2002).

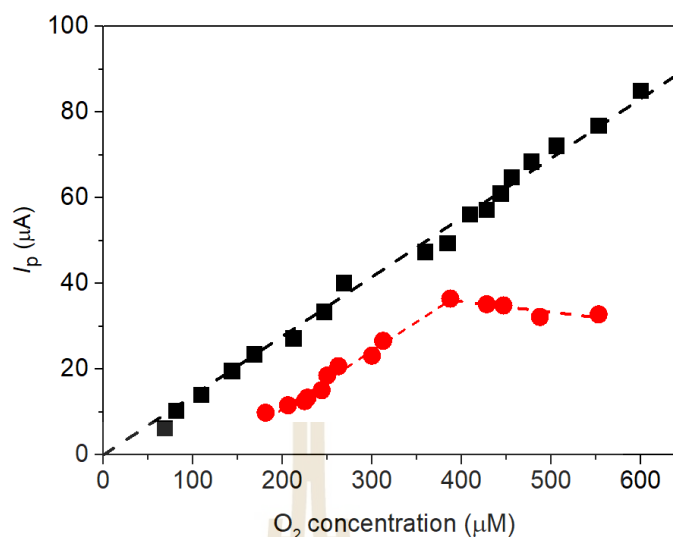


Figure 5.14 Comparison of the calibration plot between a deoxygenated and O₂-saturated hemin solution (black) and a deoxygenated and O₂-saturated 1.0 M KCl solution (red) at a scan rate of 100 mV s⁻¹.

5.9 Reproducibility

The reproducibility of this sensor was tested by conducting five successive measurements on the same solution using a 200 μM hemin solution in 1.0 M KCl at a flow rate of 0.50 L min⁻¹ for 3.0 minutes. The reversibility of O₂ adsorption at high salt concentration depends on the decomposition of [hem (Fe³⁺) - O₂^{•-}]_{ad} complex and the alkalinity in this solution. [hem (Fe³⁺) - O₂^{•-}]_{ad} complex can decompose and reverse into hem (Fe³⁺)_{ad} and soluble O₂^{•-} (Mihara et al., 2017; Song and Zhang, 2008; Bettelheim and Kuwana, 2002). The potential and peak current remained almost unchanged after successive scanning and retained almost 100% of their initial values, as shown in **Figure 5.15**. The relative standard deviation (RSD) of the calibration slope was found to be less than 5.0% (specifically, 4.61%). This observation indicates stable and highly reproducible sensor performance.

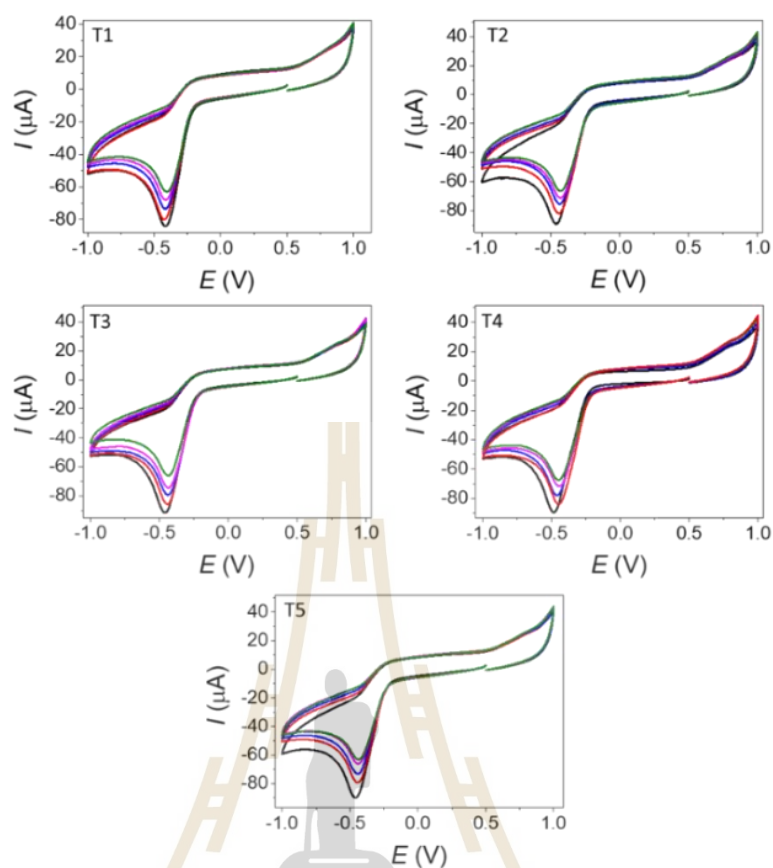


Figure 5.15 Reproducibility and stability measurements: CV response of a 200 μM hemin solution at GCE in 1.0 M KCl at a flow rate of 0.50 L min^{-1} for 3.0 minutes by conducting five successive measurements.

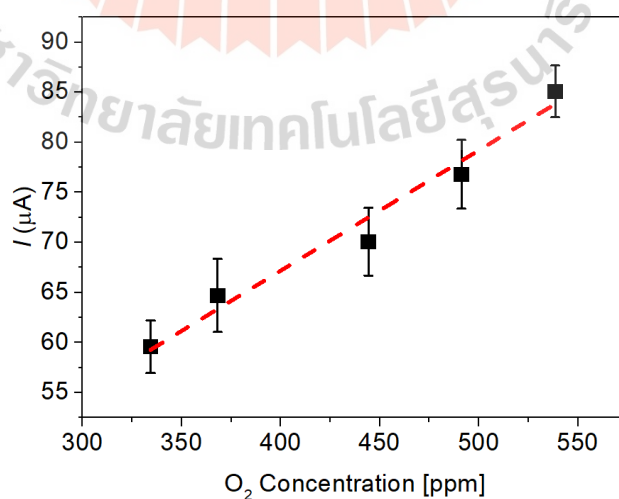


Figure 5.16 Average reproducibility and stability measurements of O_2 reduction in 200 μM hemin solution in 1.0 M KCl by conducting five successive measurements.

5.10 Interference

Inorganic salts with high ionic strength can influence the solubility of O_2 due to the interaction of water molecules with the salt ions, forming hydrated salts. The increased presence of hydrated salts will lead to a decrease in the number of dissolved oxygen molecules in the solution (Lange, Staaland, and Mostad 1972; Langenfeld and Bugbee 2021; F. J. Millero, Huang, and Laferiere, 2002). In this study, the behavior of dissolved oxygen was examined in the presence of various high ionic strength interfering species within a hemin solution. 0.80 mM Ca^{2+} and Cl^- ($CaCl_2$), 0.61 mM glucose, 0.69 mM K^+ and SO_4^{2-} (K_2SO_4), 0.70 mM K^+ and NO_3^- (KNO_3), 0.91 mM Mg^{2+} and SO_4^{2-} ($MgSO_4$), 0.70 mM NH_4^+ and Cl^- (NH_4Cl), 0.63 mM Na^+ and SO_4^{2-} (Na_2SO_4), 0.53 mM Na^+ and $HP_4O_{10}^{2-}$ (Na_2HPO_4), 0.67 mM Na^+ and $H_2PO_4^-$ (NaH_2PO_4), and 0.87 mM Na^+ and NO_2^- ($NaNO_2$) was added in hemin solution and the response ratio was found to be 1.19%, 2.52%, 0.29%, 2.76%, 1.80%, 1.73%, 3.09%, 0.47%, 0.53% and 2.94% respectively, on peak responses of DO as reported in Fu et al (Fu et al., 2015). The signal of each interfering compound and the mixture was approximately the same as that of the blank solution, with observed effects on peak DO responses being less than 5%.

In common interferences found in natural water, such as ascorbic acid, that may potentially interfere with the O_2 reduction peak, no obvious O_2 reduction peak was observed as shown in **figure 5.17l**. Moreover, the voltammetry signals exhibited a significant influence on the oxidation peak of hemin in the presence NO_2^- of at 0.8 V due to a large number of active sites on the glassy carbon electrode (GC) that are selective for nitrite, as shown in Fig. 5.14k (Canales, Antilén, Chapa, Del Río, and Ramírez, 2014). The presence of NO_2^- as interference results in a large oxidation peak at 0.8 V, but it does not interfere with the O_2 reduction peak. Therefore, the voltammetry signals of this sensor did not exhibit any significant influence on the O_2 reduction peak in the presence of Cl^- , NO_3^- , and PO_4^{3-} , but previous research has suggested an impact of NO_3^- and PO_4^{3-} on dissolved oxygen (DO) detection (Hsu and Selvaganapathy, 2013). Therefore, the activity of an oxygen-saturated hemin solution is independent of dissolved contaminants, except for NO_2^- and ascorbic acid. These results indicate that the O_2 sensor can tolerate high concentrations of salts and

interfering species, making it suitable for measuring dissolved oxygen (DO) levels while performing controlled changes in the dissolved oxygen concentrations in low O_2 concentration.

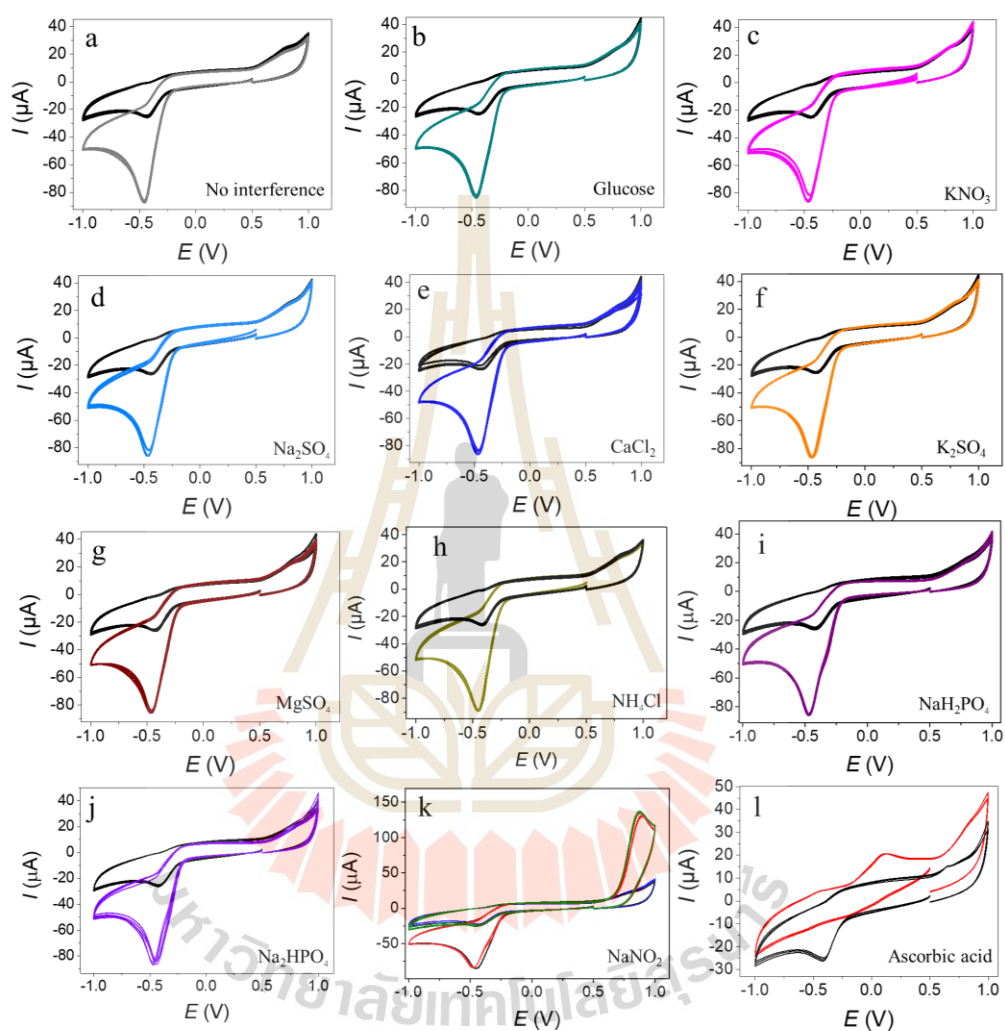


Figure 5.17 CV curve for interference study in hemin solution in 1.0 M KCl and in oxygen-saturated hemin solution (bubble O_2 in 3.0 min, flow rate 0.50 ml min^{-1}) at scan rate 100 mV s^{-1} .

A performance comparison of this DO sensor with other recently developed DO sensors is presented in **Table 2.5**. An ideal oxygen sensor should possess high sensitivity, selectivity, rapid response time, and fast recovery time. To achieve these characteristics, researchers have employed various strategies, including immobilizing

hemin and other electrocatalytic materials on a host substrate to develop highly efficient biosensors such as multiwall carbon nanotube (Ye et al., 2004), graphite (Shigehara and Anson, 1982), graphene (Chen et al., 2011; Fu et al., 2015), multiwall carbon and graphite oxide (Le and Jeong, 2018). Several works have indeed demonstrated potential as active layers for oxygen sensors due to their high catalytic activity and large surface area. However, the stability of hemin on the electrocatalytic materials and the electrode surface was poor, leading to the easy release of porphyrin from the modified electrode surface during CV cycling (Chen et al., 2011; Feng et al., 2011; Zheng et al., 2002b). In this work, the most notable advantage of this sensor is its ability to detect O₂ using hemin in a salt solution, which helps prevent mediator leakage. Additionally, this sensor demonstrates capability across a wide range of analyte concentrations (Yunusa et al., 2014). However, the hemin sensor exhibits lower sensitivity (0.1360 $\mu\text{A } \mu\text{M}^{-1}$) compared to other studies and commercially available Clark electrodes (1.923 $\mu\text{A } \mu\text{M}^{-1}$) (Hsu et al., 2014).

5.11 Conclusion

The electroreduction of O₂ was investigated under high salt conditions using active iron porphyrin as a mediator. This mediator facilitates direct electron transfer between the O₂ molecule in the solution and the bare solid electrode. The reduction of O₂ by hemin was observed at a potential of -0.45 V, corresponding to the formation of a complex between hemin and the O₂ molecule, [Hemin (Fe³⁺)-O₂]. The O₂ reduction mechanism involves the formation of O₂ adducts with ferric ion, followed by the subsequent reduction of the intermediate peroxide and the protonation of hydroperoxide. The limit of detection (LOD) and electrode sensitivity of the hemin solution are higher than those of the blank solution, determined to be 11.79×10^{-6} mol L⁻¹ and 0.14 $\mu\text{A } \mu\text{M}^{-1}$, respectively. These conditions correspond to the presence of a large quantity (> 0.1 M) of an inert electrolyte (supporting electrolyte), which does not interfere in the electrode reaction. With a low limit of detection (LOD), a wide linear range, and high sensitivity, the electrode demonstrates potential utility as a dissolved oxygen sensor. One of the most notable advantages of this sensor is its ability to prevent mediator leakage. Additionally, the hemin-KCl electrode exhibits

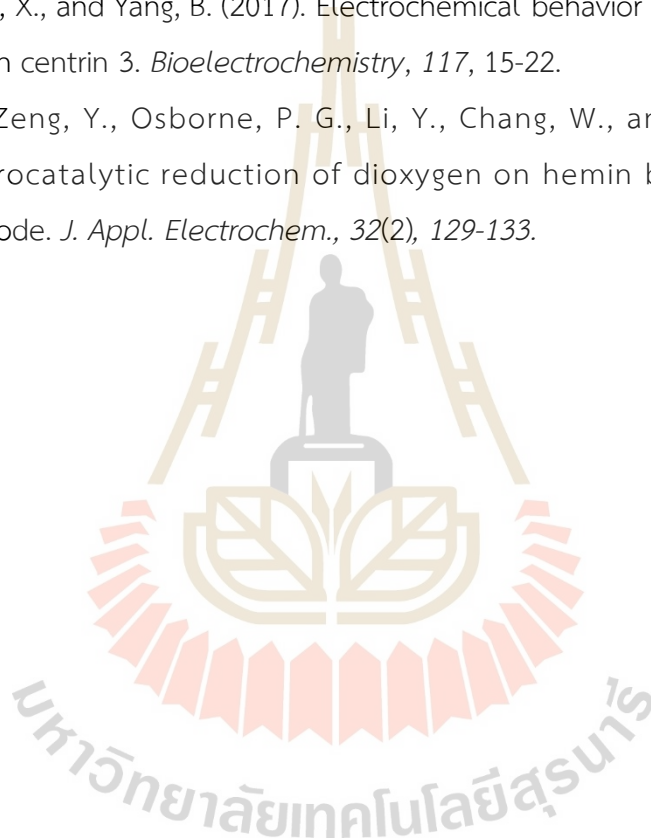
stable electrocatalytic properties, reproducibility in measurements over time (%RSD = 4.61%), and anti-interference capability.

5.12 References

- Ali, B., Anushka, and Mishra, A. (2022). Effects of dissolved oxygen concentration on freshwater fish: A review. *Int. J. Fish. Aquat.*, 10(4), 113-127.
- Antoniadou, S., Jannakoudakis, A. D., and Theodoridou, E. (1989). Electrocatalytic reactions on carbon fibre electrodes modified by hemine I. Electroreduction of oxygen. *Synth. Met.*, 30(3), 283-294.
- Bettelheim, A., and Kuwana, T. (2002). Rotating-ring-disk analysis of iron tetra (N-methyl pyridyl) porphyrin in electrocatalysis of oxygen. *Anal. Chem.*, 51(13), 2257-2260.
- Canales, C., Antilén, M., Chapa, M., Del Río, R., and Ramírez, G. (2014). Electrooxidation of nitrite using an oxidized glassy carbon electrode as amperometric sensor. *Electrocatalysis*, 6(3), 300-307.
- Collman, J. P., Elliott, C. M., Halbert, T. R., and Tovrog, B. S. (1977). Synthesis and Characterization of "face-to-face" porphyrins. *Proc. Natl. Acad. Sci. U S A*, 74(1), 18-22.
- Compton, R., and Banks, C. (2007). Understanding Voltammetry.
- Compton, R. G., Laborda, E., and Ward, K. (2013). Understanding voltammetry: Simulation of electrode processes.
- Hsu, L., Selvaganapathy, P. R., Brash, J., Fang, Q., Xu, C.-Q., Deen, M. J., and Chen, H. (2014). Development of a low-cost hemin-based dissolved oxygen sensor with anti-biofouling coating for water monitoring. *IEEE Sens. J.*, 14(10), 3400-3407.
- Huang, X., and Groves, J. T. (2018). Oxygen Activation and radical transformations in heme proteins and metalloporphyrins. *Chem. Rev.*, 118(5), 2491-2553.
- Jamnongwong, M., Loubiere, K., Dietrich, N., and Hébrard, G. (2010). Experimental study of oxygen diffusion coefficients in clean water containing salt, glucose or surfactant: Consequences on the liquid-side mass transfer coefficients. *J. Chem. Eng.*, 165(3), 758-768.

- Kim, H., Rogler, P. J., Sharma, S. K., Schaefer, A. W., Solomon, E. I., and Karlin, K. D. (2020). Heme-Fe(III) superoxide, peroxide and hydroperoxide thermodynamic relationships: Fe(III)- O_2^* complex H-atom abstraction reactivity. *J. Am. Chem. Soc.*, *142*(6), 3104-3116.
- Li, W., Aoki, K. J., Chen, J., and Nishiumi, T. (2015). Conditions of predominant occurrence of catalytic reduction of O_2 by ferrous hemin over formation of ferrous hemin- O_2 adduct. *J. Electroanal. Chem.*, *743*, 134-138.
- Liang, Z.-X., Song, H.-Y., and Liao, S.-J. (2011). Hemin: A highly effective electrocatalyst mediating the oxygen reduction reaction. *J. Phys. Chem.*, *115*(5), 2604-2610.
- Mihara, N., Yamada, Y., Takaya, H., Kitagawa, Y., Aoyama, S., Igawa, K., Igawa, K., Tomooka, K., and Tanaka, K. (2017). Oxygen reduction to water by a cofacial dimer of iron(III)-porphyrin and iron(III)-phthalocyanine linked through a highly flexible fourfold rotaxane. *Chem.*, *23*(31), 7508-7514.
- Palanisamy, S., Velusamy, V., Chen, S. W., Yang, T. C. K., Balu, S., and Banks, C. E. (2019). Enhanced reversible redox activity of hemin on cellulose microfiber integrated reduced graphene oxide for H_2O_2 biosensor applications. *Carbohydr. Polym.*, *204*, 152-160.
- Pegis, M. L., Martin, D. J., Wise, C. F., Brezny, A. C., Johnson, S. I., Johnson, L. E., Kumar, N., Raugei, S., and Mayer, J. M. (2019). Mechanism of catalytic O_2 reduction by iron Tetraphenylporphyrin. *J. Am. Chem. Soc.*, *141*(20), 8315-8326.
- Schmitz, D., Anlauf, R., and Rehrmann, P. (2013). Effect of air content on the oxygen diffusion coefficient of growing media. *Am. J. Plant Sci.*, *04*(05), 955-963.
- Si, F., Zhang, Y., Yan, L., Zhu, J., Xiao, M., Liu, C., Xing, L., and Zhang, J. (2014). 4 – Electrochemical oxygen reduction reaction. In W. Xing, G. Yin, and J. Zhang (Eds.), *Rotating electrode methods and oxygen reduction electrocatalysts* (pp. 133-170). Amsterdam: Elsevier.
- Šljukić, B., Banks, C. E., and Compton, R. G. (2005). An overview of the electrochemical reduction of oxygen at carbon-based modified electrodes. *J. Iran. Chem. Soc.*, *2*(1), 1-25.
- Sokolov, S. V., Sepunaru, L., and Compton, R. G. (2017). Taking cues from nature: Hemoglobin catalysed oxygen reduction. *Appl. Mater. Today*, *7*, 82-90.

- Song, C., and Zhang, J. (2008). Electrocatalytic oxygen reduction reaction. In J. Zhang (Ed.), *PEM Fuel Cell Electrocatalysts and Catalyst Layers: Fundamentals and Applications* (pp. 89-134). London: Springer London.
- Toader, A., and Volanschi, E. (2007). Electrochemical and spectral study of the hemin-surfactant interaction in solution. *Rev. Roum.*, 52.
- Toader, A. M., Volanschi, E., Lazarescu, M. F., and Lazarescu, V. (2010). Redox behavior of hemin at p-GaAs(1 0 0) electrode. *Electrochim. Acta*, 56(2), 863-866.
- Zhao, Y., Chu, X., and Yang, B. (2017). Electrochemical behavior of hemin binding with human centrin 3. *Bioelectrochemistry*, 117, 15-22.
- Zheng, N., Zeng, Y., Osborne, P. G., Li, Y., Chang, W., and Wang, Z. (2002). Electrocatalytic reduction of dioxygen on hemin based carbon paste electrode. *J. Appl. Electrochem.*, 32(2), 129-133.



CHAPTER VI

CONCLUSION

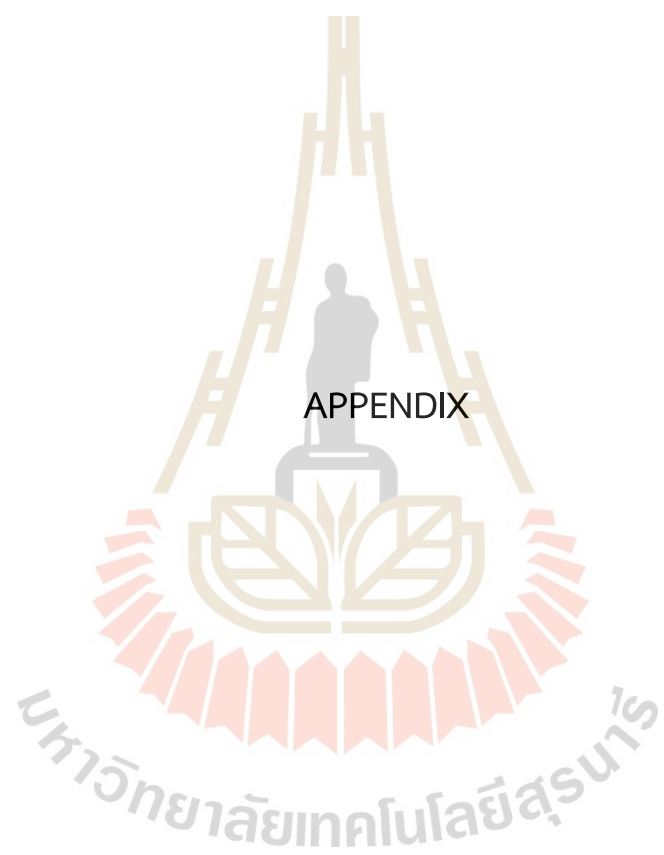
In this thesis, the developed carbon electrode shows strong potential for detecting molecular biomarkers in the human body, such as uric acid (UA), ascorbic acid (AA), dopamine (DA), and hemin under various conditions. In addition, aqueous hemin catalyst was utilized as an oxygen sensor in high salt concentrations.

Copper-based materials (Cu_2O and CuO) and carbon-based materials (CNT and microporous carbon) were investigated for the oxidation of three molecular biomarkers: AA, DA, and UA in synthetic urine samples. The microporous carbon/GCE sensor exhibits excellent electrocatalytic activity, enabling the simultaneous determination of these three compounds in acidic conditions (pH 1.0). This is attributed to the high porous structure, large specific surface area, and high electrical conductivity of microporous carbon, which accelerate the electron transfer rate and enhance the electrooxidation-catalyzed reactions of UA, AA, and DA. High selectivity was achieved because three well-resolved anodic peaks corresponding to AA, DA, and UA were observed when comparing DPV responses of the mixtures with those of the individual species and in synthetic urine samples. The microporous carbon-modified electrode, exhibiting good selectivity and sensitivity, was utilized for the rapid detection of synthetic urine, yielding acceptable recovery results ranging from 96-102%. Additionally, uric acid demonstrates scavenging properties towards reactive oxygen species (ROS) by utilizing hydrogen peroxide (H_2O_2) as a model system.

The hemin iron complex (metalloporphyrin) solution has been explored as an electrocatalyst for detecting dissolved oxygen (DO) in high salt concentrations using CV technique. The introduction of hemin significantly enhances the electrocatalytic activity for the reduction reactions of oxygen. The proposed DO sensor demonstrates high sensitivity, a wide linear response range to O_2 , and a low limit of detection that can effectively detect the low concentration range of O_2 typically found in wastewater. This sensor can tolerate high concentrations of sea salts, exhibits good

reproducibility and long-term stability, and is resistant to interfering species. However, it has been observed that AA and NaNO_2 have a minor influence on DO detection.





APPENDIX

APPENDIX

The quality of a developed analytical method relies on several key performance characteristics, including sensitivity, linear range, limit of detection (LOD), and limit of quantification (LOQ).

A1. Sensitivity

Sensitivity is to be determined within the linear concentration range of the biosensor calibration curve. The slope of the calibration plot is a measure of sensitivity, the sensitivity can compute the LOD and LOQ (Thévenot, Toth, Durst, and Wilson, 2001).

A2. Limit of detection (LOD)

The limit of detection (LOD) is the lowest concentration of an analyte in the sample that can be accurately and precisely detected but not necessarily quantified, under the stated condition of the test (Rahman and Rahman, 2018).

$$\text{LOD} = \frac{3 \times \text{SD}}{m} \quad (\text{A-1})$$

Where SD is standard deviation of the calibrated plot and m is slope of the calibrated line.

A3. Limit of quantification (LOQ)

The limit of quantification (LOQ) is the lowest concentration of the analyte in the sample that can be determined with acceptable precision and accuracy under the stated conditions of test (Rahman and Rahman, 2018).

$$\text{LOQ} = \frac{10 \times \text{SD}}{m} \quad (\text{A-2})$$

Where SD is standard deviation of the calibrated plot and m is slope of the calibrated line.

A4. Linear range

The linear range exhibits a direct proportionality to the concentration of the analyte present in the sample, and it is important for quantitative analysis.

References

Rahman, H. M. R., and Rahman, M. M. (2018). Estimation of limit of detection (LOD), limit of quantification (LOQ) and machine standardization by gas chromatography.

Thévenot, D. R., Toth, K., Durst, R. A., and Wilson, G. S. (2001). Electrochemical biosensors: recommended definitions and classification international union of pure and applied chemistry: physical chemistry division, commission I.7 (Biophysical chemistry); analytical chemistry division, commission V.5 (Electroanalytical chemistry).1. *Biosens Bioelectron.*, 16(1), 121-131.

CURRICULUM VITAE

Name Miss Tidapa Rattanaumpa (E-mail D6200435@g.sut.ac.th)

Education

2012-2016 B.Sc. (Chemistry), Khon Kaen University

2016-2019 M.Sc. (Chemistry), Khon Kaen University

2019-2023 Ph.D. candidate (Chemistry), Suranaree University
of Technology

Scholarship Development and Promotion of Science and Technology Talents
Project (DPST)

Publications

Rattanaumpa, T., et al. (2022). Microporous carbon in the selective electro-oxidation of molecular biomarkers: uric acid, ascorbic acid, and dopamine. *RSC Adv.* 12(29): 18709-18721. (IF (2023) = 4.036)

มหาวิทยาลัยเทคโนโลยีสุรนารี